DEVELOPMENT OF HIGHLY FLUORESCENT NANOSYSTEMS FOR BIOMEDICAL SENSING, IMAGING AND THERAPEUTIC APPLICATIONS

A THESIS PRESENTED BY

RESMI V NAIR

TO
THE SREE CHITRA TIRUNAL INSTITUTE
FOR
MEDICAL SCIENCES AND TECHNOLOGY, TRIVANDRUM
THIRUVANANTHAPURAM

IN PARTIAL FULFILMENT OF THE REQUIREMENTS

FOR THE AWARD OF

DOCTOR OF PHILOSOPHY

2020

CERTIFICATE

I, Resmi. V. Nair, hereby certify that I had personally carried out the work depicted in the thesis entitled, **"DEVELOPMENT OF HIGHLY FLUORESCENT NANOSYSTEMS FOR BIOMEDICAL SENSING, IMAGING AND THERAPEUTIC APPLICATIONS",** except where due acknowledgment has been made in the text. No part of the thesis has been submitted for the award of any other degree or diploma prior to this date.

Resmi V Nair

Reg.No: 2014/PhD/08

Date: 23.09.2020

Dr. R. S. Jayasree
Division of Biophotonics and Imaging
Department of Biomaterial Sciences and Technology
BMT Wing, SCTIMST

This is to certify that **Ms. Resmi. V. Nair**, in the Division of Biophotonics and Imaging Laboratory of this Institute has fulfilled the requirements prescribed for the PhD degree of the Sree Chitra Tirunal Institute for Medical Sciences and Technology, Thiruvananthapuram.

The thesis entitled, **"DEVELOPMENT OF HIGHLY FLUORESCENT NANOSYSTEMS FOR BIOMEDICAL SENSING, IMAGING AND THERAPEUTIC APPLICATIONS"** was carried out under my direct supervision. No part of the thesis was submitted for the award of any degree or diploma prior to this date.

*Clearance was obtained from the Institutional Ethics Committee/ Institutional Animal Ethics Committee for carrying out the study.

Date: 23.09.2020 Dr. R.S. Jayasree

(Research Supervisor)

The thesis entitled

DEVELOPMENT OF HIGHLY FLUORESCENT NANOSYSTEMS FOR BIOMEDICAL SENSING, IMAGING AND THERAPEUTIC APPLICATIONS

Submitted by

RESMI V. NAIR

for the degree of

Doctor of Philosophy

of

SREE CHITRA TIRUNAL INSTITUTE FOR
MEDICAL SCIENCES AND TECHNOLOGY, TRIVANDRUM

Thiruvananthapuram

Is evaluated and approved by

.....	PRADEEP THALAPPIL
Name of the guide	Name of the thesis examiner

ACKNOWLEDGEMENTS

I would like to express my sincere gratitude to my research guide, Dr. R. S. Jayasree for her continuous support, valuable suggestions and patient mentoring during the entire course of my PhD work. I am thankful to her for all the moral support and help she has given me throughout my days in the lab.

I owe my sincere gratitude to The Director, SCTIMST and Head BMT Wing for providing all the facilities during the course of my work. I extend my thanks to Dean, Associate Dean (PhD affairs), Registrar, Deputy Registrar and all members of academic division and Director's office for their support and help.

I am extremely thankful to my doctoral advisory committee members, Dr. K Sreenivasan and Dr. Lissy K Krishnan for their suggestions and critical comments. I am grateful to the Indian Council of Medical Research, Department of Biotechnology and SCTIMST for the financial support.

I thank Prof. A. Ajayaghosh and Dr. K. K Maiti, CSIR-NIIST Trivandrum and their team for helping me in the work and for all valuable suggestions. I also extend my sincere thanks to Dr. Sreejalekshmi and Dr. Rakesh, IIST Trivandrum, for their support and suggestions for my work.

I sincerely acknowledge Dr. Sachin J Shenoy, Dr. Harikrishnan and their team for helping me in animal experiments. I sincerely thank Dr. Kalyana Krishnan, Dr. M.R. Rekha, Dr. Lizymol P P and their team for helping me in dynamic light scattering (DLS) measurements. I am grateful to Dr. Prabha D. Nair, for extending me facility of fluorescence spectrometer for my studies. Dr. Manoj Komath, Ms Susan and Dr.Fransis are gratefully acknowledged for helping in transmission electron microscopy technique. I thank Dr. Anugya Bhatt and her team for helping me in blood related studies.

My sincere thanks also goes to former and present fellows Dr. Arya Saraswathy, Dr. Shaiju, Dr. Lakshmi,, Ms. Nisha, Ms. Lakshmi, Mr. Jayaram, Ms. Parvathy, Ms. Hema, Ms. Renuka, Ms. Marina, Ms. Dhanya, Ms Resmi and Dr. Rekha of

Division of Biophotonics and Imaging. I also thank all staff of BMT Wing, who directly or indirectly helped me for my PhD program. The help from the divisions of accounts, store and library is greatly acknowledged. I also thank the security staff for their kind support.

I owe my deep sense of gratitude and regards to my beloved parents, sister, and brother- in-law for their prayers, affection, patience and support, which smoothly paved the path towards the successful completion of the work. Heartfelt thanks to my husband for his encouragement, support and love.I thank God Almighty for standing with me in all the stages of my life.

Table of Contents

List of Figures

List of Schemes

Abbreviations

NP	Nanoparticles
DI	Deionized water
BSA	Bovine serum albumin
NIR	Near infrared
Qd	Quantum dot or cadmium selenide quantum dot
PAQd	Picric acid functionalised cysteine capped cadmium selenide quantum dot
PA	Picric acid
Creat	Creatinine
Cu	Copper
GQd	Glutathione capped cadmium selenide quantum dot
SMGQd	Sulfamethoxazole functionalised glutathione capped cadmium selenide quantum dot
SM	Sulfamethoxazole
Zn	Zinc
Pb	Lead
AuC	Gold cluster or cystiene capped gold cluster
Dopa	Dopamine
GNR	Gold nanorod
MTX	Mitoxantrone
PGNR	Thioamino functionalised polyethylene glycol capped gold nanorod
FPGNR	Folic acid functionalised PGNR
FA	Folic acid
MTX@FPGNR	Mitoxantrone bonded FPGNR
CTAB	Cetyl Trimethyl Ammonium bromide
PPIX	Protoporphyrin IX
GSH	Reduced glutathione

GSH@GNR	Glutathione capped gold nanorod
P@GNR	Protoporphyrin functionalised with gluthathione capped gold nanorod
F@PGNR	Folic acid functionalised P@GNR
GMSA	Gold nanoparticle with mercaptosuccinic acid
GQC	Glutathione capped gold cluster
GQC-GNR	Hybrid system of gold cluster and gold nanorod
FA-GQC-GNR	Folic acid functionalised GQC-GNR

Synopsis

Nanotechnology has contributed tremendously to the advancement of science, engineering and medicine, especially with the use of newer class of materials viz., nanomaterials. Research related to nanoscience has got a wide acceptance since early nineties. It is the study of particles having size ranges from 1-100 nm. These materials have wide use in various fields including biomedical applications. Disease diagnosis is the prerequisite for the management of any disease. Using the nanotechnological approaches, disease diagnosis and treatment has entered into a new horizon. In this era of increased multiple ailments, timely and accurate disease diagnosis is very important. Here is the importance of developing new approaches for disease diagnosis and treatment; nanotechnology being one of the priority areas among them. Multifunctional nanoparticles have been extensively researched upon for biomedical sensing, imaging and therapy. However, tremendous opportunities are yet to be explored for further utilization of these materials. Generally nanomaterials with electrical, magnetic and optical properties are used depending up on the intended applications. Luminescence is one of the important properties of nanomaterials which are unique with respect to its size and shape. This warrants their potential in biomedical applications. The thesis deals with mainly two classes of optical nanoparticles, semiconducting or quantum dots and metallic nanoparticles, for the design of nanosystems for sensing, imaging and therapy.

The thesis is mainly divided into six chapters viz., introduction, review of literature, materials and methods, results, discussion and conclusion. The first chapter consists of a general introduction on nanoparticles, its properties connected to the specific nanoparticles used in this study, and also introduction on sensing, imaging and therapy. Review of literature involves important research work related to the thesis which was published in recent years with respective references discussed in detail (Chapter 2), followed by materials and methods which explain details of the materials used for the studies and methodologies adopted for completion of the objectives (Chapter 3).

Chapter 4 of the thesis deals with the results followed by discussions, with both chapters subdivided into four major sections. In Chapter 4, the major experimental findings are included, whereas the detailed discussion based on the results are included in Chapter 5.

A brief picture of the chapters on results and discussion is given below. In detail, the first section includes the sensing of biomedically relevant analytes using quantum dots based sensor. In the second section, sensing of dopamine using gold nanocluser along with the use of fluorescence emission of the cluster for cellular imaging is explained. Third one is multimodal imaging and therapy for cancer using gold nanorod systems. And the last one is development of a hybrid gold nanorod-gold cluster system for imaging and therapy.

All the sections dealing with the design of nanosensors make use of the optical property of either semiconductor quantum dots or atomic sized gold nanocluster. Quantum dots are material in the size range of 2 to10 nm with peculiar properties such as fluorescence, non photobleachability and inertness. In the first part of section one a green emitting cysteine quantum dot (Qd) was synthesised and modified with picric acid. This modification imparts dual emission to the system with different excitations (λ_{ex} 390 nm and λ_{ex} 290 nm)- blue and green(λ_{em} 515 nm and λ_{em} 446 nm). The new blue emission at 446 nm is assumed to be originated from the charge transfer due to the complex formation between Qd and picric acid. The complex, PAQd was characterised using different techniques. Absorption peak at 354 nm and a broad shoulder peak at 502 nm indicated the presence of Qd and picric acid in PAQd. The participation of the hydroxyl group in the complex formation was clear from the absence of the corresponding peak in the Fourier-transform infrared spectroscopy (FTIR). Observed CO peak at 1623 cm^{-1}further supported the complex formation. Nuclear magnetic spin resonance (NMR) spectroscopy also confirmed the findings of FTIR. After required characterization, PAQd was used for the simultaneous detection of copper and creatinine. Addition of creatinine showed a concentration dependent increase in the blue emission where as in the case of copper addition, the green emission quenches. The mechanisms behind sensing were studied with the help of transmission electron microscopy (TEM) images and zeta potential

analysis. In the second part of the first section, two different red emitting quantum dots (GQd and SMGQd) were synthesised by using glutathione as capping agent and is further functionalised with sulfamethoxazole. GQd showed characteristic peak at 435 nm and an emission at 680 nm (λ_{ex} 420 nm). The change in fluorescence intensity of GQd in the presence of lead ion was used for the detection of the same, where a concentration dependent decrease in fluorescence intensity was noted. In the case of sulfamethoxazole functionalised quantum dot SMGQd, emission at 586 nm (λ_{ex} 420 nm) showed increase in intensity with zinc concentration. The mechanism behind the sensing of both analytes was explained with the help of size and zeta potential analysis. When zinc sensor showed a sensitivity of nanomolar to millimolar, lead sensor has it in the femtomolar to millimolar level.

Another material used in this thesis is gold cluster. These are materials having size below 2 nm. These clusters have optical properties similar to that of quantum dots. The second section of the work deals with the synthesis of gold clusters with NIR emission. Here, cysteine capped gold nanocluster was used for dopamine sensing and *in vitro* imaging. Since this material has an NIR emission property and had cytocompatible nature the system was successfully used for *in vitro* imaging in L929 and HeLa cells. Upon addition of dopamine to this cysteine gold cluster, the emission at 606 nm (λ_{ex} 400 nm) increases. The sensor has sensitivity in the femtomolar level, for dopamine sensing. Since dopamine is a neurotransmitter its detection in brain cells is important. Hence the sensing is also extended to dopamine incubated brain cells (C6 glial cells).

Next material used in the thesis was gold nanorods, which is anisotropic gold particle having two surface plasmon resonance (SPR) bands due to its longitudinal and transverse vibrations of surface electrons. The longitudinal SPR absorption occurs in NIR region with minor shifts depending on the aspect ratio. Due to the NIR absorption, the particle attains heat generation property when irradiated with laser of suitable wavelengths. Likewise, in this study gold nanorods were used for photothermal therapy in combination with other therapeutic strategy. In the first study GNR, along with a clinically used cancer drug mitoxantrone was used to

enhance the therapeutic efficiency by chemo-photothermal therapy. This material was also designed to have targeted cancer imaging with the use of folic acid. In cancer cells folate receptors are found in large numbers. The functionalisation of drug mitoxantrone (MTX), with gold nanorod imparted an NIR emission for the system (MTX@FPGNR). MTX@FPGNR was proved to be non-cytotoxic in L929 cells for concentrations of the order of 2 mg/ml. *In vitro* imaging was effectively shown in L929, C6 and HeLa cells using MTX@FPGNR. MTX@FPGNR also served as a good SERS agent due to the presence of gold nanorod facilitating additional Raman imaging using the same system. Photothermal efficacy of the MTX@FPGNR was evaluated on irradiation with 808 nm laser. Within 4 minutes, an increase in temperature up to 48^{o}C was achieved. In this case, laser irradiation also triggered drug release with an increase in temperature. The combined treatment efficacy was confirmed and depicted using fluorescence imaging and Raman spectroscopy. The therapeutic efficacy was proven to be much better than that compared to the drug alone. Thus, this is considered as a smart system with dual imaging and dual therapy capabilities where photothermal and chemotherapy are triggered with a laser stimulus. In the second part of the work a gold nanorod-photosensitizer, protoporphyrin IX combination (F@PGNR)was used for photothermal therapy and photodynamic therapy. Here also the cancer targeting was achieved using folic acid.The final system showed an emission at 730 nm which was used for *in vivo* imaging application. The phothothermal efficacy of F@PGNR, with 808 nm irradiation provided a temperature hike of more than 60^{o}C within 4 minutes. 67.5% singlet oxygen generation yield makes the system suitable for photodynamic therapy. Therapeutic efficacy of the system was proved *in vitro* as well as *in vivo* (in tumor induced animals) after irradiation with respective lasers (530 nm and 808 nm).

In the final section, a hybrid gold based system was used for cancer imaging and therapy making use of the photothermal efficacy of gold nanorod and imaging property of gold cluster. Folic acid conjugation facilitated cancer targeting. Characteristic longitudinal and transverse absorption peaks of GNR, supported by electron microscopic data confirmed the formation of gold rods. The emission property of gold cluster was observed at 740 nm. The combined system showed both

the properties of gold nanorod and gold cluster. The imaging efficacy of the system was proved *in vitro* using fluorescence microscopy and the treatment efficacy was monitored using live/dead and MTT assay. It is found that in both the applications, the hybrid system was superior to its individual counter parts. The imaging of this material using the construct was also demonstrated *in vivo*.

The final chapter of the thesis summarises the work of six different nanosystems synthesized and optimised for applications like sensing, imaging and therapy, and studied in this thesis. The thesis starts with the uses of a basic nano system viz., quantum dots for the sensing application and ends with an advanced hybrid nanosystem, all useful for biomedical applications. The future prospects of the study are to make the sensors available for clinical use. In case of therapy and imaging, combining these multiple modality in a single platform for better efficacy and performance will be much appreciated.

CHAPTER 1

INTRODUCTION

Nanoscience and nanotechnology have played a significant role in the present era of scientific research through the development of novel nanoscale material for various applications ranging from energy, environment, catalysis, health care etc. Interdisciplinary areas of science have got wide acceptance after the well-known talk *"There's plenty of Room at the Bottom"* by Physics Nobel Laureate Prof. Richard P. Feynman in the annual meeting of American Physical Society at California Institute of Technology, on December 29th 1959 (Feyman 1960). The talk mainly focuses on the miniaturization of materials, which may resolve various scientific problems that existed during that period of time. Nanoscience deals with the manipulation of materials in the nanoscale size by designing them with desired property. A nanometer is one-billionth (10^{-9}) of a meter(Ghosh & Pal 2007). Nanotechnology is defined as the manipulation of individual atoms or molecules in the nanometer dimension (with at least one-dimension sized between 1 to 100 nanometers). Nanomaterials may be zero-dimensional (spherical nanoparticle), one dimensional (nanorod or nanotubes), two dimensional (film or stack of thin-film) or three dimensional (flower, coil, etc.) in nature based on its dimension (Alagarasi 2011).

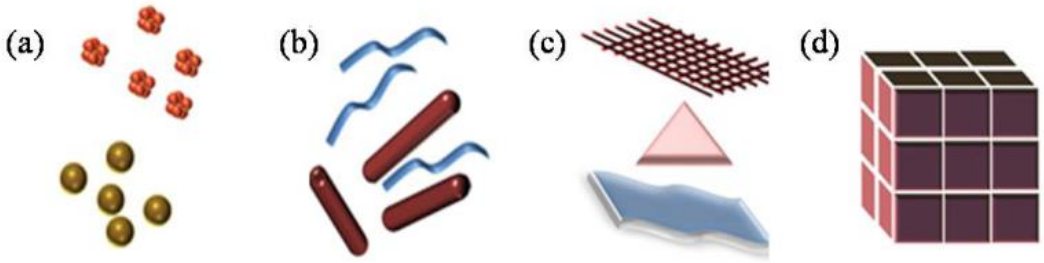

Figure 1: Classification of nanomaterials (a) 0D spheres and clusters, (b) 1D nanofibers,wires, and rods, (c) 2D films, plates, and networks, (d) 3D nanomaterials (Alagarasi 2011).

Nanoparticles are much larger than individual atoms and molecules but are smaller than bulk materials, and their behavior is in between a macroscopic solid and atomic or molecular systems. The electron energy levels in nanostructures are discrete, consisting of the finite density of states. This is due to the confinement of electron wave function to the physical dimensions of these nanostructures. The energy states of the nanomaterials are determined by the boundary conditions, and therefore surface effects becomes very important. High surface to volume ratio, quantum size effect, and electrodynamic interactions are the major factors responsible for the drastic property change of these materials in comparison with their bulk counterparts.

1.1. Special properties of nanoparticles

The scientific community has made significant contributions to nanotechnology based novel materials and devices by utilizing the diverse concepts from engineering, physics, chemistry, materials science, biology, agriculture, and medical sciences. As a result, the last decade has witnessed break throughs in nanotechnology mediated biomedical fields such as sensing, imaging and therapy. Unique optical, chemical, and magnetic properties of the nanomaterials compared to their bulk material impart these applications.

1.1.1. Electronic properties

Electronic properties of nanomaterials changes with the system's length scale, and it reduces when there is an increasing influence of the quantum mechanical effects and the lack of scattering centers. When the size of the nanomaterials is in the range of de Broglie wavelength of the electrons, the energy state becomes discrete, although a fully discrete energy spectrum is observed only when these materials were confined in all the three dimensions. In certain cases, the energy bands of conducting materials cease to overlap and become insulators below a critical length scale. Quantum mechanical tunneling occurs between two closely adjacent nanostructures due to their intrinsic wave-like nature. The tunneling current increases if a voltage is applied between two nanostructures, which aligns the discrete energy levels in the density of states (DOS). The presence of other charge carriers influences the conduction and charge state of certain materials like quantum dots. These Coulomb blockade effects result in conduction processes involving single electrons, and as a result, they require only a small amount of energy to operate a switch, transistor, or memory element. All these phenomena can be utilized to produce radically different types of components for electronic, optoelectronic, and information processing applications, such as resonant tunneling transistors and single-electron transistors (*Ray et al.,* 2006).

1.1.2. Magnetic properties

Magnetic nanoparticles are used for avariety of applications like imaging, bioprocessing, refrigeration, as well as in high storage density magnetic memory media.

The large surface area to volume ratio results in a substantial proportion of atoms to have different magnetic coupling with neighboring atoms leading to differing magnetic properties(Kumar & Mohammad 2011). Nano sized gold and platinum are magnetic, whereas, in bulk, they are non-magnetic. Gold nanoparticles become ferromagnetic when they are capped with the appropriate molecules such as

thiol. Giant magnetoresistance (GMR) is a phenomenon observed in nanoscale multilayers consisting of a strong ferromagnet (Fe,Co,Ni) and a weaker magnetic or non-magnetic buffer (Cr,Cu). It is usually employed in data storage and sensing. Magnetic nanoparticles are used in biomedical applications such as for contrast enhancement in magnetic resonance imaging (MRI), and targeted drug delivery (Frandsen & Hansen 2010). MRI is an imaging technique used to form pictures of the anatomy and the physiological process of the body with the aid of magnetic contrast agents. In nanomaterial research, superparamagnetic iron oxide nanoparticles are widely used for MR imaging. In combination with other materials, magnetic nanomaterials are used for MR imaging, therapy and drug delivery (L. Li *et al.,* 2013; Sulek *et al.,* 2011).

1.1.3. Optical properties

In the case of small nano clusters, the effect of reduced dimensionality on the electronic structure has the most profound effect on the energies of valence band or highest occupied molecular orbital (HOMO) and the conduction band or the lowest unoccupied molecular orbital (LUMO). The optical emission and absorption occur when the transition of the electrons takes place between these two states. Semiconductors and many other metals show size dependent optical properties. Colloidal suspensions of gold nanoparticles have a deep red color, which becomes progressively blue/purple as the particle size increases (Kumbhakar, Ray & Stepanov 2014). The optical properties of nanomaterials are mainly due to surface plasmon resonance (SPR) in the case of metallic nanomaterial and quantum confinement effect for quantum dots.

Other optical properties which may be influenced by reduced dimensionality include photocatalysis, photoconductivity, photoemission, electroluminescence etc.

1.1.3.1. Optical properties of semiconducting nanoparticles

Semiconducting nanoparticles are usually group III-V, II-VI and silicon-based systems with particle size between 2-10 nm (Smith & Nie 2010). Unlike the bulk semiconducting materials, the nanoparticle with size less than 10 nm shows discrete energy levels rather than continuous valence band and conduction band. The

energy gaps in larger semiconducting dots are less compared to smaller ones. This change in the energy gap is responsible for the change in fluorescence property with size. When a photon of sufficient energy (greater than or equal to the bandgap) strikes a quantum dot, it can excite an electron from the valence band to the conduction band, leaving a positive hole in its place. This generates an electron-hole pair (also known as an exciton) which is a common phenomenon occurring in semiconducting materials. However, in a quantum dot, the average exciton size (the exciton Bohr radius) is smaller than the size of the quantum dot, producing confinement of energy as the exciton is squeezed into the material.

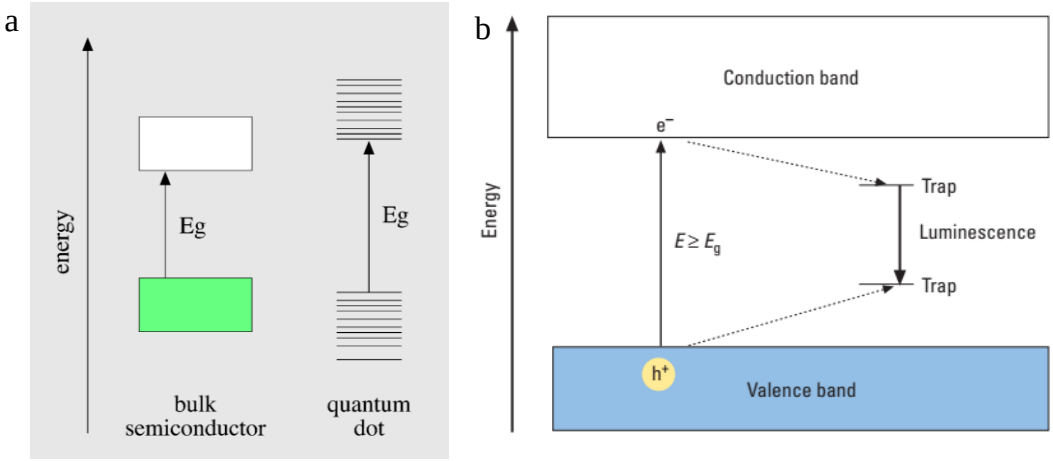

Figure 2: a) Continuous energy level of bulk semiconductor and discrete energy levels of quantum dots (Murphy & Coffer 2002), b) Electron- hole pair formation when photon absorbed having energy greater than or equal to the energy of Bohr exciton radius (Murphy 2002).

1.1.3.2. Optical properties of metallic nanoparticles

Optical properties of metallic nanoparticles are unique and this will depend on their size, shape, surface characteristics and morphology. The reason for this exclusive property is a phenomenon known as localized surface plasmon resonance (LSPR) and it is the collective oscillation of conduction band electrons that are in resonance with the oscillating electric field of the incident light. The oscillation frequency is determined by four factors: the density of electrons, the effective electron mass, and the shape and size of the charge distribution (Jain *et al.*, 2007; Pinchuk, Kreibig & Hilger 2004).

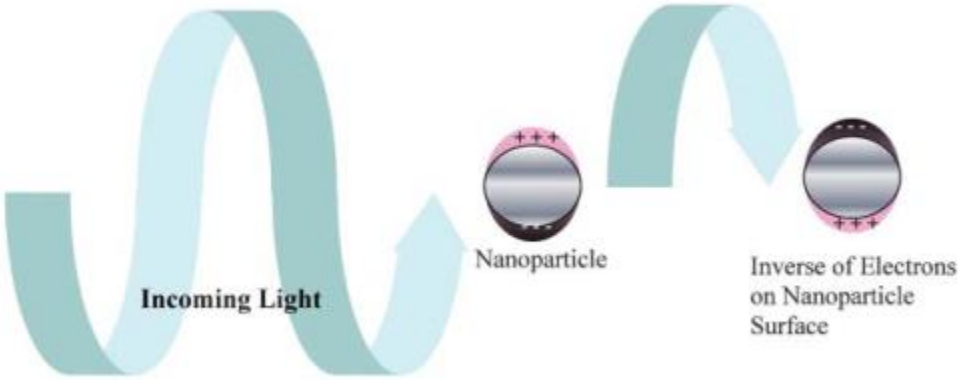

Figure 3: Origin of surface plasmon resonance due to coherent interaction of the electrons in the conduction band with light (Eustis, El-sayed & Kasha 2006).

1.2. Importance of optical properties

The nanoparticles (metallic and semiconducting) (Astruc 2009; Ray *et al.*, 2006) have attracted strong interest as a novel platform for nanobiotechnology, biomedical technology and biomedicine (Panyala & Havel 2009; Shim, Lim & Nam 2008) because of the efficient bioconjugation potential and remarkable optical properties (Kreibig & Vollmer 1996). Applications of these nanomaterials include genomics, biosensors (Kelly *et al.*, 2003), immunoassays (Liu *et al.*, 2008), clinical chemistry (Baptista *et al.*, 2008), detection and control of microorganisms (Gupta *et al.*, 2007; Luo & Stutzenberger 2008), cancer cell detection and treatment (Huang, Jain & El-sayed 2008; Lal, Clare & Halas 2008), targeted delivery of drugs or other therapeutic substances (Han, Ghosh & Rotello 2007), optical imaging and monitoring of biological cells and tissues (Aaron *et al.*, 2008), optical coherence tomography (Gobin *et al.*, 2007), two photon luminescence (Park *et al.*, 2008), or photoacoustic (Han, Ghosh & Rotello 2007) techniques.

Optical imaging uses visible light and the special properties of photons to acquire details of organs and tissues as well as smaller structures, including cells and even molecules. These images are used by scientists for research as well as disease diagnosis and treatment.

Main advantages of optical imaging compared to conventional imaging techniques are

- Optical imaging significantly reduces the exposure of harmful radiation by using non-ionizing radiation such as visible, ultraviolet, and infrared light. Optical imaging is safer for patients and significantly faster.This can also be used to monitor the progression of the disease.
- Soft tissues can also be visualized using optical imaging techniques due to the difference in absorption / scattering of light by the tissues.
- Because it can obtain images of structures across a wide range of sizes and types, it can be combined with other imaging techniques, such as MRI or x-rays, to provide enhanced information.
- Optical imaging techniques make use of different wavelengths of light for visualizing and analyzing different properties of an organ or tissue simultaneously, whereas other imaging techniques are limited to one or two measurements at a time.

Light penetration of tissue is basic for optical imaging. Depending on the depth and thickness of the tissue, the information obtained will vary. It is mainly because the tissue is not transparent to the visible light of the electromagnetic spectrum. Most of the optical applications favour the use of near-infrared (NIR) light because the tissue is less absorbing in this region.

Fluorescence molecules absorb photons, and excited and return to its ground level,emitting a longer wavelength light in a certain period of time.This emitted light is acquired with high precision by filtering the emitted photons from the excitation wavelength.The absorption of photons by tissue takes place in less than 1 cm depth. Time resolved fluorescence imaging technique can be employed for imaging samples with thickness up to 3 cm without background signals. Advanced techniques like fluorescence lifetime imaging are useful to assess the local environment of fluorophores such as refractive index, local pH, ion concentration, and oxygen concentration. The fluorescence lifetime exploits differences in fluorescence lifetimes of the order of nanoseconds to monitor target fluorescence.

Molecules with high fluorescence quantum yield, high molar absorption coefficient, an adapted fluorescence lifetime, and a large Stokes shift are efficient fluorophores. The Stokes shift is thedifference in energy between absorption band

maxima and emission band maxima. Signal collection efficacy of a fluorophore is determined by this Stokes shift, which in turn control the possibility of spectral cross-talk in more than one fluorophore. Forster resonance energy transfer (FRET) and spectral multiplexing are examples for spectral cross talk. FRET has been employed in different systems for measuring enzymatic activities or physico-chemical variations. After labeled with a FRET-pair of fluorophores, this technique could be useful in monitoringthe degradation of a macromolecule, including nanoparticles. Non toxicity, ability to attach to the molecule of interest, solubility, and stability in biological fluids are additional advantages for using these fluorophores in the biological environment.

Similar to optical imaging, optical sensing is another important application of nanoparticles with optical properties. A nanosensor consists of a biosensitive layer that either contains a biological recognition molecule or has the property to attach a biological recognition molecule to it. Among various nanobiosensing techniques, optical sensing is one of the most accepted methods. This is because, even very small changes in the signal is detectable, due to the advancement in the technology of the optical detectors. Optical sensingis passive to electrochemical interferences, in the wide dynamic range, and the multiplexed detection is also possible with this technique. In this method, the change in the property of light is measured in any one or more forms of intensity, phase, polarization, wavelength, and spectral distribution by measuring absorbance, fluorescence, refractivity etc.

In this thesis, biomedical applications of nanoparticles are studied by considering their optical properties. Thus, the prominent ones among the optical nanoparticles viz. semiconducting and metallic nanoparticles are chosen for the entire study for sensing, imaging, and therapeutic applications.

1.3. Sensing

In disease diagnosis and the treatment that followed, the detection of specific molecules from the body is very important. The devices which help to monitor the desired analyte or molecule are called sensors. Sensors respond to the presence of analyte molecule, which can be measured electrochemically, optically, acoustically, mechanically, calorimetrically or electronically, and then correlate with the analyte concentration. The method of transduction depends on the type of physico-chemical change resulting from the sensing mechanism. In 1962, the first report on glucose oxidase (GOD) biosensor by Clark and Lyons (Lyons C Leland 1962). Since then, biosensors have been intensively studied and utilized in various applications. Nanomaterials due to its high surface to volume ratio are widely used in the field of sensing.

1.4. Cancer

Cancer is a condition when uncontrollable cell division occurs or when the mechanism of usual cell death of the body does not occur to a particular type of cell at a particular region. Cancers are mainly of two types, benign and malignant. Benign tumors are not considered as cancer as they are a bunch of cells grown locally without spreading to other tissue and organs. But in the case of malignant cancers, cancer will spread to neighboring tissues and spread through blood vessels.

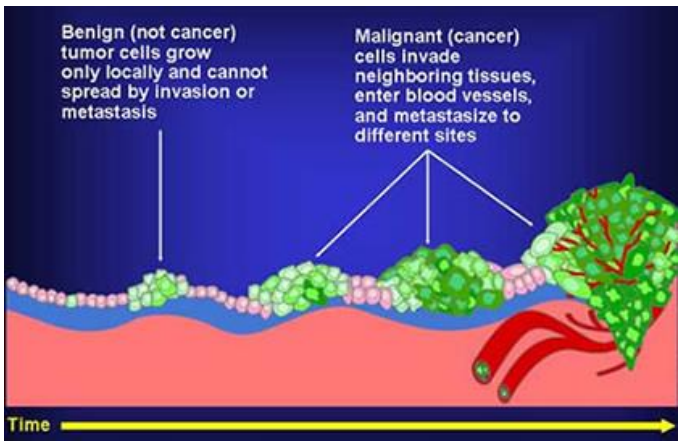

Figure 4: Pictorial representation of different stages of cancer. Reproduced from the official site of Edward Comprehensive Cancer Centre.

According to the World Health Organization (WHO) report of 2018, cancer burden has risen to 18.1 million new cases and 9.6 million deaths. It indicates that despite the vigorous research taken place in these fields; still, the mortality incidence ratesare high.Many attempts are going on to control and cure cancer employing techniques like chemotherapy, photodynamic therapy (PDT) and photothermal therapy(PTT). The unique properties of nanomaterials recommendto use them as drug carriers, PDT agents, imaging agents, etc. and has attracted wide use in cancer diagnosis and therapy (figure 5)

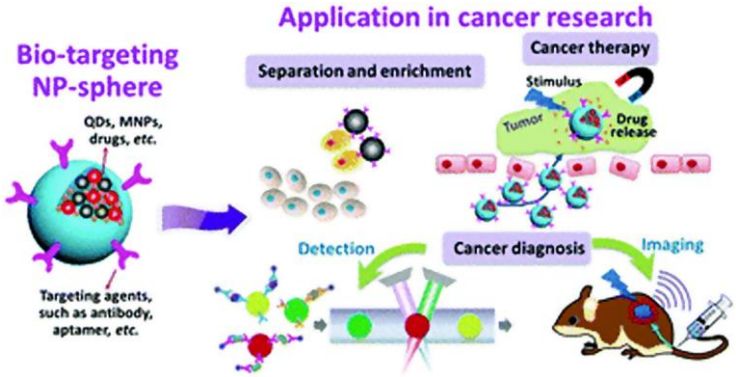

Figure 5: Representation of the use of nanoparticles in cancer research (Parvanian, Mojtaba & Aghashiri 2017).

1.4.1.Chemotherapy

In chemotherapy, a drug or combination of drugs is given to the body to prevent tumor growth. The action of drugs is either to enter into the cell division pathway to induce apoptosis (programmed cell death) or to block the blood supply around the tumor region so that it will starve. As a result, the destruction of the tumor will occur. The main drawback of chemotherapy is that the chemotherapeutic agents are nonspecific; it may cause damage to normal cells. Another limitation of chemotherapy is the mode of action of chemotherapeutic drugs may cause adverse effects to cancer treatment by making the cells survive in starvation conditions and that may cause changes of metastatic condition to cancer or by making it multidrug resistance. Various chemotherapeutic drugs (doxorubicin, epirubicin, paclitaxel, docetaxel, 5-fluorouracil, cyclophosphamide, carboplatin, mitoxantrone, etc.) are used to treat cancer.

1.4.1.1. Mitoxantrone

Mitoxantrone is one among the long list of cancer drugs used clinically. In an effort to find an analogue to the existing cancer drug, doxorubicin to avoid cardiac toxicity, a new drug 1,4-dihydroxy-5,8-bis[2-(2-hydroxyethylamino)ethylamino]anthracene-9,10-dione commonly known as mitoxantrone was discovered in 1980 (Fox 2004). Mitoxantrone, a drug from the class of anthracenedione is the only drug approved for clinical use. It is generally used for breast cancer, acute leukemia, lymphoma and prostate cancer etc.

The ability to bind to DNA and to inhibit both DNA replication and DNA-dependent RNA synthesis is involved in the antitumor activity of mitoxantrone. It is also a potent inhibitor of topoisomerase II, which is an important enzyme for the repair of damaged DNA. It acts via causing single and double-stranded breaks. Structurally mitoxantrone contain symmetrical a tricyclic planar chromophore substituted with two nitrogen-containing side chains (Figure 6) (Enache, Toader & Iancu 2016).

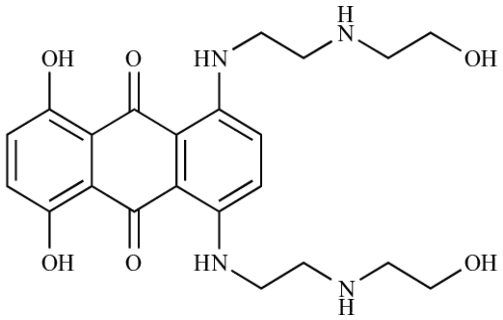

Figure 6: Structure of mitoxantrone.

This drug has emission in the near-infrared (NIR) region. So, in combination with other therapeutic nanomaterials, this drug can be used as both imaging and therapeutic agent.

1.4.2. Photothermal therapy (PTT)

PTT is a minimally invasive local treatment in which materials with optical absorption on interacting with electromagnetic radiation such as radiofrequency, microwaves, NIR, or visible light gets stimulated and produces heat energy. The heating in the biological environment causes hyperthermia, resulting in adverse cellular events such as protein aggregation and denaturation, evaporation of cytosol, and cell lysis. For living cells, it is determined that PTT induces programmed cell death by activating the intrinsic pathway rather than necrotic cell death (Lapotko 2009; Roti 2008). Necrotic cell death stimulates inflammatory responses, which may usually compromise the antitumor activity (Perez-Hernandez *et al.*, 2015)(Rock & Kono 2008). Therefore, PTT is considered to be a reliable and powerful treatment modality for cancer.

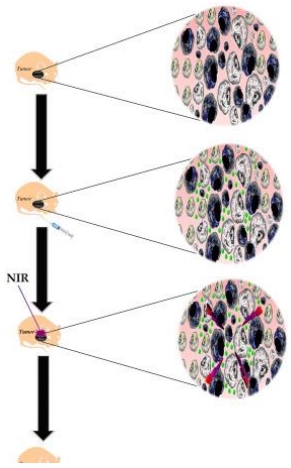

Figure7: Schematic representation of photothermal therapy in tumor bearing mice (Eskiizmir & Yapıcı 2018).

Nanomaterials having efficacy to generate heat upon absorption of suitable wavelength of light (NIR region) are widely used as photothermal agents. PTT is generally used in conjunction with imaging modalities for diagnosis and with other treatment modalities to enhance therapeutic efficiency. Carbon nanotubes, Gold nanorods, graphene, etc.are proven to have very good photothermal properties due to their efficacy to convert absorbed photons into heat via electron electron interaction or electron phonon interaction.

1.4.3. Photodynamic therapy (PDT)

PDT is a FDA approved therapy for cancer treatment, which requires a photosensitizer, suitable light source and oxygen. Upon irradiation of photosensitizer (PS) molecule in the presence of oxygen,PS undergoes excitation to higher state followed by the relaxation. PS relaxation occurs through two pathways, emission of fluorescence and intersystem crossing that leads to the production of singlet oxygen ($^1O_2$) and other reactive oxygen species, which may destroy cancer cells by indiscriminate oxidation. In both ways, depending on quantum yield,these photosensitizer molecules can be used both as cancer imaging and treatment modality. The class of molecules of porphyrins is commonly used as photosensitizer. Protoporphyrin IX is one among them and has been approved by FDA.

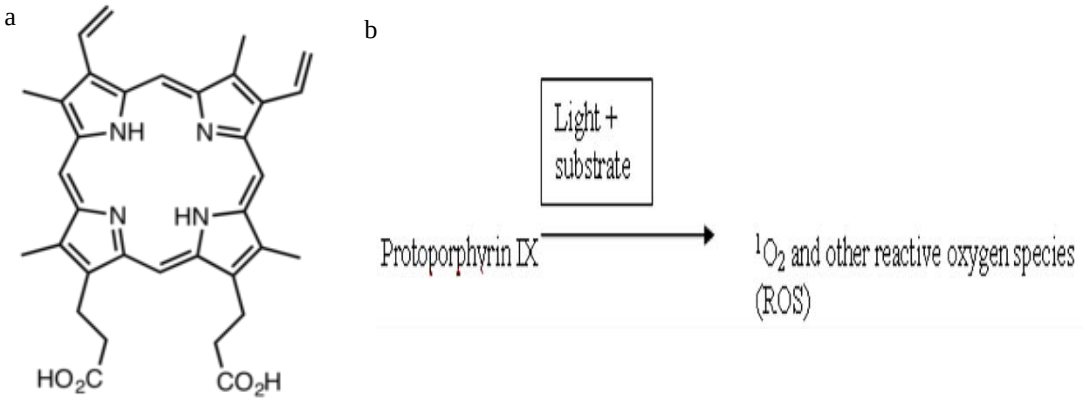

Figure 8: a) Structure of protoporphyrin IX b) Schematic representation of singlet oxygen production when a suitable wavelength of light falls on it.

The scope of using nanomaterials along with PS for cancer treatment, is well explored as it has several advantages over the use of PSalone. These include targeted delivery of PS, so that dark toxicity is avoided, use of multiple functions for imaging in addition to PDT, usage of the reduced amount of PS due to targeting ability etc. The working mechanism of such nanocarriers is demonstrated in figure 9.

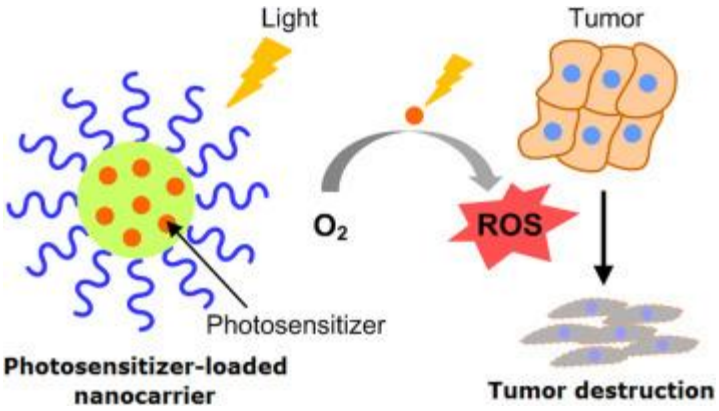

Figure 9: Use of photosensitizer along with nanocarrier to treat cancer (Hong, Choi & Suk 2016).

1.5. Quantum dots for sensing applications

A sensor is a device that will respond or react to physical, chemical, or biological changes that happens in the presence of analytes. The response will be recorded in different forms of signals. Various fields such as police department, defense, health care etc. use the technique of sensing of different analytes for applications related to criminal investigations, security and disease diagnosis. In the healthcare industry, a particular disease or disease condition or health status can be detected through the sensing of different analytes present in the biological fluids. Different materials ranging in size from bulk to nano are used for sensing applications. Nanomaterials based sensors have got wide acceptance due to the fact that these materials have the unique property of high surface to volume ratio, which increases the sites for surface specificity and hence sensitivity, which is the most important parameter required for any sensor.

Quantum dots are one among the nanoparticles having a narrow emission profile and having size dependent fluorescence property, and they are resistant to chemical and biological degradation. They are non-photo bleachable in comparison with conventional dye molecules. So quantum dots are one of the important candidates for biosensing applications (Matea & Mocan 2017; Pereiro & Sanz-medel 2006).

1.6. Fluorescent gold based systems for sensing and imaging

Gold nanoparticles are candidates in the nano regime with well demonstrated optical properties. However, spherical gold nanoparticles do not possess fluorescence property. But due to LSPR and comparatively lesser cytotoxicity, they get wide acceptance in the sensing of biomolecules in health care industry. Lack of fluorescence property limits the use of bare gold nanoparticles in fluorescence imaging. Therefore,to overcome this limitation, a new class of material known as gold clusters comprising few atoms of gold was developed. Gold nanoclusters are particles havingsize less than 2 nm; they are smaller than nanoparticle but larger than an atom. They are having peculiarities such as photoluminescence, non-photobleachability, photon anti-bunching, longer fluorescence lifetime when compared to the conventional organic fluorophores and versatility in applications. Electronic states of gold nanoclusters are quantum confined, i.e., it possesses a discrete valence bands and conduction bands susceptible to electron transfer between them, unlike in the case of bulk gold or bigger nanoparticles. This phenomenon of quantum confinement effect makes gold nanoclusters fluorescing.The fluorescence property of gold nanocluster changes from visible to NIR region depending on the number of metal atoms and the ligands and the local environment. It is also reported that by changing the ligand, the fluorescence property of the nanocluster can be tuned (Chen *et al.*, 2015, 2014; Li, Schluesener & Xu 2010; Luo *et al.*, 2017; Peng *et al.*, 2018). Various ligands such as glutathione, large polymers, and peptide molecules are used for the synthesis of gold nanoclusters.

1.7. Gold nanorod for cancer imaging and therapy

Gold (Au) based nanomaterials are considered to be safer in the biomedical application when compared with semiconducting materials. The shape of the gold nanoparticles plays an important rolein deciding its property. In comparison with spherical nanopartilces, nonspherical ones exhibit anisotropic optical and electronic responses that are determined by their topological aspects. Among various gold nanomaterials with nonspherical shapes, much attention has been paid to gold nanorods. Because of their essential applications in optical devices, biochemical

sensors, and nanomedicine, the growth and characterization of gold nanorods have encountered an upsurge in research activities since their first discovery in1991(Gole& Murphy 2004; Huang, Neretina & El-Sayed 2009). The most important property of gold nanorod is its LSPR. Collective confinement of oscillations of the free electrons in the nanoscale is responsible for LSPR(Nikoobakht & El-sayed 2003; Zijlstra & MoNOS 2011). LSPR of gold nanocrystals can be tuned by changing the reaction conditions of synthesis and thereby changing the aspect ratio. The gold nanorod has two modes of absorption, longitudinal mode and transverse mode. The longitudinal plasmon oscillations is responsible for the NIR absorption, which subsequently lead to heat generation when NIR laser is irradiated. This heat generation efficacy of gold nanorod makes it suitable for cancer treatment using the technique of PTT (destroying cancer cells due to heat generation) (Hartland 2011; Jain *et al.,* 2008; Link & El-sayed 2010; Mackey *et al.,* 2014; Stockman 2011). Gold nanorod can also be used as a treatment modality in combination with chemotherapy and photodynamic therapy (Bucharskaya*et al.,* 2016; Choi, Park & Yeon 2018; Hauck *et al.,* 2008; Jang *et al.,* 2011a; Kuo *et al.,* 2010; Li *et al.,* 2014; Popp *et al.,* 2014; Yang *et al.,* 2018; Zhang *et al.,* 2016). Chemotherapy is the treatment of cancer using conventional drugs. But it has limitations such as nonspecificity, due to which damage to the normal cells is very common. Also, these drugs cause severe side effects and the demand for high dose due to nonspecificity. These side effects could be controlled to a great extent using targeted delivery of drugs using nanocarriers and by enhancing their therapeutic efficiency using additional treatment modalities like PDT and PTT. PDT is an approved and well established treatment modality where free radicals are created for the destruction of cancer cells. Here, PS molecules, when irradiated with a suitable laser, generate singlet oxygen that leads to stress in cancer cells leading to cell death. These two techniques, together with PTT, are used for enhancing the efficiency of cancer treatment.

1.8. Hybrid system for imaging and therapy

Hybrid nanomaterials are two or more nanoparticles suitably combined to get properties of both the parental nanoparticles. When nanoparticles with different properties are combined without compromising its individual properties, it is important to control the reaction so that it can act as a single system without losing its original identity (Taylor-pashow *et al.,* 2010; Tian *et al.,* 2018). For example, when a particle having a magnetic property is combined with material with optical property, the final system will possess both magnetic and optical properties. Usually, two different classes of materials are used for making hybrid systems. Reports on hybrid systems of the similar or same material are rare. Hybrid material involving two gold based systems like gold nanoclusters and gold nanorod will have imaging and therapeutic property but has not been reported. Hybrid materials with different combinations of nanomaterials are useful for cancer therapy by increasing the desired properties with the appropriate combinations (figure10)

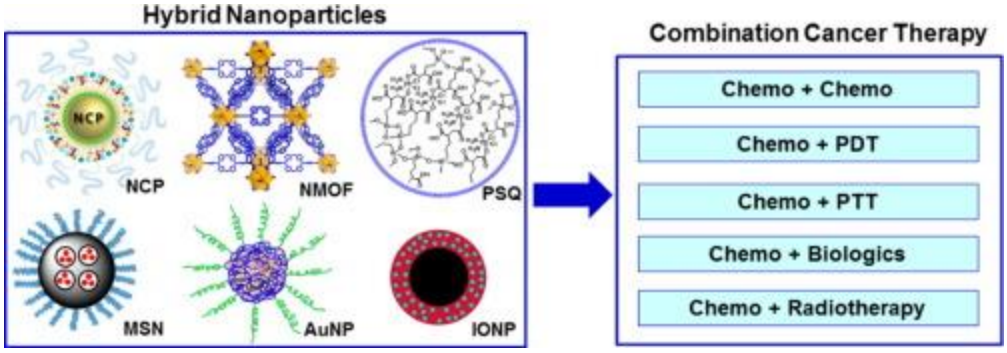

Figure 10: Hybrid nanomaterials with different types of nanoparticles (NCP-nanoscale coordination polymers, NMOF-nanoscale metal-organic frame works, PSQ- polysilsesquioxane, mesoporous silica, AuNP-gold nanoparticle, IONP-iron oxide nanoparticles) used for combinational cancer therapy (He, Lu & Lin 2015).

1.9. Hypothesis

Considering the broad spectrum of application possibilities of nonomaterials, it is hypothesized that nanosystems could be designed to suit the needs of imaging,diagnosis and therapies. Among the various systems, systems with optical property have much importance in sensing, imaging, and therapy. So, the broad idea for the thesis is to develop highly fluorescent nanosystems for biomedical sensing,

imaging, and therapy. By considering the optical efficiency and the toxicity of semiconducting nanoparticles with respect to metallic nanomaterial, it is hypothesized that semiconducting nanoparticle or quantum dots will be more suitable for sensing applications and metal based nanomaterial for sensing, imaging, and therapy. Accordingly, the objectives of the thesis are formulated as follows.

1.10. Objectives

The major objectives of the study are

- To develop fluorescent nanoparticle for biomedical sensing.
- To develop metallic nanoparticles for sensing and imaging.
- To develop multifunctional fluorescent nanopartcles for imaging and therapy
- To develop hybrid fluorescent nanoparticles for imaging and therapy

Chapter 2

Literature Review

Nanomaterials, with size ranging from 1-100 nm, have gained considerable attention due to their wide range of applications, for the last few decades. But the investigation of the unique properties of these nanomaterials has reached only to the tip of an iceberg, so far. Here are some of the research findings, which paved the path for this thesis work. Different nanomaterials have emerged within thirty years, with advancements in the field of nanotechnology. Quantum dots are one among the nanomaterials (semiconductor nanoparticle) with peculiar size dependant fluorescent properties. Gold based nanomaterials are another important class of nanomaterials that possess unique optical properties. Particularly, gold nanoclusters, composed of a few atoms, exhibit quantum confinement with exceptional fluorescent properties. These are applied for various biomedical applications, especially sensing. Gold nanorods like anisotropic gold nanomaterial with photothermal properties, are widely used for therapeutic applications.

2.1. Quantum dots for sensing

Semiconducting nanoparticles or quantum dots are a special class of inorganic nanocrystals composed of atoms of group II-VI, III-V, IV-VI elements (Murphy, 2002). The optical properties of semiconducting nanomaterials are generated when the electron-hole pair becomes confined (Hegazy & El-hameed 2014) in the quantum dimension. This confinement leads to an increase in the band gap with a decrease in particle size. High surface to volume ratio makes electron-hole pairs to be spatially confined (Moradian *et al.*, 2011). These features led to the synthesis of various types of size and shape-controlled quantum dots. Cadmium selenide (CdSe) is one of the most studied quantum dots. Different synthesis strategies like wet chemical method, solvothermal /hydrothermal processes, etc. are available for quantum dots; among them, wet chemical method is the popular one for biomedical applications.

2.1.1. Cadmium selenide quantum dots for the simultaneous detection of copper and creatinine.

The elevated creatinine level in serum is a sign of impaired renal function, chronic nephritis or urinary tract obstruction, and skeletal muscle diseases. Imbalance in creatinine (Creat) level leads to diseases like chronic kidney disease or serious kidney damage, heart failure, dehydration, liver disease (cirrhosis), hyperthyroidism etc (Jose *et al.,* 2006; JP *et al.,* 1993; Kreisman & Hennessey 1999). Similarly, copper (Cu) is an essential trace element in specific enzymes for proper growth, development, and functioning of organs with a normal range of 0.0016 - 0.0024 µM in blood serum. Cu plays an important role in maintaining and repairing connective tissues. It is an important metal for the health of the heart and arteries (Dinicolantonio, Mangan & Keefe 2018). Cu deficiency plays a role in coronary heart disease (Klevay 1984). Other conditions associated with Cu scarcity include nutritional deficiency, inability to absorb copper, Wilson's disease, and rheumatoid arthritis (Uauy, Olivares & Gonzalez 1998). Time-bound and early-stage detection of these two analytes will give a better understanding in maintaining the homeostasis of the body. Though several reports are available for individual detection of Cu and creat (Du *et al.,* 2015; Fu *et al.,* 2018; He, Zhang & Yu 2015; Mehta, Kumar & Kailasa 2013a; Pundir, Yadav & Kumar 2013; Rahman, Ahmed & Asiri 2016; Sittiwong & Unob 2015; Song *et al.,* 2010a, 2010b; Xu *et al.,* 2012), few studies are available for their simultaneous detection.

There is an increasing demand for the detection of clinically significant metabolites from body fluids with high selectivity and sensitivity, which is an indicator of health status. Currently, available techniques lack the ability of determining more than one analyte using a single technique from a single draw of blood. Accordingly, the concept of multianalyte sensing has recently been identified as important, where the information about multiple analytes could be derived from a single draw of blood in a very short time. This concept finds importance in cases of diseases having more than one marker for confirmation or more than one disease condition at the same time. In this context, multi analyte nanosensors (MANS) are

the new promising candidates. However, a few attempts have been made to explore this concept (Komatsu *et al.,* 2005; Ruedas-rama & Hall 2010; Sugunan *et al.,* 2005; Wu *et al.,* 2010, 2012). A report on multianalyte sensor deals with quantum dot-DNAzyme (modified DNA sequence) based nanomaterialfor multiplexed detection of heavy metals Cu and lead (Pb) ions using fluorescence property (Wu *et al.,* 2010). In another study, silica nanoparticles were used for the detection of Hg^{2+}, H_2SO^{4-} and S^{2-} in live cells by measuring the change in fluorescence property, which has also been used as an intracellular imaging modality (Wu *et al.,* 2012). Komatsu *et al.,* developed a single fluorescent probe based on coumarin for the detection of multi analytes Ca^{2+} and Mg^{2+} ions, and the same material were used for fluorescence imaging application (Komatsu *et al.,* 2005). Maria J. Ruedas-Rama and co-workers reported the change in the fluorescence property of an enzyme-linked nanosphere sensor for the detection of urea and creatinine (Ruedas-rama & Hall 2010). In another study, Sugunan*et al.,* worked on chitosan capped gold nanoparticles for the detection of zinc and copper ion by using the chelating property of chitosan along with the optical properties of gold nanoparticle. The change in the absorption spectra, on treating with metal ions, gives a good indication of heavy metal ions concentration in it (Sugunan *et al.,* 2005). Among the various nanomaterials, quantum dots have attracted wide acceptance in designing of optical nanosensors for biological and non-biological samples due to their inherent size dependent fluorescence property. The last decade has witnessed revolutionary development of nanoparticle for different biomedical applications (C. V Durgadas *et al.,* 2011; Nair *et al.,* 2014, 2015, 2017; Nair & Jayasree 2016; Nair, Santhakumar & Jayasree 2018; Santhakumar *et al.,* 2018; Saraswathy *et al.,* 2014a, 2014b); especially quantum dot based nanosensors with high selectivity and sensitivity compared to conventional sensors.

2.1.2.Cadmium selenide quantum dots for the detection of lead and zinc

Lead is one of the heavy metals which is restricted by the European Union due to its toxicity. This metal is non-biodegradable and accumulates in the ecosystem, causing harm to human health (Vries, Römkens & Schütze 2007). The pollution due to lead is the persisting issue and gives long-lasting effects in the

environment due to the circulating effect of the ions (Park, Lee & Jung 2013). Low level of lead exposure can cause neurological, reproductive, cardiovascular, developmental disorders, and severe problems in children, including slowed motor responses, decreased IQs, and hypertension (Vries, Römkens & Schütze 2007). Consequently the detection of lead in blood as well as the water is very important.

There are various reports available for the lead detection using nanomaterials. In one of the studies, citrate coated gold nanoparticles were used to detect lead (II) ion. An increase in concentration of lead causeda change in the absorption of colloidal gold. The higher amount of lead (II) ion induces aggregation, thereby changing the color of the solution (Berlina & Sharma 2014). Another study has been reported on BSA-capped gold nanoparticles for the detection of lead ion. In the presence of lead ion leaching of gold nanoparticle (Au-NPs) occurred, the reaction happens only in the presence of thiosulfate (S_2O3_2) and 2-mercaptoethanol (2-ME) in it. The presence of lead ion accelerated the dissolution of the 2-ME/$S_2O_3^2$–Au NPs@BSA into solution, leading to a dramatic decrease in the absorption (Lee *et al.,* 2012). In one of the studies, glutathione capped gold nanoparticles were used for the detection of lead (II) ion. In this case, the presence of lead (II) ion increases the aggregation of gold nanoparticles, which leads to a change in the absorption of the nanoparticles (Zhong, Liu & Liu 2015). A sensitive and label-free DNAzyme-based unmodified gold nanoparticles sensor for Pb^{2+} were reported. The detection was based on the fact that unfolded single-stranded (ss) DNA could be adsorbed on the citrate protected gold nanoparticles while double-stranded (ds) DNA could not. It leads to aggregation of nanoparticles which was recorded using colorimetric techniques. Similarly,they also reported the detection of lead using gold nanoparticle with modified DNAzyme using dynamic light scattering techniques (Wei *et al.,* 2008). Colloidal gold nanoparticles also used for the detection of lead ions using the change in absorption (Miao & Shuai 2011). Ali *et al.,* reported the detection of lead (II) ion using glutathione capped cadmium tellurium (CdTe) and ZnCdSe quantum dots. It was found out that upon addition of lead (II) ion, a fluorescence quenching was observed due to carboxylate-GSH-lead (II) coordination (Ali *et al.,* 2007). Another study put forward the detection of the lead ion using aptamer coated graphene oxide mixed cadmium selenide (CdSe)/zinc sulphide (ZnS)(CdSe/ZnS). On

conjugation with lead, an energy transfer mechanism enables fluorescence quenching (M. Li *et al.*, 2013).

Zinc is one of the essential trace element in the human body. 2g of zinc content has been estimated for the total body (Maret & Sandstead 2006). Zinc has mainly three functions in the human body viz., catalysis, adjustment, and structure (Gmoshinskiĭ et al,. 2018). A high amount of zinc in the body will cause metal fume fever, reduce serum high-density lipoprotein-cholesterol levels, and leads to iron and copper deficiency. Accordingly, it is essential to detect the level of zinc ion in human blood. There are various reports available for zinc detection using the nanoparticle approach. In a report, the derivative of azamacrocycle (TACN (1,4,7-triazacyclononane), cyclen (1,4,7,10-tetraazacyclododecane), and cyclam (1,4,8,11-tetraazacyclotetradecane) of CdSe/ZnS core/shell quantum dots were used for the fluorescent detection of zinc ions. The presence of azamacrocycles disturbs the process of radiative recombination in quantum dots. When Zn (II) ions introduced, it takes the crown positionin azamacrocycle, leading to fluorescence enhancement(Ruedas-rama & Hall 2008). Xu *et al.,* reported fluorescent CdTe quantum dot for the detection of zinc and cadmium ions. In this study, the fluorescence of quantum dots were quenched in the presence of sulfur anion, and it retains the fluorescence in the presence of zinc or cadmium ion. This retaining fluorescence intensity was quantitatively correlated with the concentration of ions (Xu *et al.,* 2011).

In another study, label-free silver nanoparticle was used for the detection of zinc ions. In thepresence of zinc ions, label-free silver nanoparticles undergo aggregation, leading to a change in color from yellow to forest green (Uni, Liu & Lu 2003). Rastogi *et al.*, reported the synthesis of 8-aminoquinoline (N-(quinolin-8-yl)-2-(3 (triethoxysilyl)propylamino)acetamide (QTEPA) grafted on silica nanoparticles (SiNPs) for divalent zinc ion detection. They demonstrated the detection of zinc ion in HCl buffer with pH 7.22, in yeastcell (Saccharomyces cerevisiae) suspension, and in tap water (Rastogi *et al.,* 2011). A fluorescent sensor was developed for the detection and removal ofzinc using Fe_3O_4@SiO_2 core-shell nanoparticles functionalized with 8-chloroacetylaminoquinoline (Xu *et al.,* 2013). The detection of divalent zinc ions reported using fluorescent properties of upconversion lanthanide

nanoparticles(Peng *et al.,* 2015). A quinoline derivative functionalized with carbon dots used for the detection of zinc ions. The sensor used for the intracellular detection of zinc within 1 minute (Zhaomin *et al.,* 2014).

2.2.Gold based fluorescent nanoparticle for sensing and imaging-cysteine gold cluster for the detection of dopamine and cellular imaging

Gold nanoclusters are atomic-sized particles with a size less than 2 nm, which is too small to exhibit surface plasmon resonance(Qu et al. 2015). These clusters possess high fluorescence due to their extremely small size. The ligand present on its surface influences the fluorescence of gold nanoclusters due to the charge transfer from the ligand or direct electron donation from ligand to the metal core (Wu & Jin 2010). Fluorescence properties of gold nano clusters were used for sensing applications. Yu *et al.,* developed a chitosan oligosaccharide lactate(Chi) functionalized gold cluster to form Au NCs (Au NCs@Chi) for the detection of hydrogen sulfide. It had high fluorescence quantum yield, and FRET based sensing was used for the detection of H_2S. Using wavelength-ratiometric and time-resolved luminescence imaging (TLI) techniques its were able to detect exogenous and endogenous H_2S *in vitro* and *in vivo* (Wu & Jin 2010). A gold cluster based system was developed for the detection of biomolecules like urea from whole blood and milk (Nair, Philips & Jayasree 2013). Dopamine is a molecule from the family of catecholamine and phenethylamine. It plays an important role in the brain as a neurotransmitter. It acts as a paracrine messenger outside the brain and a vasodilator in blood vessels. Also, in the kidney,it helps in sodium excretion and urine output. In the pancreas, dopamine reduces insulin production. Similarly, in every part of the body, dopamine plays a specific function. Therefore, the imbalance levelof dopamine concentration in the blood streams is a sign of some disorders in the body, such as Alzheimer's, Parkinson's, schizophrenia, addiction, bipolar disorders, binge eating, and gambling. Soit is essential to develop the strategies for dopamine detection. Various reports are available for dopamine detection using different approaches employing nanoparticles. In one of the studies, dopamine was detected by measuring

the fluorescence of polydopamine nanoparticles, which was produced in the presence of an acid and base (Yildirim & Bayindir 2014). Zhang et al., studied the detection of dopamine using fluorescent silicone nanoparticle. The addition of dopamine to the silicon nanoparticle,its fluorescence, quenches as the concentration of dopamine increases(Zhang *et al.,* 2015). In another study, carbon dots were used for the detection of dopamine using fluorescence enhancements with an increase in concentration (Baruah *et al.,* 2014). Rostami *et al.,* developed a colorimetric sensor with task-specific ionic liquid (TSIL) functionalized silver nanoparticle for dopamine. In the presence of dopamine, the hexagonal TSIL silver nanoparticles converted to spherical-shaped nanoparticles. A color change from green to red was observed in addition to dopamine due to this change in morphology of TSIL-Ag NPs (Rostami *et al.,* 2018). Su*et al.,* developed a dopamine sensor using gold nanoparticle, where the amino and hydroxyl group of dopamine is adsorbed on the surface of gold nanoparticles. These gold nanoparticles undergo aggregation on interaction withCu^{2+} ions. Here Cu^{2+} acts as a discriminator linker for dopamine detection by inducing aggregation of gold nanoparticles (Su *et al.,* 2012). Zheng *et al.,* introduced a dopamine sensor using unmodified gold nanoparticle synthesized with 58-mer dopamine-binding aptamer (DBA). Here, DBA acts as a recognition element and gold nanoparticles (AuNPs) acts as probe. Upon addition of dopamine the structure of aptamer changed from random coil to a rigid tertiary structure like a pocket and this change has been evaluated by circular dichroism spectroscopic experiments. It also facilitates aggregation of gold nanoparticle which induces color change from red to blue. Concentration of dopamine detected using both circular dichroism and absorbance (Zheng, Wang & Yang 2011) of AuNPs. Govindaraju*et al.*,reported BSA capped gold cluster for dopamine detection from cerebrospinal fluid (Govindaraju*et al.,* 2017).

The properties of gold nanoclusters depend on the number of gold atoms and nature of the ligands. Using different surface ligands, one can tune the properties of gold nano cluster. In turn, the applications of gold clusters in sensing and other biological fields were reported (Govindaraju *et al.,* 2017).

2.3. Fluorescent multifunctional gold based system for imaging and therapy

The shape of the nanocrystal is an important parameter which decides the physical and chemical properties of the material. Gold nanoparticle having shapes other than spherical exhibit anisotropic optical and electronic responses,which are determined by the morphological aspects (Klar *et al.,* 2010).

2.3.1. Gold nanorod-MTX (Mitoxantrone) nanomaterial for *in vitro* cancer imaging and therapy

Gold nanorod with NIR absorption is a good photothermal agent. In cancer treatment, they are acting as a source for temperature generation upon laser irradiation. Chemotherapy is the treatment of cancer using the traditional drug. Mitoxantrone is a conventional cancer drug used for the treatment of leukemia and other types of cancers. This drug destroying cancer cells as well as normal defense cells. So the nonspecificity is the major drawback of this drug.

There are various studies reported for the combined therapy of gold nanorod with cancer drugs, and some of the recent reports are pointing here. Gold nanorod-doxorubicin used for combined therapy with the help of polymersomes, which is stimulus-responsive. The imaging and treatment efficacies were evaluated *in vitro* and *in vivo* (Liao *et al.,* 2015). In one of the studies,a biodegradable micelles were prepared by coating gold nanorods (GNRs) with synthesized stimuli-responsive thiol-end capped ABC triblock copolymer [poly(acrylic acid) -b-poly(N-isopropylacrylamide)-b-poly(εcaprolactone)-SH; PAA-bPNIPAAm-b-PCL-SH]. Anti-cancer drug doxorubicin (DOX) was conjugated onto it by electrostatic force, and the drug releases its pH-thermal responsive release of drug and treatment were studied (Abbasian *et al.,* 2017). In another report,GNR was decorated with camptothecin, a cancer drug through chemical bonding. Upon acidic pH, laser irradiation drug will release, and photo-chemo therapy was evaluated *in vitro* (Yang *et al.,* 2018). In another report, gold nanorod conjugated with doxorubicin used for the treatment of liver cancer. Here, GNR acts as photothermal agent as well as a carrier for the drug. The combined therapy effect was proved *in vitro* as well as *in vivo* in tumor-bearing mice (Chen *et al.,* 2018). In another report,the capping agent

CTAB of GNR replaced with truncated Evans blue. GNR covered with truncated Evan blue helps to hold the drug molecule, human serum albumin/hydroxycamptothecin (HSA/HCPT). The system used as a chemo-thermal therapy agent which is superior touse chemo and photothermal therapy separately (Wang *et al.,* 2018). In another study,mesoporous silica-coated GNRs functionalized with hyaluronic acid-RGD peptide (Huimin *et al.,* 2018). It's used for the delivery of doxorubicin in cancer treatment.

2.3.2. Gold nanorod-PPIX (Protoporphyrin IX) nanomaterial for cancer imaging and therapy

Gold nanorod(GNR) has good photothermal properties due to NIR absorption. Upon conjugating GNR with PS will impart additional photodynamic property. GNR, along with Al (III) phthalocyanine chloride tetrasulfonic acid ($AlPcS_4$), were used for combined PTT and PDT. Quenching in fluorescence was observed in the complexation stages with $AlPcS_4$, and on reaching the tumor site, the fluorescence intensity enhancement was observed. The results obtained suggested that combined therapy gives better results to single treatment(Jang *et al.,* 2011b). Jian Wang *et al.,* investigated the treatment efficiency of chlorine e6 (photosensitizer) and aptamer switch probe (ASP)linked gold nanorod. ASP target the cancer cells, and changes its confirmation leads to the release of PS molecule, thereby facilitating singlet oxygen generation (Wang *et al.,* 2013). Wen-ShuoKuo *et al.*,studied indocyanine conjugated gold nanostructure for cancer therapy. The use of indocyanine was limited due to its chemical degradation in water. In the presence of GNR, its stability is increasing, and they used the system for PDT and PTT(Kuo*et al.,* 2012). One of the reports showed rose-bengal, a fluorescent molecule conjugated with gold nanorod for the treatment of cancer. Singlet oxygen generation capacity of rose-bengal was checked with a 532 nm laser irradiation in GNR system. An 810 nm laser irradiation leads to temperature generation due to the presence of GNRs (Wang *et al.,* 2014). In another report, methylene blue loaded on silica-coated GNR for cancer treatment. The presence of methylene blue resulted in PDT and photothermal property due to GNRs were evaluated (Seo *et al.,* 2014) in cancer condition. The PDT and PTT efficiency of silylated zinc phthalocyanine (ZnPc) anchored silica-

coated GNRswas investigated with irradiation of NIR laser. Hyaluronic acid (HA) was further grafted on the system for targeting to CD44 antigen (Tham *et al.,* 2016) present in cancer cells.

2.4. Hybrid fluorescent gold based nanomaterial for imaging and therapy- gold nanorod-gold cluster hybrid nanomaterial for cancer imaging and therapy

Hybrid nanoparticles are combinations of two or more nanostructures with combined properties of parental nanparticlesfor biomedical applications. In 2007, a gold-coated iron oxide hybrid nanoparticle for MR and optical imaging was reported, and it used for photothermal therapy after laser irradiation (Larson, Bankson & Aaron 2007). Mathew Hembury *et al.,* developed a hybrid gold quantum cluster-gold particle in a mesoporous silica matrix called gold–silica quantum rattles for fluorescence imaging and therapy. It reported that the instability of the gold quantum cluster in aqueous media limits its use in the medicinal field. So to increase the aqueous stability, they incorporate it into mesoporous silica along with gold nanoparticle (Hembury *et al.,* 2015). In another report, quantum dots which are having emission property incorporated into a single-walled carbon nanotube, which is having photothermal property. This hybrid quantum dots- single-walled carbon nanosystem after conjugation with folic acid, was used for cancer cell imaging and therapy (Nair *et al.,* 2014). A gold-silver hybrid system developed for the treatment of certain infections. Silver ions have already proven to have an antibacterial property, and it cannot be monitor using normal techniques. So in this article, they were used photoacoustic imaging, with gold nanorod's photoacoustic nature. In the hybrid system, they coated silver over gold nanorod; in the presence of chemical ferricyanide solution (1 mM) silver ions will ooze out and showed the antibacterial property. Gold and silver nanohybrid materials make use of the properties of both gold and silver(Kim *et al.,* 2018).

Chapter 3

Materials & Methods

This chapter elucidates the materials and methods used for this thesis work.

3.1.Cadmium selenide quantum dots for simultaneous detection of copper and creatinine

3.1.1. Materials

The chemicals such as cadmium chloride monohydrate (SRL chemicals), selenium powder (Sigma Aldrich), sodium sulphite (Merck), cysteine hydrochloride (Sigma Aldrich), 1-ethyl-3-(3-dimethylaminopropyl)carbodiimide (EDC) (Sigma Aldrich) picric acid (PA) (Merck), zinc oxide, etc. were used without any further purification.

3.1.2. Synthesis of quantum dot (Qd)

Selenium stock solution was prepared by mixing sodium sulphite (0.4 M) and selenium metal powder (0.2 M) in 25 mL DI water at 75^{o}C for 3h. 25 mg cadmium chloride (2.5 mM, 25 mL) was treated with 131.5 mg of cysteine (15 mM, 25mL). The pH of the solution was adjusted to 11.5 before adding the selenium stock. 125 µl (5mM, 25 mL) selenium was added to the reaction mixture at 80^{0}C. The whole reactions were carried out at 590 rpm for 12h. Qds were purified by centrifugation using the isopropanol-water mixture at 10000 rpm for 15 min.

3.1.3. Conjugation of picric acid with Qd (PAQd)

Purified Qds (c.a. 5mg) were treated with 12 mg (12.2 mM, 5 mL) of EDC for 30 min. After 30 min 14 mg of picric acid (PA) (12 mM, 5 mL) was added at room temperature, and the reaction mixture were stirred at 520 rpm for 2h. PAQd were purified by centrifugation at 8000 rpm for 10 minutes.

3.1.4. Characterisation

Qd and PAQdwerecharacterised using fourier transform infrared spectrometer (FT-IR) Carry 600 (Agilent Technologies) to confirm the functionalization and chemical changes after the formation of a complex with EDC and PA. FTIR spectra were recorded in the range 400 to 3600 cm^{-1} in transmission

mode using KBr pellet method spanning over 32 scans. NMR analysis was also used to confirm the chemical changes that happened during the formation of PAQd. Zeta potential at every step of synthesis was investigated using Malvern ZetasizerNanoZS 90 to investigate the change in the surface charge after functionalization. Surface morphology was confirmed using TEM (100kv JEM-2010 HiTachi-JEOL, Tokyo, Japan) analysis. UV-visible spectroscopy was done using Shimadzu UV spectrometer- UV 2600 for analysis of the optical property and functionalization of the quantum dots. The emission properties of the materials were studied using Varian Carl Eclipse fluorescence spectrophotometer at different excitation wavelengths. All the cell imaging experiments were performed using Olympus IX83 Inverted Fluorescence microscope (Tokyo, Japan) equipped with a cooled CCD camera (XM10, monochrome, Olympus), a metal halide lamp (X-Cite, series 120PC Q), an objective lens (LUCPLFLN 40X PH/0.6, include 100X, Olympus), excitation filters (360-370, 470-495, 540-585), dichroic mirrors (DM410, DM505, DM595), and emission filters (420-460, 510-550, 600IF) controlled with CellSens Imaging software.

3.1.5. Sensing of copper and creatinine from aqueous solution

Different concentrations of copper and creatinine in the range from nano molar (nM) to milli molar (mM) were prepared and were incubated with 1mg/mL concentration of PAQd for 30s. Variations in fluorescence intensity were monitored at 531 nm and 440 nm for copper and creatinine, respectively.

3.1.6. Sensing of copper and creatinine from blood serum

5 mL of human blood was collected from a healthy individual without any bias. The serum was separated and diluted with normal saline and divided into different batches. Each batch was incubated with varying concentrations of copper and creatinine (nm to mM). Serum samples with different levels of copper and creatinine were added to 0.01 mg/mL of PAQd, and changes in the fluorescence intensity were monitored at 531 nm and 440 nm. The institutional ethics committee approved the blood study; B form number SCT/IEC/594/APRIL-2014.

3.1.7. Basic cell culture

MDA MB-231 (human breast cancer cells) and L929 (mouse alveolar and adipose connective tissue cells) purchased from ATCC were used for the *in vitro* analysis. L929 and MDA MB-231 cells were cultured using Dulbecco's Modified Eagle's Medium (DMEM). The media was supplemented with 10% (v/v) fetal bovine serum (FBS), 100 μgmL^{-1}penicillin, 100 μgmL^{-1} streptomycin and 2.5 μgmL^{-1} amphotericin B. The entire cells were maintained in an incubator (5% CO_2 at 37°C). The 85-95% of confluent cells were harvested using trypsin-ethylenediamine tetraacetic acid and sub-cultured in culture dishes at a seeding density of $0.25x10^6$ cells per millimeter.

3.1.8. Cytotoxicity studies

L929 and MDA MB-231 cells were seeded onto a 96-well plate with a cell density of $1x10^4$ cells/well and keep it for 24h of incubation; the cells was further incubated with fresh media containing Qd and PAQd concentrations of 1, 0.5, 0.1, 0.05, 0.01, 0.005 and 0.001 mg/mL for 72 h. Then, the materials containing media was removed and replaced with 100 µl of fresh serum-free DMEM medium containing 3-(4, 5-dimethylthiazol-2-yl)-2,5-diphenyltetrazolium bromide (MTT-10 µl, 5 mg/mL). Following 3h incubation period, the MTT formazan crystals were dissolved using DMSO (100 µL). Absorbance at 570 nm was measured using a microplate reader (Synergy H1 hybrid multi-model microplate reader, Bio-Tek). The relative percentage cell viability (%) for each material calculated.

3.1.9. Intracellular copper and creatinine detection

L929 and MDA MB-231 cells were seeded in a four-well plate and allowed to grow in the DMEM medium for 24 h. Then each wellwas incubated with different concentrations of copper (20 µM and 3 mM) and creatinine (3 nM and 0.033 mM). After half an hour incubation, analyte containing media was removed and added the fresh media, which contain 0.01 mg/mL of PAQd, for 3h. For the control group,thesame cell was used without the incubation of analytes. For the detection, fluorescence microscopic images were captured with the same exposure and gain time. The intensity of the images was calculated using grayscale readings.

3.1.10. Extracellular copper and creatinine detection

L929 and MDA MB-231 cells were seeded in a four-well plate and allowed to grow in the DMEM medium for 24 h. Then each well was incubated with different concentrations of copper (20 µM and 3 mM) and creatinine (3 nM and 0.033 mM) followed by immediate addition of 0.01 mg/mL of PAQd. For the control group the same cells without the incubation of analytes were used. For detection, fluorescence microscopic images were captured with the same exposure and gain time. The intensity of the images was calculated using gray scale readings.

3.2. Cadmium selenide quantum dots for the detection of lead and zinc

3.2.1. Materials

Reduced glutathione, Selenium powder, and sulfamethoxazole were purchased from Sigma Aldrich. Sodium sulphite, isopropanol, methanol, zinc oxide and lead nitrate were purchased from Merck andcadmium chloride monohydrate was purchased from SRL chemicals. All chemicals were used without any further purification.

3.2.2. Synthesis of glutathione capped cadmium selenide (GQd)

4 mg (1 mM, 20 mL) of cadmium chloride was treated with 18.13 mg (2.95 mM, 20 mL) of reduced glutathione and adjust the pH to 11.5. Then 50 µl of selenium stock (0.5 mM, 20 mL (dissolving selenium metal powder to sodium sulfite in 0.2:0.4M ratio at 75^0C for 3 h in aqueous media as explained in section 3.1.2)) was added at 60^0C followed by stirring at 590 rpm for 12 h. Glutathione stabilized Qds (GQd) were purified by centrifugation using isopropanol-water (1:1) mixture at 10000 rpm for 15 minutes.

3.2.3. Functionalisation of GQd with sulfamethoxazole (SMGQd)

GQd treated with 18 mg (4.7 mM, 10 mL) of sulfamethoxazolefor 24 h at neutral pH and room temperature. SMGQd was purified using centrifugation at 8000 rpm for 10 minutes.

3.2.4. Characterisation

GQd and SMGQd was characterised using fourier transform infrared spectrometer Carry 600 (Agilent Technologies FT-IR) to confirm the functionalization and chemical changes with GQd. FT-IR spectra were recorded in

the range 400 to 3600 cm^{-1} in transmission mode using the KBr pellet method spanning over 32 scans. NMR analysis was also used to confirm the chemical changes that happened in the formation of SMGQd. Every step of synthesis was investigatedusingzeta potential analyzer, make Malvern ZetasizerNanoZS 90 for studying the change in surface charge. Surface morphology was confirmed using TEM (FEITecnai G2 F30 S -Twin TEM 300 kV) analysis. UV-visible spectroscopy was studied using Shimadzu UV spectrometer- UV 2600, to confirm the optical property and functionalisation of SMGQd. The emission properties of the materials were studied using Varian Carl Eclipse fluorescence spectrophotometer at different excitation wavelengths.

3.2.5. Detection of zinc and lead

Different concentrations of zinc (nM – mM) and lead (pM-mM) were added to 1 mg/mL solution of SMGQd and GQd respectively. The emission profile of solutions was recorded using a spectrofluorometer at 420 nm excitation.

3.3. Cysteine gold cluster for the detection of dopamine and cellular imaging

3.3.1. Materials

Chloroauric acid ($HAuCl_4$), sodium borohydride ($NaBH_4$), sodium hydroxide (NaOH), and cysteine were purchased from Sigma Aldrich. All cell culture media (F12 and DMEM) and reagents (MTT, FBS, and Antibiotic – antimycotic solution) were purchased from HiMedia.

3.3.2. Synthesis of gold cluster (AuC)

Chloroauric acid (2.5 mM) and cysteine (1mM) were mixed in the ratio of 2:1(w/w) followed by NaOH (10 mM) till the solution faded its color or till it became basic. Then 100 µl of sodium borohydride (10 mM) was added and stirred for 30 min. The product was used without any further purification. The synthesis was optimized using different concentrations of reactants.

3.3.3. Characterisation

AuC was characterised by Fourier transform infrared spectrometer Carry 600 (Agilent Technologies FT-IR) to analyze the functionalisation. FT-IR spectra were recorded in the range 400 to 3600 cm^{-1} in transmission mode using the KBr pellet method spanning over 32 scans. Zeta potential at every step of synthesis of AuC was investigated using Malvern ZetasizerNanoZS 90 to investigate the change in charge. Surface morphology was confirmed using TEM (100kv JEM-2010 HiTachi-JEOL, Tokyo, Japan) analysis. Shimadzu UV spectrometer- UV 2600 used for absorbance spectra measurements. The emission property was studied using Varian Carl Eclipse fluorescence spectrophotometer at different excitation wavelengths. A spectrum at every pixel was taken (Scan Range: 40 x 40 μM2, 100 x 100 pixel, 10,000 spectra) using a 20 x Nikon objective. The sample was excited with a 10 mW power, 633 nm frequency doubled Nd:YAG laser. Suitable cells were focused and scanned with an integration time of 0.5s using a video camera.The cell imaging experiments were performed using Olympus IX83 Inverted fluorescence microscope (Tokyo, Japan) equipped with a cooled CCD camera (XM10, monochrome, Olympus), a metal halide lamp (X-Cite, series 120PC Q), objective lens (LUCPLFLN 40X PH/0.6, include UPLFLN 100X/0.3, Olympus), excitation filters (360-370, 470-495, 540-585), dichroic mirrors (DM410, DM505, DM595), and emission filters (420-460, 510-550, 600IF) controlled with CellSens Imaging software.

3.3.4. Sensing of dopamine

Different concentrations of dopamine (fM-mM) were added to the solution containing 1mg/mL of AuC, and fluorescence intensity at 645 nm was measured in aqueous and PBS solution. Cellular dopamine detection was done in C6 glioma cells. Cells were seeded on four well plates after 24 h,and different concentrations of dopamine were incubated for 3h. Then 1 mg/mL solution of AuC was added, and fluorescence intensity was recorded.

3.3.5. Cellular imaging using AuC

Different concentrations of AuC were incubated with L929 and MDA MB-231 cell lines and evaluated cytotoxicity using MTT (protocol is already given). For cellular imaging, cells were seeded in four-well plates, and after attaining 80% confluence, AuCs were incubated for 3h. After that, cells were stained with DAPI

and washed with PBS for 3 times. Images were recorded using a fluorescence microscope.

3.4. Gold nanorod-MTX (Mitoxantrone) nanomaterial for in vitro cancer imaging and therapy

3.4.1. Materials

Chloroauric acid ($HAuCl_4$), thioamine polyethylene glycol (thio-Amino PEG) andcetyltrimethyl ammonium bromide (CTAB), mitoxantrone and folic acid were purchased from Sigma Aldrich. Ascorbic acid, sodium borohydride, and silver nitrate were purchased from Merck. All cell culture media (DMEM) and reagents (Hoesch, MTT, FBS, antibiotic-antimycotic, acridine orange, and ethidium bromide) were purchased from HiMedia.

3.4.2. Preparation of gold nanorod (GNR)

Gold nanorods were synthesised using seed-mediated growth procedure. Seed solution was prepared by treating 0.25 mL of 2.2 mM $HAuCl_4$ with sodium borohydride ($NaBH_4$) (100 µL of 10 mM) as a reducing agent and CTAB (3 mL of 0.1 M) as a stabilizing agent. The solution was kept at 20 ^{0}C for 3 h. The growth solution was prepared by treating 0.2 mM $HAuCl_4$ (3.3 mL) with CTAB (50 mL of 0.1M), $AgNO_3$ (250 µL of 0.01 M), and ascorbic acid (250 µL of 0.1 M) followed by 166 µL of seed solution. The solution was kept overnight for the growth of the nanorod at room temperature. On completion of the growth, the solution was kept at 4^0 C for 1h, and then at room temperature to remove the excess CTAB as sediment. The supernatant collected was centrifuged at 1200 rpm for 20 minutes, and the centrifugation was repeated thrice to purify the GNR.

3.4.3. Surface modification of GNR with thioamino polyethylene glycol (PGNR)

GNR was stirred with 1 mg of thioamino PEG for two hours. The synthesized material was recovered using centrifugation at 22000 rpm for 15 minutes and washed twice to get PGNR.

3.4.4. Preparation of cancer targeting system (FPGNR)

PGNR was treated with half the concentration of folic acid through EDC/NHS coupling. 3mg/5µL of EDC was treated with folic acid at pH 4, and the

solution was stirred for 3 h. Then 3mg/5µL of NHS was added to the solution and kept stirring for 3h. After 15 minutes, PGNR was added to the EDC/NHS mixture, and the solution was stirred for another 12 h at pH above 9 and then centrifuged at 22000 rpm for 15 minutes. The pellet was washed twice to remove the unreacted folic acid. The construct was named as FPGNR.

3.4.5. Encapsulation of mitoxantrone(MTX) drug to FPGNR (MTX@FPGNR)

FPGNR was sonicated with 0.5 mL of 1.5 mg/mL MTX solution for 15 minutes. Then the solution was stirred for 12 h at pH 4.The products were washed by centrifugation with distilled water for 15 minutes at 22000 rpm to remove the unreacted MTX. The construct was named as MTX@FPGNR.

3.4.6. Characterisation

GNR, PGNR, FPGNR, and MTX@FPGNR were characterised by fourier transform infrared spectrometer Carry 600 (Agilent Technologies) to confirm the functionalisation and chemical changes after functionalisation of GNR. FT-IR spectra were recorded in the range 400 to 3600 cm^{-1} in transmission mode using the KBr pellet method spanning over 32 scans. Zeta potential at every step of synthesis was investigated using Malvern Zetasizer NanoZS 90 to investigate the change in charge after functionalisation. Surface morphology was confirmed using TEM (100kv JEM-2010 HiTachi-JEOL, Tokyo, Japan) analysis. UV-visible spectroscopy was using Shimadzu UV spectrometer- UV 2600 to confirm the functionalisation of GNR. The emission property was studied using Varian Carl Eclipse fluorescence spectrophotometer at different excitation wavelengths. The heat generation potential of the material was studied by irradiating with 808 nm laser (MDL III). Raman imaging of the cells and surface-enhanced Raman scattering were investigated with the spectral imaging mode of the confocal Raman microscope (alpha300R, WITec Inc. Germany). A spectrum at every pixel was taken (Scan Range: 40 x 40 µM2, 100 x 100 pixel, 10,000 spectra) using a 20 x Nikon objective. The sample was excited with a 10 mW power, 633 nm frequency doubled Nd:YAG laser. Using the integrated video camera, a suitable cell was focused and scanned with an integration time of 0.5s. All the cell imaging experiments were performed using Olympus IX83 Inverted fluorescence microscope (Tokyo, Japan) equipped with a cooled CCD camera (XM10, monochrome, Olympus), a metal halide lamp (X-Cite, series 120PC

Q), objective lens (LUCPLFLN 40X PH/0.6, include UPLFLN 100X/0.3 , Olympus), excitation filters (360-370, 470-495, 540-585), dichroic mirrors (DM410, DM505, DM595), and emission filters (420-460, 510-550, 600IF) controlled with CellSensimaging software.

3.4.7. Drug release

In vitro drug release study was doneusing fluorescence spectroscopy. 1mg/mL of MTX@FPGNR was weighed separately and divided into four batches. One batch was dissolved in normal distilled water (pH 7) and another batch in DI water (pH 4). Similar batches were chosen for laser irradiation. Fluorescence of each sample was pre-recorded, and all the samples were diluted to 5 mL with solvent, as mentioned above. At different time intervals of 1, 2, 4,8,12, and 24 h, one batch of each sample was irradiated with 808 nm laser for 1.30 S with 1W power. All the four samples were centrifuged at 15000 rpm for 10 minutes. 1 mL of supernatant was collected and then made up to 5 mL with fresh solvent. The fluorescence intensity of each collection was recorded with 600 nm excitation. The ratio of the intensity of 668 and 711 nm was recorded, which are the characteristics emissions of MTX drug. This ratio is directly proportional to the concentration of MTX drugs.

3.4.8. Cell culture

Two cancerous cell lines over expressing different levels of folate receptors were chosen for this study: HeLa (human cervical cancer) and C6 glioma (rat glial tumor). Normal fibroblast cell line L929 (mouse alveolar and adipose connective tissue) was used as a folate receptor-negative control group. L929 and HeLa cells were cultured in Dulbecco's Modified Eagle's Medium supplemented with 10% (v/v) fetal bovine serum (FBS), 100 μmL^{-1} penicillin, 100 μgmL^{-1}streptomycins and 2.5 µgmL-1 amphotericin B. C6 glioma cell line was cultured in Dulbecco's Modified Eagle's Medium/Nutrient mixture F12 Ham (DMEM/F12, 1:1) supplemented with 1 mM sodium pyruvate, 10 % (v/v) fetal bovine serum (FBS), 100 μmL^{-1}penicillin, 100 μgmL^{-1}streptomycins and 2.5 μgmL^{-1} amphotericin B. All the cell lines were maintained in a humidified atmosphere with5% CO_2 at 37°C. All experiments were performed using the following protocol: cells grown to reach 85-95% confluency were harvested with trypsin-ethylenediaminetetraacetic acid and sub-cultured in culture dishes at a seeding density of $0.25x10^6$ cells per millimeter.

3.4.9. *In vitro* cellular cytotoxicity

The cellular cytotoxicity of all constructs was tested in all three cell lines, L929, C6, and HeLa. All cell line was seeded onto a 96-well plate with a cell density of $1x10^4$ cells/well. After 24 h of incubation, the cells were further incubated with fresh media (100 μL per well) containing all constructs in concentrations of 2, 1, 0.5, 0.25, and 0.125 mg/mL for 24 h, respectively. Then the constructs containing media were removed and replaced with 100 μL of fresh DMEM containing 3-(4, 5-dimethylthiazol-2-yl)-2, 5-diphenyltetrazolium bromide (MTT-10 μL, 5 $mgmL^{-1}$). Following 4 h of incubation period, the insoluble MTT formazan crystals formed were dissolved with DMSO (100 μL). Absorbance at 570 nm was measured using a microplate reader (Synergy H1 hybrid multi-mode microplate reader, Bio-Tek). The relative cell viability (%) for each construct related to the control cells was finally calculated.

3.4.10. Cancer cell targeting potential of MTX@FPGNR

HeLa, C6, and L929 cell lines were evaluated for the uptake of MTX@FPGNR using fluorescence microscopy. All the cells were trypsinized and seeded in 4 well plates (10^4 cells/well) for further investigation. Then the cells were incubated with 1 mg/mL of MTX@FPGNR for 6 h. After incubation, the cell lines were washed three times with PBS to remove the excess material in media and then stained with nuclear specific Hoechst stain for 10 min. Excess stain was removed by PBS wash, and the cells were imaged under the inverted fluorescence microscope.

3.4.11. Evaluation of drug release in cancer cells

3.4.11.1.Fluorescence technique

HeLa, C6 cell lines were evaluated for drug release using fluorescence microscopy. All the cells were trypsinized and seeded in 4 well plates (10^4 cells/well) for further investigation. Then the cells were incubated with 1 mg/mL of MTX@FPGNR for 6 h. After incubation, the cell lines were washed with PBS three times to remove excess material in the media. The cells were divided into two batches containing each cell and were irradiated with 808 nm laser with 1W power for 1.30s. Then each cell were stained with nucleus specific Hoechst stain for 10

min. Excess stain was removed by PBS wash, and the cells were imaged under the inverted fluorescence microscope.

3.4.11.2. Raman spectroscopy

Both HeLa and C6 cancer cell lines were cultured in labtekfour-well chamber slides. After the cells attained 50% confluency, the final construct MTX@FPGNR was incubated at a concentration of 1 mg/mL in both the cell lines for 6 h, to get maximum uptake. One set of construct treated cells was irradiated with 808 nm laser, and another set was kept without laser irradiation. These construct treated cells with and without laser irradiation were mapped by Raman microscope to confirm the drug release, along with untreated HeLa and C6 cells as a control to observe the changes in the Raman signatures.

3.4.12. Validation of photothermal and chemotherapies using MTX@FPGNR

3.4.12.1.Quantitative analysis of photothermal treatment

For the quantitative determination of photothermal therapy, HeLa and C6 cells were used. Both cells were seeded in 96 well plates at a density of 10,000 cells per well and incubated for 24 h. Different concentrations of GNR, PGNR, FPGNR and MTX@FPGNR were prepared using cell culture medium. The existing medium in the wells was replaced with 100 µL of fresh medium containing the materials and incubated for different time periods. The wells were irradiated with 808 nm laser for 1.30 s with a laser power of 1W. Then MTT assay was carried out. Similarly, for chemotherapy MTX alone was incubated with different cell lines for 6h.

3.4.12.2. Qualitative analysis of photothermal treatment

For the qualitative microscopy evaluation of photothermal therapy, both the cancer cell lines were treated with 1 mg/mL of MTX@FPGNR for six h and the cells were irradiated with a laser. Live dead assay was done using acridine orange/ethidium bromide staining. 1 µL of each dye was added to 1 mL of PBS and 100 µL of solution was added to each well and the cells were imaged under a fluorescent microscope.

3.5. Gold nanorod-PPIX nanomaterial for cancer imaging and therapy

3.5.1. Preparation of gold nanorod (GNR & GSH@GNR)

Gold nanorods were synthesised using seed-mediated procedure. Seed solution was prepared by treating 2.2 mM $HAuCl_4$ with 10 mM $NaBH_4$ as a reducing agent and 0.1 M CTAB as a stabilizing agent in 3 mL. The solution was kept at 20^{o}cfor 3hrs. The growth solution was prepared by treating 2.2 mM of $HAuCl_4$ with 0.1M of CTAB, 0.01 M of $AgNO_3$, 0.1 M of ascorbic acid followed by 200 µL of seed solution with a total of 54.3 mL and the solution was kept the solution overnight at room temperature. After the completion of growth, the solution was kept in 4^{o}C for 1h and then kept at room temperature to settle down the excess of CTAB. After removing the settled particle, the supernatant was centrifuged at 1200 rpm for 20 minutes, and this was repeated thrice.

The GNR was subjected to a ligand exchange reaction with reduced glutathione in less than 4^{o}C. The centrifuged GNR was treated with 0.25 M reduced glutathione by simple stirring at 500 rpm for 3 hrs. The solution was kept in 4^{o}C for 1h and then kept at room temperature to settle down CTAB. After removing the settled particle, the supernatant was centrifuged at 1200 rpm for 20 minutes, and this was repeated thrice. The final product is abbreviated as GSH@GNR.

3.5.2. Preparation of photosensitizer/ cell targeting system (P@GNR/F@PGNR complex)

Protoporphyrin IX was treated with double the concentration of GSH@GNR through EDC/NHS coupling. Initially, 5mg/5µL of EDC was treated with protoporphyrin IX at pH 4 for 3h. Then 3mg/5µL of NHS was added and stirred for 15 minutes, and then GSH@GNR was added,and the pH was maintained above 9. Stirring was continued for 12h and then centrifuged at 14000 rpm. The product obtained was abbreviated as P@GNR.

P@GNR was again functionalized with folic acid through EDC/NHS coupling reaction. Initially, 5mg/5 µL of EDC was treated with P@GNR at pH 4 for 3hrs. Then 3mg/5 µL of NHS was added and stirred for 15 minutes and then added the folic acid, and the pH was maintained above 9. Stirring was continued for 12h

and then centrifuged at 14000 rpm. The product obtained was abbreviated as F@PGNR.

3.5.3. Characterisation

The GNR, GSH@GNR, P@GNR, and F@PGNR were initially characterized by Fourier transform infrared spectrometer to confirm the functionalisation and chemical changes after the functionalisation of GNR. Spectra were recorded in transmission mode using the KBr pellet method in the range from 400-4000 cm^{-1} over 32 scans. Zeta potential of each step was investigated using Malvern ZetasizerNano ZS 90 to investigate the change in charge with functionalisation. Surface morphology was confirmed using TEM (100kv JEM-2010 HiTachi-JEOL, Tokyo, Japan) analysis. UV-visible study was done using Shimadzu UV spectrometer- UV 2600. The emission property was studied using in Varian Carl Eclipse fluorescence spectrophotometer at different excitation wavelengths. The fluorescence imaging property of synthesized material was checked using IVIS Spectrum live animal imaging system. Fluorescence lifetime measurements were carried out using time-correlated single-photon counting (TCSPC) method with an excitation wavelength of 451 and 344 nm and using Fluoro Max-4C Spectrofluorometer (Horiba Instruments, USA) instrument.

3.5.4. *In vitro* cytotoxicity evaluation

L929 mouse fibroblast cells from ATCC were used for cytotoxic studies. Cells were seeded in 96 well plates at a density of 9000 cells per well and incubated for 12h. Thereafter the GNR, GSH@GNR, P@GNR and F@PGNR were diluted using cell cultured medium to obtain 1 mg/mL, 0.5 mg/mL, 0.1 mg/mL, 0.05 mg/mL, 0.01 mg/mL, 0.005 mg/mL and 0.001 mg/mL concentrations and incubated in cells for 72 h. Cells with media alone grown on the same plate was used as control. Then the material containing media was removed and replaced with 100 µL of fresh DMEM containing 3-(4, 5-dimethylthiazol-2-yl)-2, 5-diphenyltetrazolium bromide (MTT-10 µL, 5 mgmL−1). Following four h of the incubation period, the insoluble MTT formazan crystals formed were dissolved with DMSO (100 µL). Absorbance was measured at 570 nm using a microplate reader (Synergy H1 hybrid multi-mode microplate reader, Bio-Tek). The relative percentage cell viability for each system related to the control cells was finally calculated.

3.5.5. Cellular uptake of P@GNR and F@PGNR complex

The cellular internalization of P@GNR and F@PGNR was performed with a confocal microscopic investigation of cancer cells (MCF7). The cells were seeded on a cover glass with a density of 9000 cells/well. After three h of incubation of material, each material (1mg/mL) cells were washed with PBS and were stained with Dapi and mounted on a confocal glass plate, and fluorescence images were acquired.

3.5.6. *In vitro* photothermal treatment

MCF7 cells were used for the photothermal studies. MCF7 cells were seeded 96 well plates at a density of 9000 cells per well and incubated for 12 h. Thereafter the GNR, GSH@GNR, P@GNR and F@PGNR were diluted using cell cultured medium to obtain 1 mg/mL, 0.5 mg/mL, 0.1 mg/mL, 0.05 mg/mL, 0.01 mg/mL, 0.005 mg/mL and 0.001 mg/mL concentrations. The existing medium was replaced with 100µL of fresh medium containing the materials of different concentrations and incubated for the different time period. Cells with the same condition without material treatment were taken as a control group. Then 808 nm laser was irradiated for the 50s with a laser power of 0.05W. Then MTT assay was carried out.

Cells treated with 1mg/mL solution after laser irradiation live dead assay was done using ethidium bromide and acridine orange staining. The procedure followed: 100 µL of both the dyes were mixed and added 200 µL for each well kept it for 2 minutes, and then microscopic images were taken.

3.5.7. *In vitro* photodynamic treatment

MCF7 cells were used for the photothermal studies. MCF7 cells were seeded in each well of 96 well plates at a density of 9000 cells per well and incubated for 12 h. Thereafter the GNR, GSH@GNR, P@GNR and F@PGNR were diluted using cell cultured medium to obtain 1 mg/mL, 0.5 mg/mL, 0.1 mg/mL, 0.05 mg/mL, 0.01 mg/mL, 0.005 mg/mL and 0.001 mg/mL concentrations. The existing medium was replaced with 100µL of fresh medium containing materials of different concentrations and was incubated for the different time period. Cells having fresh media without material were used as control. Then 530 nm laser was irradiated for 40 s with a laser power of 0.05W, and then MTT assay was carried out.

For qualitative measurement of PDT, cells treated with 1mg/mL of material were irradiations with laser 530 nm followed by live dead assay were carried out. Ethidium bromide and acridine orange stain is used for live and dead cell imaging.

3.5.8. *In vivo* studies

The Institutional Animal Ethics Committee approved all animal studies; B-form number SCR/IAEC-149/MARCH/2015/87R. Swiss Albino mice of 20 g were used for the *in vivo* experiments. MCF7 cells were injected subcutaneously into the hind flank of each mouse. Animals were used for experiments, after two weeks of tumor induction.

For *in vivo* NIR fluorescence imaging, PDT and PTT, the animals were divided into 3 (1 control and 2 test) different groups having six animals each in a group. The first group of animals injected with PBS was used as control. The second group was injected with 0.5 mg/mL of P@GNR, and the third group was injected with 0.5 mg/mL of F@PGNR in 500 µL PBS. After half an hour, the animals were imaged using the IVIS animal imaging system. One among them,one from each group were sacrificed, and images were collected from excised organs. The rest of the animals from each group has undergone PDT/PTT treatment.

For PDT analysis, each animal (both control and test) was exposed to a 530 nm laser followed by fluorescence spectrum recording. The experiment was repeated at regular intervals of time till the 9^{th} day when the test animal's spectrum matched with control.

In the case of PTT, animals of both test and control were exposed with 808 nm laser. The fluorescence spectrum was recorded and repeated till the 6^{th} day when the symptoms of cancer disappeared in the fluorescence spectrum.

The tumor regression was monitored based onthechange in the concentration of total hemoglobin concentration and redox ratio. The total hemoglobin concentration was calculated from emission spectra at 410 nm excitation, which gives the spectral filtering modulation effect of hemoglobin. Hemoglobin concentration is one of the indicators of vascularization and is estimated from the equation

Total hemoglobin concentration (C_{Hb}) = FI_{500}/FI_{570}

Additionally, the redox ratio was also used for the evaluation of tumor regression. The metabolic activity can be monitored by the redox ratio (at 320 nm excitation). The ratio is calculated using the equation (Nair *et al.,* 2015b; Nazeer *et al.,* 2014a)

Redox ratio= FAD intensity/ (FAD intensity +NADH intensity)

3.6. Gold nanorod-gold cluster hybrid nanomaterial for cancer imaging and therapy

3.6.1. Materials

Chloroauric acid ($HAuCl_4$), cetyltrimethylammonium bromide (CTAB), reduced glutathione, mercapto succinic acid, and folic acid were purchased from Sigma Aldrich. Sodium borohydride, silver nitrate, ascorbic acid, and sodium hydroxide were purchased from Merck. All cell culture media (DMEM) and reagents (MTT, acridine orange, ethidium bromide, Dapi, FBS, and antibiotic-antimycotic solution) were purchased from HiMedia.

3.6.2. Synthesis of gold cluster-gold nanorod hybrid nanomaterial (GQC@GNR)

Gold nanorods were synthesised as mentioned in the previous section (3.4.2). GQC was synthesised in two-step method. At first, gold nanoparticles were synthesised using mercaptosuccinic acid and chloroauric acid. Then GQC was synthesized by etching of gold nanoparticles with reduced glutathione (GSH). For the synthesis of NIR emitting gold nano cluster, mercaptosuccinic acid conjugated gold nanoparticles (GMSA) was treated with GSH at 0^oC. In a typical experiment, 2.8 mg GMSA at pH 1.5 and 12 mg GSH (at 0^oC) was dissolved in 30 mL MQ water. After 15 min, this system was allowed to react at 70^oC at 500 rpm for 24 h. As time progressed, the color of the solution changed from brown to yellow. The gold cluster (GQC) was collected by centrifugation at 3000 rpm for 10 minutes to remove any GMSA. The supernatant was collected and precipitated in 1:1 methanol isopropanol mixture to remove the unreacted GSH from the cluster.

GNR and GQC were mixed by different pH conditions (neutral GQC, acidic GQC, and basic GQC to neutral GNR, or neutral GQC is added to neutral GNR, acidic

GNR or basic GNR). The mixtures were stirred for 3 h. Purification was done by centrifugation, and excess GQC was removed by methanol wash.

3.6.3. Characterisation

The UV-visible study was done using Shimadzu UV spectrometer- UV 2600. The emission property was studied using in Varian Carl Eclipse fluorescence spectrophotometer at different excitation wavelengths. The fluorescence imaging property of synthesized material was checked using IVIS Spectrum live animal imaging system. Fluorescence quantum yield calculations were done using the standard method from emission spectra. Zeta potential of each step was investigated using Malvern Zetasizer Nano ZS 90 to investigate the change in surface charge before and after functionalization. Surface morphology was confirmed using TEM (100kv JEM-2010 HiTachi-JEOL, Tokyo, Japan) analysis.

3.6.4. *In vitro* cytotoxicity evaluation

L929 mouse fibroblast cells from ATCC were used for cytotoxic studies. Cells were seeded in 96 well plates at a density of 9000 cells per well and incubated for 12h. After that the GQC@GNR was diluted using cell cultured and incubated in cells for 24 h. Cells with media alone grown on the same plate was used as control. Then the material containing media was removed and replaced with 100 µL of fresh DMEM containing 3-(4, 5-dimethylthiazol-2-yl)-2, 5-diphenyltetrazolium bromide (MTT-10 µl, 5 mg/mL). Following 4 h of the incubation period, the insoluble MTT formazan crystals formed were dissolved with DMSO (100 µL). Absorbance at 570 nm was measured using a microplate reader (Synergy H1 hybrid multi-mode microplate reader, Bio-Tek). The relative percentage cell viability for each system related to the control cells was finally calculated.

3.6.5. Cellular uptake of GQC@GNR

The cellular internalization of folic acid conjugated GQC@GNR was performed with an Olympus microscope in HeLa cells. The cells were seeded on a cover glass with a density of 9000 cells/well. After 3 h of incubation of material, each material (0.1 mg/mL) cells was washed with PBS mounted on a confocal glass plate, and the fluorescence images were acquired.

3.6.6. *In vitro* photothermal treatment

HeLa cells were used for the photothermal studies. HeLa cells were seeded in 96 well plates at a density of 9000 cells per well and incubated for 12 h. There after the folic acid conjugated GQC@GNR were diluted using cell cultured medium to obtain 0.5 mg/mL, 0.4 mg/mL, 0.31 mg/mL, 0.3 mg/mL, 0.2 mg/mL, 0.1 mg/mL, 0.05 mg/mL and 0.025 mg/mL concentrations. The existing medium was replaced with 100µl of fresh medium containing the materials of different concentrations and incubated for three h. Cells with the same condition without material treatment were taken as the control group. Then 808 nm laser was irradiated for the 60s with a laser power of 0.05W. Then MTT assay was carried out.

Cells treated with 0.5 mg/mL solution after laser irradiation live dead assay was carried out using ethidium bromide and acridine orange staining. The procedure followed was 100 µL of both the dyes were mixed and added 200 µL for each well kept it for 2 minutes. Then microscopic images were taken.

3.6.7. *In vivo* studies

All animal studies were approved by the Institutional Animal Ethics Committee (B form number SCT//IAEC-082/OCTOBER/2013/82)

Swiss Albino mice of 30 g were used for the *in vivo* experiments. Dalton lymphoma cells were injected subcutaneously into the hind flank of each mouse. After 5 days of tumor induction, animals were used for experiments.

The first group of animals were injected with PBS, was used as control. The second group injected with 0.5 mg/mL of GQC@GNR in 500 µL PBS. After half an hour, the animals were imaged using the IVIS animal imaging system. One among each group were sacrificed, and images were collected from excised organs and biodistribution were monitored.

Chapter 4

Results

This chapter confers the results obtained by following the methodologies discussed in chapter 3.

4.1. Quantum dot based multianalyte detection

Quantum dots are considered to bean ideal candidate for sensing, due to its exceptional fluorescence properties. In the present thesis, two cadmium selenide quantum dots with two different capping agents and fluorescent properties are utilized for the detection of multianalyte. The quantum dotused for the sensing applications are cysteine and glutathione capped cadmium selenide quantum dots (Qd and GQd) having green and red emission, respectively. Qd was designed for the simultaneous detection of copper and creatinine. Sulfamethoxazole functionalized GQd was used for the detection of lead and zinc.

4.1.1. Cadmium selenide quantum dots for simultaneous detection of copper and creatinine

Cadmium selenidequantum dots with cysteine (amino acid) as a capping agent were synthesised (Qd) and used for the sensing of copper and creatinine.

4.1.1.1. Synthesis of quantum dot based sensor (PAQd) and its characterisation

Cysteine quantum dots (Qds) were synthesised and functionalised with picric acid through EDC, as explained in 3.1.1.The UV-visible spectrum of Qd showed a broad shoulder peak at 515 nm (Figure 11). The spectrum of PAQd showed a strong absorption peak at 354 nm and a broad shoulder peak at 502 nm. The presence of these peaks confirmed the functionalisation of picric acid over Qd, because picric acid has a characteristic absorption peak at 356 nm. Transmission electron micrograph of Qd showed well dispersed particles (Figure 11b), whereas that of PAQd (Figure 11c) showed an organic layer of picric acid over it.

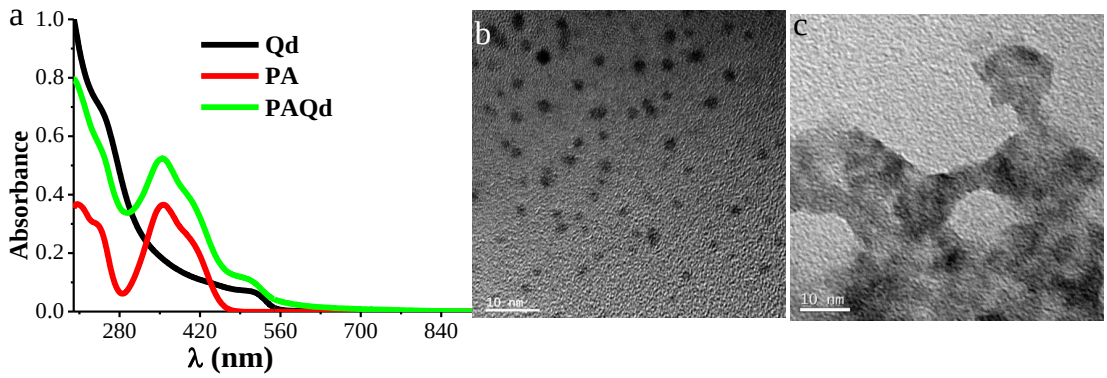

Figure 11: a) UV-visible spectra of Qd, PA and PAQd b) Transmission electron micrographs of Qd and c) PAQd.

Again, the emission properties of the samples were evaluated with a fluorescence spectrometer. Qd showed an emissionpeak at 540 nmwhen excited at 390 nm (Figure 12a). Upon conjugation with picric acid (PA), this peak is blue-shifted to 515 nm. The conjugated PAQdshowed an additional emission peak at 446 nm on excitation with 290 nm, which was absent in the case of Qd (Figure 12b). Fluorescence lifetime decay spectral values of both the emissions were evaluated and found to be 4 and 5ns (Figure 12c & d).

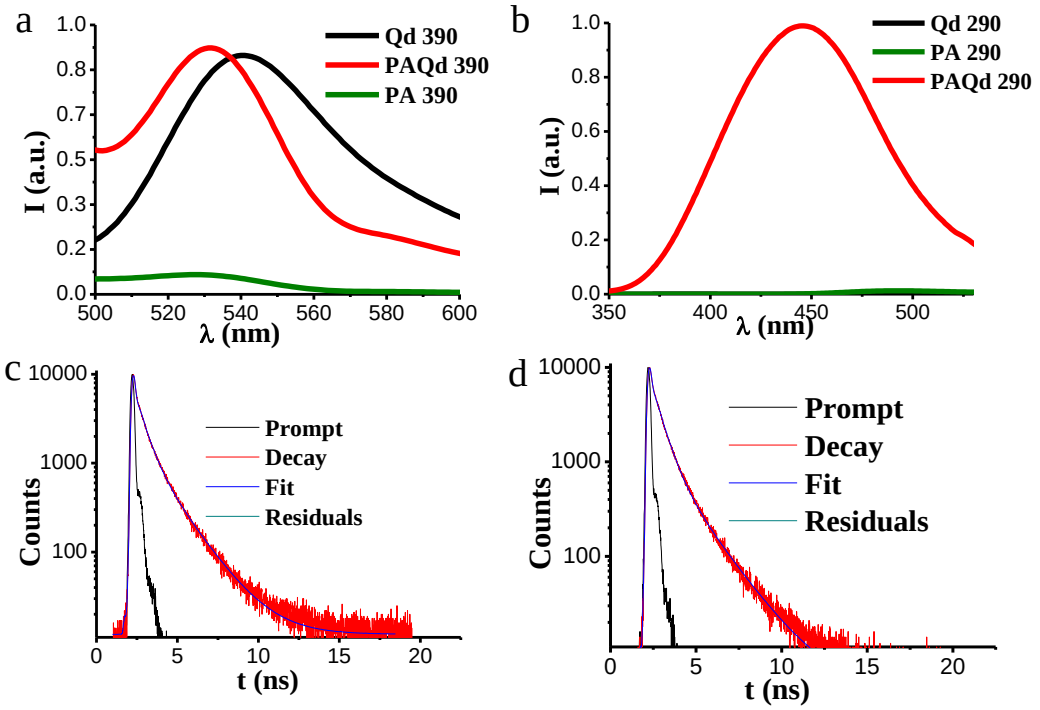

Figure 12: Emission spectra of Qd, PA, and PAQd a) λ_{ex} 390 nm and b) λ_{ex} 290 nm c) Fluorescence lifetime decay spectrum of Qd at 515 nm emission and d) fluorescence lifetime decay spectrum of PAQd at 446 nm emission.

The functionalisation was again confirmed using FT-IR spectroscopy (Figure 13). In the FT-IR spectrum of Qd, the absence of –SH peak at 2557 cm^{-1}confirms the formation of S-M (sulphur-metal) bond. The broad peak at 3425 cm^{-1} indicates the presence of intermolecular hydrogen bonding. Shoulder peak at 1623 cm^{-1} indicates the presence of the carbonyl group of cysteine. Qd on functionalisation with EDC followed by PA, the hydroxyl (OH) peak of PA at 3428 cm^{-1} disappears indicated the participation of –OH group. Peaks around 3000 cm^{-1} and 600-900 cm^{-1} confirmed the presence of an aromatic ring, and the peak at 1334 cm^{-1} confirms the nitro group.

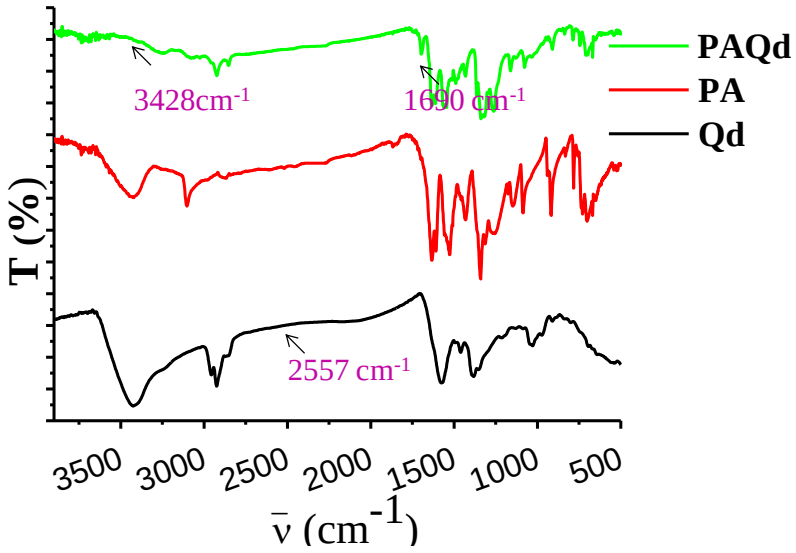

Figure 13: FT-IR Spectra of Qd, PA, and PAQd.

Nuclear magnetic resonance (NMR) spectra of Qd and PAQd (Figure 14) again confirm the successful functionalisation of picric acid over Qd. NMR spectra of Qd show the peaks corresponding to NH, CH, and CH_2at 1.81 ppm (1H,s,J-33.6 Hz) 3.64 ppm(1H, s, J-30) and 3.42- 3.52 ppm (2H, m, J-15) respectively. Whereas in the NMR spectrum of PAQd, no acidic hydrogen is observed, indicating that the phenolic -OH is participating in the reaction. And the presence of aromatic ring in the 8.860 ppm and 8.360 ppm confirms the presence of picric acid in PAQd. All other characteristic peaks of NH, CH, and CH_2 were observed with minor chemical shifts due to the functionalisation of picric acid on Qd.

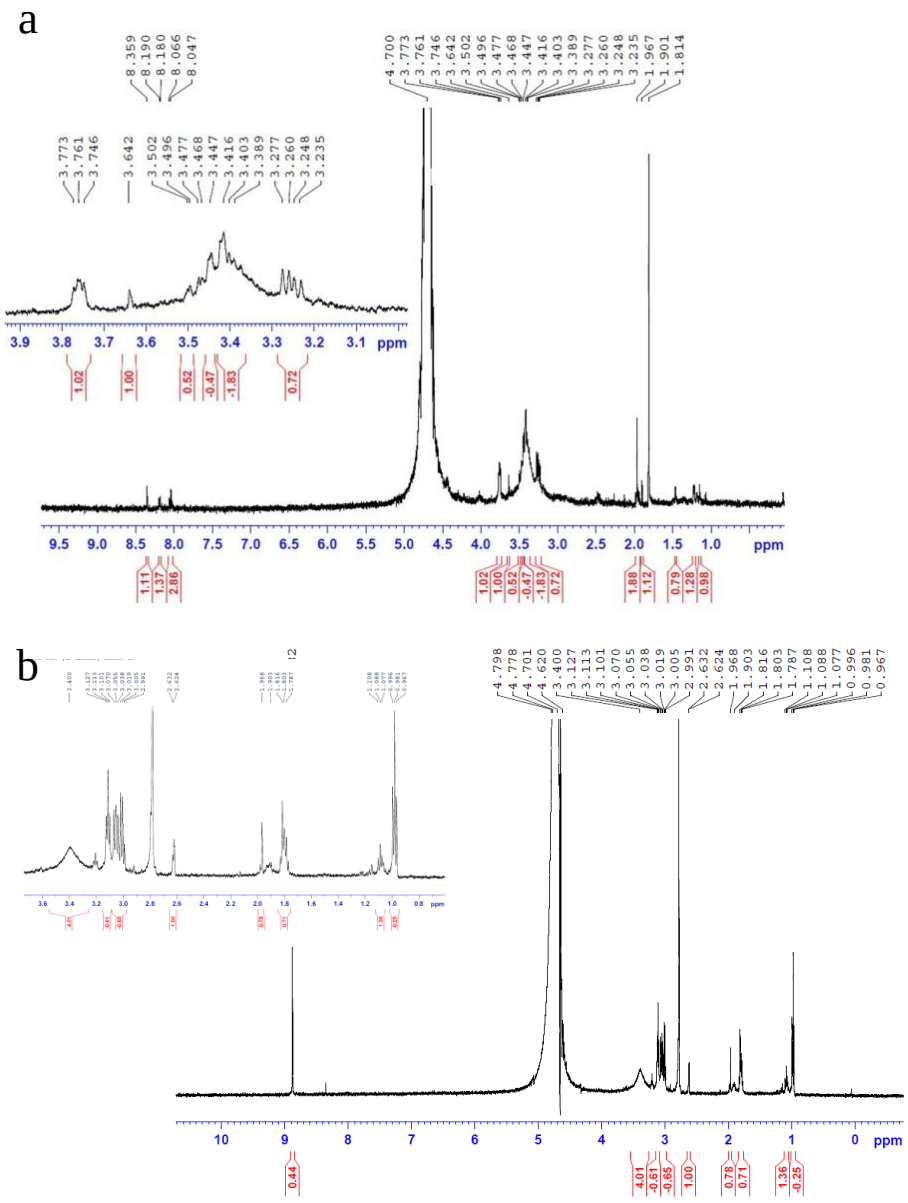

Figure 14: NMR spectra of a)Qd and b)PAQd.

The surface charges of samples were tested using zeta potential analysis. It was observed that Qd showed zeta potential value of-16.7 mV and that of PAQd,it was -14.9 mV. The change in zeta potential suggests the functionalisation, and the PAQd value indicates the stability of the systems (Figure 15).

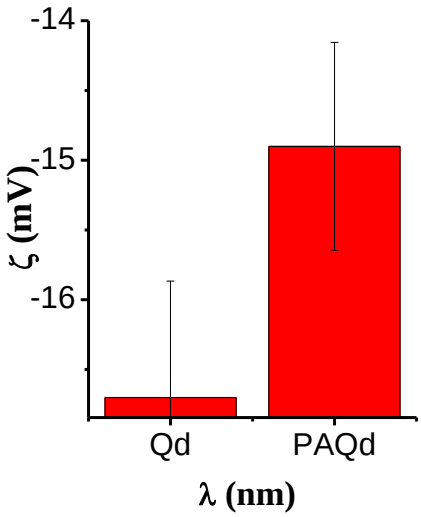

Figure 15: Zeta potential of Qd and PAQd.

4.1.1.2. Sensing of bioanalytes (copper and creatinine) using PAQd

Copper and creatinine were detected optically using the change in fluorescence property of PAQd. Upon the addition of creatinine to 1 mg/mL of the sensor, the fluorescence intensity at 446 nm showed a concentration-dependent increase of creatinine (Figure 16a). Meanwhile, the addition of copper to the sensorcauses concentration-dependent fluorescence quenching at 531 nm (Figure 16b).

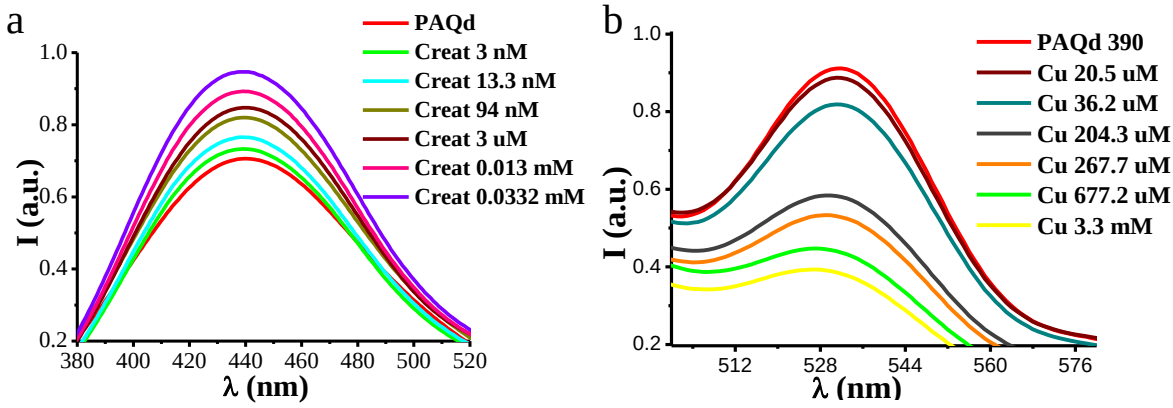

Figure 16: Emission spectra of PAQd (a. λ_{ex} 290 nm and b. λ_{ex} 390 nm) a) fluorescence enhancement on the addition of higher concentration of creatinine and b) fluorescence quenching on the addition of different concentration of copper.

The sensing property of PAQd was also evaluated in blood serum. Serum, separated from human blood, was diluted with saline and incubated with different

concentrations of creatinine and 0.01 mg/mL of PAQd. The enhancement of the fluorescence emission at 446 nm,with an increase in the concentration of creatinine (Figure 17a), was noted.

Another batch of serum was incubated with different concentrations of copper and added 0.01 mg/mL of PAQd. Here, fluorescence intensity at 531 nm decrease as the concentration of creatinine increases (Figure 17b).

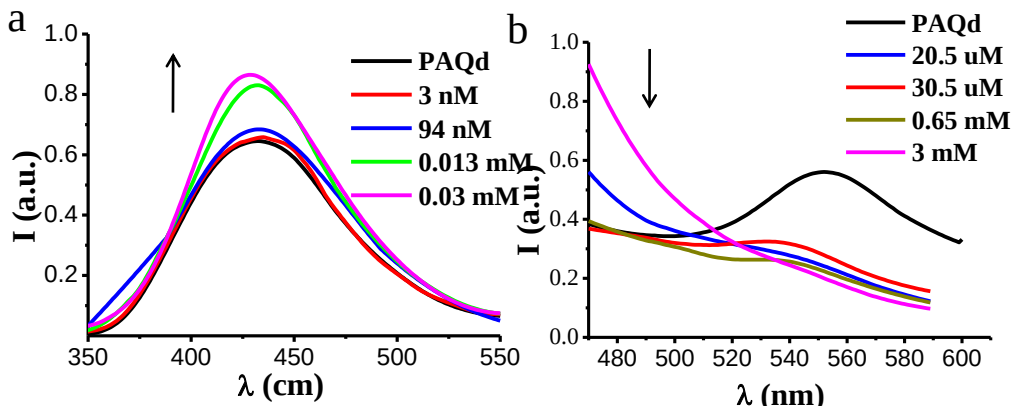

Figure 17: a) Detection of creatinine in blood serum using PAQd [Black-:PAQd, red to pink- increase in creatinine concentration; arrow indicate the increase in fluorescence intensity] b) detection of copper in blood serum using PAQd [black:-PAQd, red to pink -increase in copper concentration; arrow indicate the decrease in fluorescence intensity].

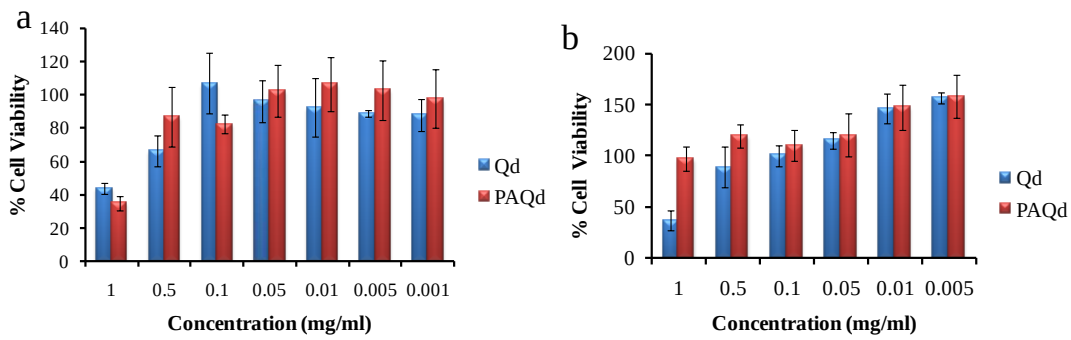

Figure 18: MTT assay of Qd and PAQd in a) L929 cells and b) MDA-MB-231 cells.

Before checking the feasibility of these materials to detect copper and creatinine in the cellular environment, their cytotoxicity evaluation is essential. MTT assay of Qd and PAQd using L929 and MDAMB-231 cells showed that concentration of the order of 0.01 mg/mLof both Qd and PAQd has more than 80% cell viability(Figure 18).

Because analytes of interest could be present both inside and outside the cells, the extracellular and intracellular sensing efficacy of the sensor was checked. For intracellular creatinine sensing, cells were incubated with creatinine for 30 minutes and washed with PBS followed byincubating with PAQd for 3h. Intracellular Cu was also evaluated with the same procedure. Both the cell lines, fluorescence quenching as the concentration of Cu increases and enhancement as creatinine concentration increases were observed. For extracellular creatinine sensing, sensor PAQd was incubated with the cells initially for 3 h followed creatinine for 3 minutes. The same procedure was used for extracellular sensing of copper as well. Fluorescence enhancement was observed with creatinine for L929 cells, whereas MDAMB 231 did not show any significant change. Observations were similar in the case of Cu, where the fluorescence decrease was evident in L929 cells, but not so with MDAMB 231 cells(Figure 19& Figure 20).

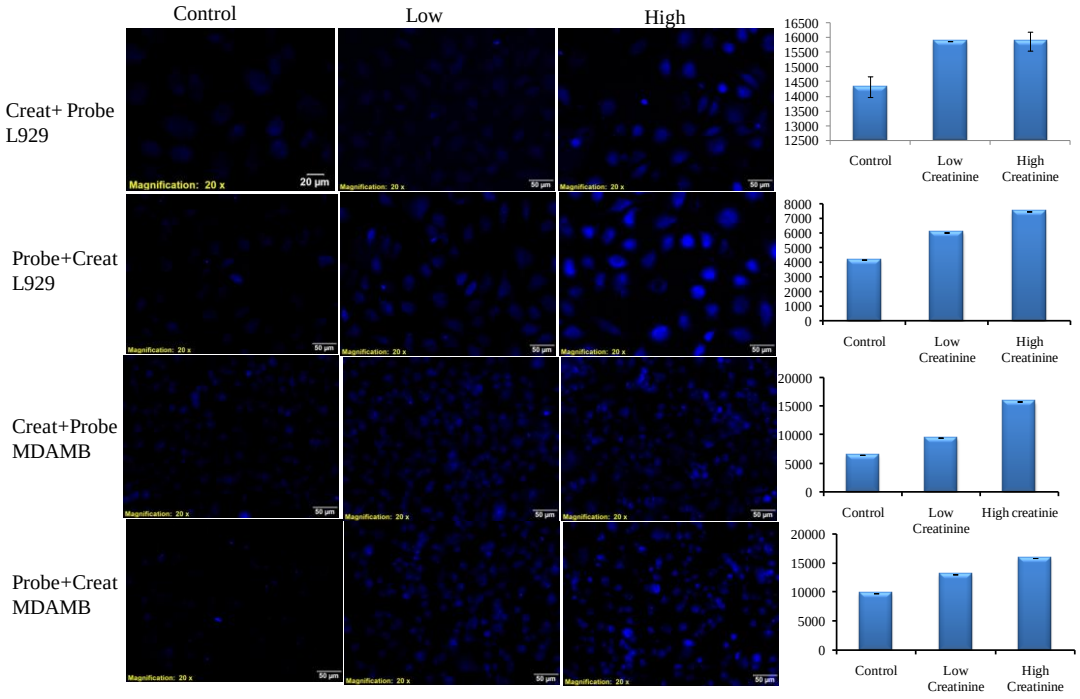

Figure 19: Detection of creatinine; as creatinine concentration increases, fluorescence intensity also increases considerably in L929 cells. Fewer enhancements in the case of MDA-MB- 231 cells are visible.

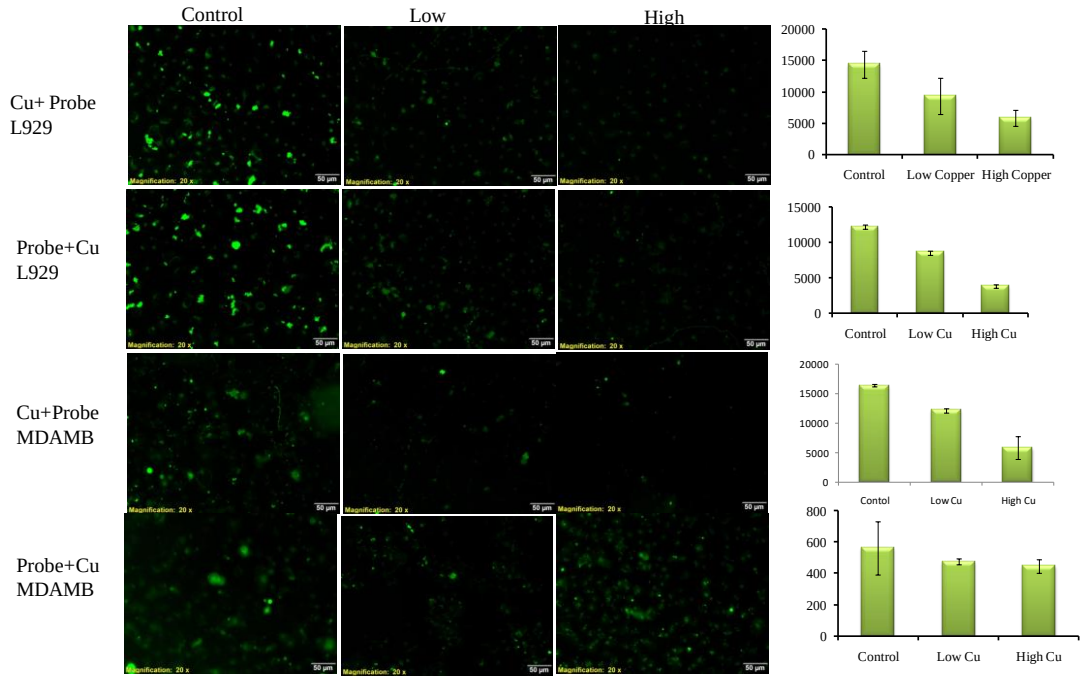

Figure 20: Detection of copper; as concentration increases, fluorescence intensity decreases considerably in L929 cells. Intensity decrease is not prominent in the case of MDA-MB- 231 cells.

4.1.1.3. Selectivity for sensing of copper and creatinine from aqueous solution

The interference of various molecules such as manganese (Mn), lead(Pb),potassium (K), urea, uric acid, glucose, magnesium (Mg), calcium (Ca),sodium(Na), cholesterol, etc. was tested while sensing the presence of creatinine and copperusing PAQd. For this, 1 mg/mL of the above molecules in aqueous solution were added to 0.01 mg/mL of PAQd, separately. Emission peaks at 446 nm and 531 nm were recorded and plotted separately (Figure 21).

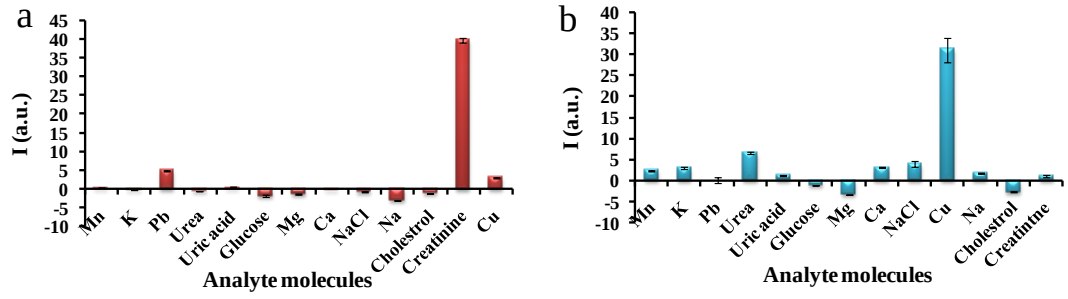

Figure 21: a) Selectivity of creatinine at 446 nm emission b) Selectivity of copper at 531 nm emission.

None of the above analytes have significantinterferenceon the fluorescence signal, and hence PAQdwas found to be highly selective for the detection of creatinine and copper.

4.1.1.4. Simultaneous detection of Cu and creatinine (non-interference with each other)

To see whether the analytes of the study, vizcopper, and creatinine interfere with each other, the zeta potential of the sensor, PAQd, along with different concentrations of the analytes,was studied. It wasfound that as the concentration of copper and creatinine increases, zeta potential value decreases. In the case of creatinine, the difference in the zeta potential was very less. Still, in the case of copper, the decrease is very drastic and approaches zero, but never attained zero even for very high concentrations. When creatinine was added to the copper rich solution of PAQd, the zeta potential value increases (Figure 22a).Transmission electron micrograph (TEM)images were taken for explaining its mechanism. The TEM images of creatinine incubated probe showed well-dispersed particles (Figure 22b), where an increase in fluorescence was observed. In contrast, the copper incubated system showed an aggregationin TEM images, where the fluorescence quenching was observed (Figure 22c).

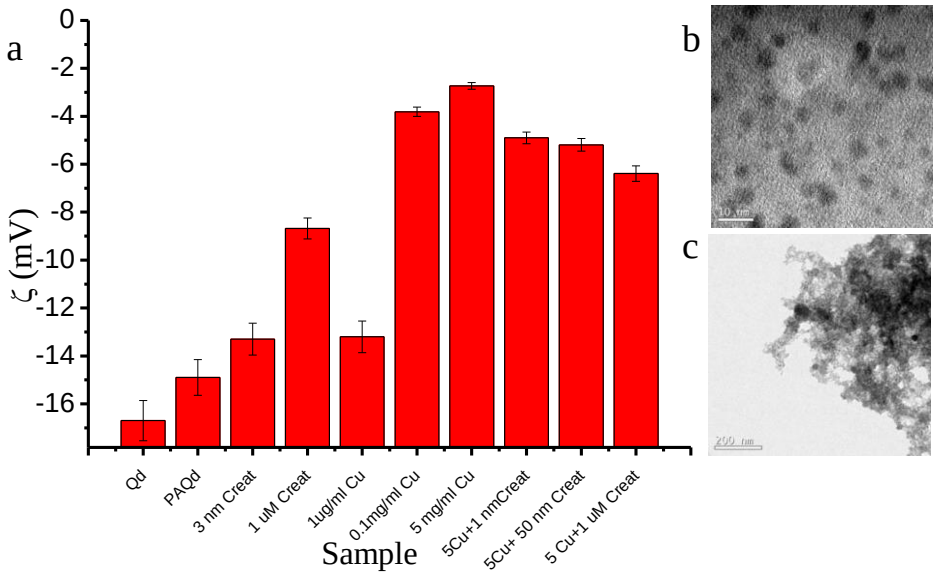

Figure 22: a) Zeta potential of Qd, PAQd, and different concentrations of copper and creatinine, TEM image-b) PAQd after creatinine incubation, and c) copper incubated PAQd.

4.1.2. Cadmium selenide quantum dots for the detection of lead and zinc

Cadmium selenide nanoparticles capped with glutathione was used for the detection of metals- lead and zinc. Glutathione capped quantum dot was used for the detection of lead.It was further functionalised with sulfamethoxazole(antibiotic) for zinc sensing.

4.1.2.1. Synthesis of glutathione capped cadmium selenide quantum dots (GQd) and its characterisation

GQd was prepared by treating cadmium chloride and selenium stock using glutathione as a capping agent (3.2.1). GQd prepared was characterised using different techniques such as UV, fluorescence, and FTIR spectroscopies. UV visible spectrum of GQdwas shown in figure23a;shows a characteristic absorption peak at 435nm. The TEM image of GQd showed a well-dispersed particle with a size of ~6±1 nm (Figure 23b).

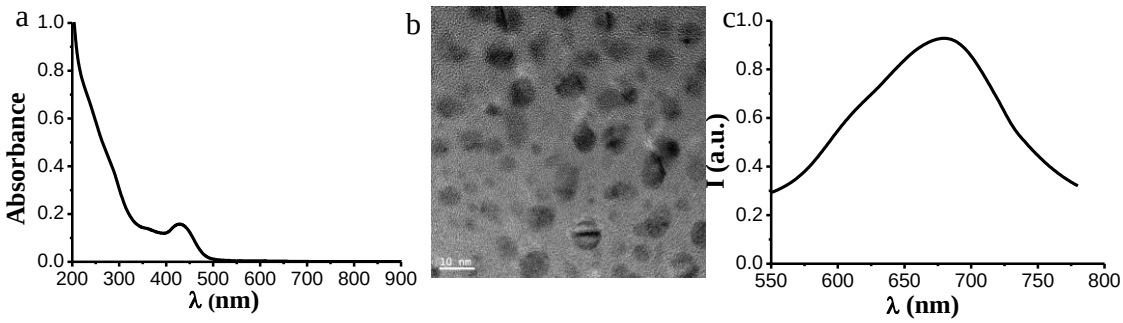

Figure 23: a) Absorbance spectrum of GQd, b) TEM images of GQd and c) emission (λ_{ex} 420 nm) spectrum of GQd.

GQd shows an emission maximum at 680 nmfor an excitation wavelength of 420 nm (Figure 23c). The formation ofGQdwas confirmed by FT-IR spectroscopy (Figure 24); the absence of the S-H peak of glutathione at 2509 cm^{-1} in the spectrum of GQd indicates thatthe same was formed through S-M (metal) bond. Also, the absence of carboxylic bands in GQd suggests the participation of the same in the formation of GQd.

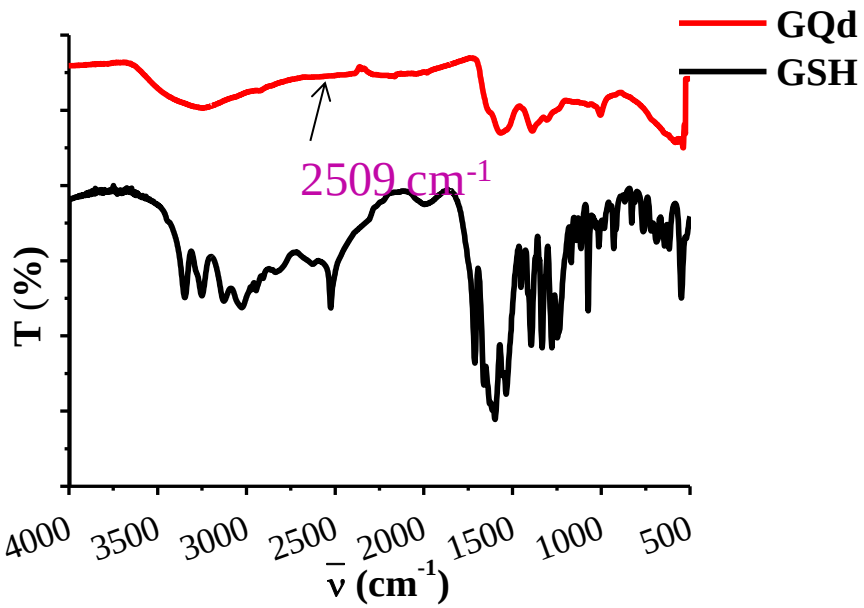

Figure 24: FT-IR Spectra of GSH and GQd.

4.1.2.2.Detection of lead ion

Different concentrations of lead ion (picomolar to millimolar) were incubated 30s with 1 mg/mL of GQd. Fluorescence intensity at 680 nm was noted, and a concentration depended quenching was observed(Figure 25), indicating GQds use as an excellent sensor for the lead ions.

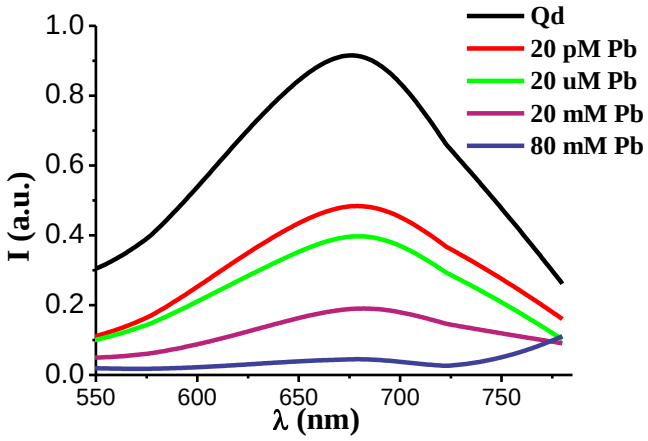

Figure 25: Decrease in fluorescence intensity as the concentration of lead increases.

4.1.2.3.The selectivity of lead ion

Different analytessuch as dopamine, cysteine, zinc, copper, sodium borohydride, hydrogen peroxide, and ascorbic acid (all 1mM concentration)were incubated in 1mg/mL of GQdsolution. Emission at 680 nm was noted for every sample; no significant changes were observed (Figure 26) except lead, proving GQd selectivity towards lead ion.

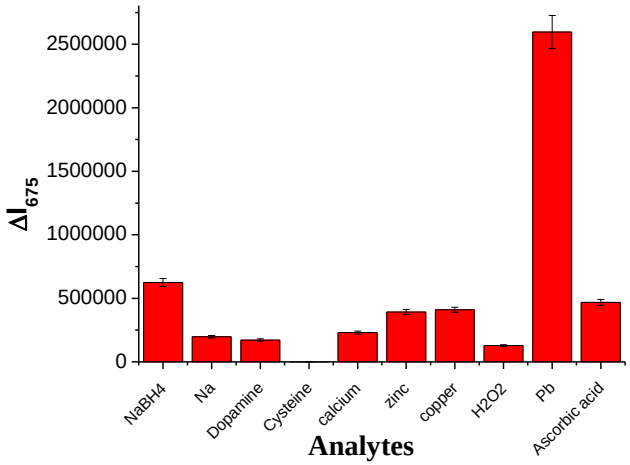

Figure 26: Selectivity of GQd on lead over other analytes.

4.1.2.4. Size and zeta potential analysis

Zeta potential of GQd and different concentrations of lead incubated GQd was noted. It was found that as the concentration of lead increases, zeta potential value decreases (Figure 27a). But the size of the sample increased with increasing concentration of the lead ion.

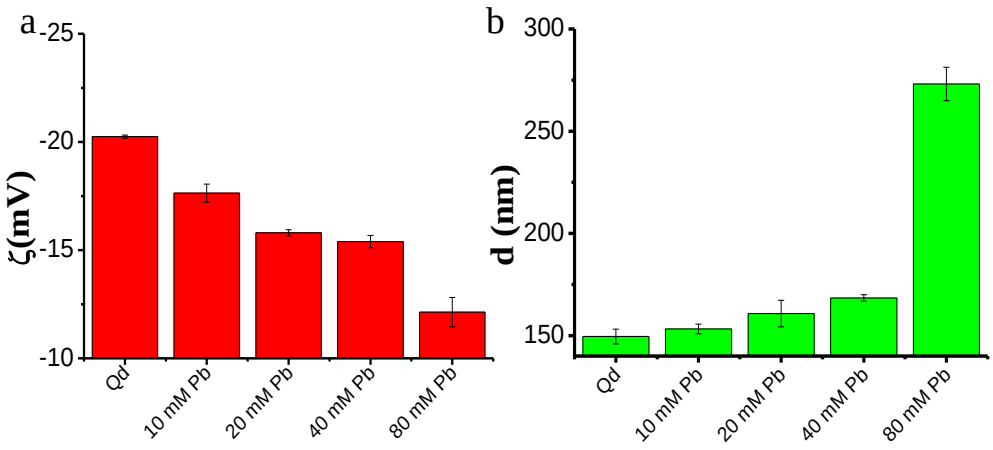

Figure 27: a) Zeta potential of GQd and different concentrations of lead incubated GQd, and b) Size analysis of Qd and different concentrations of lead incubated GQd.

4.1.2.5.Functionalisation of GQd with sulfamethoxazole and its characterisation

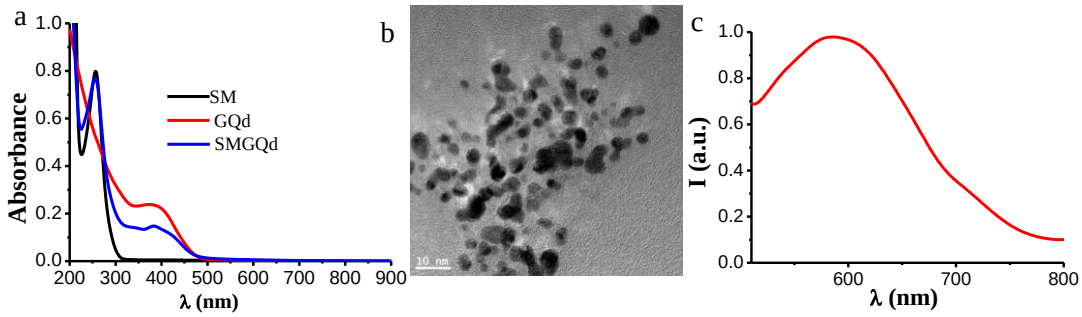

Figure 28: a) UV-Visible absorption spectrum of sulfamethoxazole (SM), GQd, and SMGQd and b) TEM image of SMGQd c) Emission spectrum of SMGQd (λex=420 nm).

GQd was functionalised with sulfamethoxazole for designing the zinc sensor, SMGQd. As an initial attempt to study the optical property, its UV-visible spectrum was recorded (Figure 28a), which shows a peak at 396 nm corresponding to that of GQd. A peak at250 nm was observed forsulfamethoxazole and the presence of the same in SMGQd confirms its conjugation. SMGQd shows emission at 586 nm, for 420 nm excitation (Figure 28c).

FT-IR spectra confirmed the functionalisation of sulfamethoxazole over GQd. The peak at 1458 cm^{-1} indicates the presence of an amide group, and peakat 1121 cm^{-1}shows S=O peak of sulfamethoxazole (Figure 29) in SMGQd.

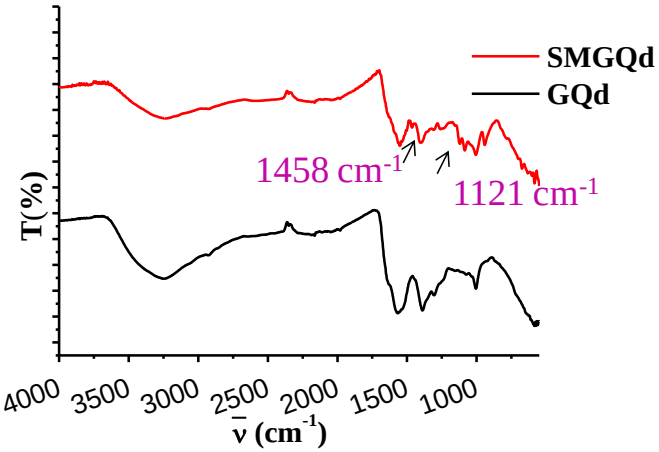

Figure 29: FT-IR spectra of GQd and SMGQd.

4.1.2.6.Detection of zinc from aqueous medium

Different concentrations (nM to mM) of zinc were added to solution containing1 mg/mL of SMGQd for 2 minutes. Fluorescence intensity was recorded at 420 nm excitation. A concentration-dependent enhancement in the fluorescence intensity at 586nm was observed (Figure 30).

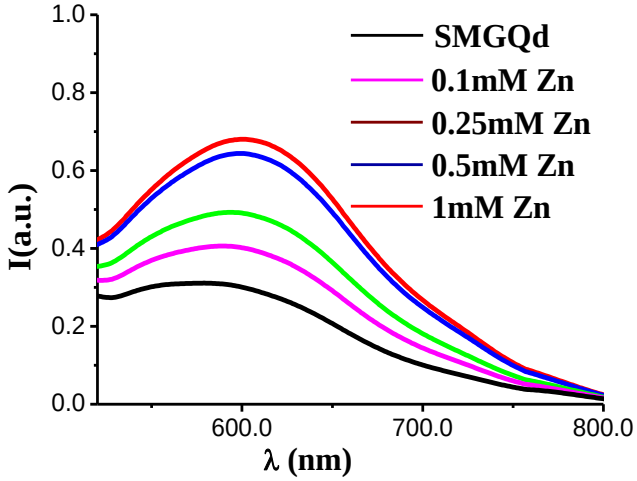

Figure 30: Fluorescence emission spectra of SMGQ, fliuorescence intensity enhances as the concentration of zinc increases.

4.1.2.7.Selectivity of zinc over other analytes

The selectivity of SMGQd for sensing of zinc was ascertained in the presence of different analytes such as calcium, iron, manganese, magnesium, lead, and cadmium. 1mM of analytes added to 1 mg/mL of SMGQd, and themajority of the analytes didn't show any significant change in fluorescence intensity at 586 nm

emission. However, lead and cadmium showed a variation in the fluorescence intensity, but was less prominent compared to zinc(Figure 31).

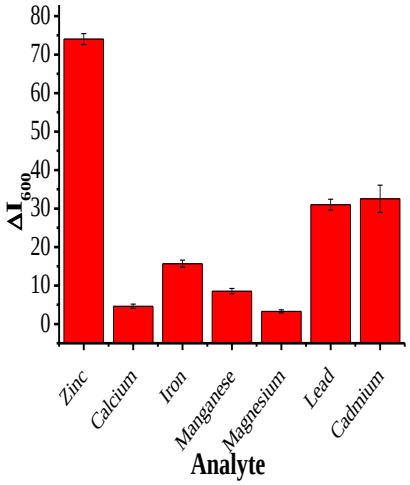

Figure 31: Selectivity of zinc over other analytes.

4.1.2.8.Size and zeta potential analysis

The results of size and zeta potential analysis are shown in Figure 32a& b. As concentration of zinc increases its zeta potential value and size are found to decrease (Figures32a&32b).

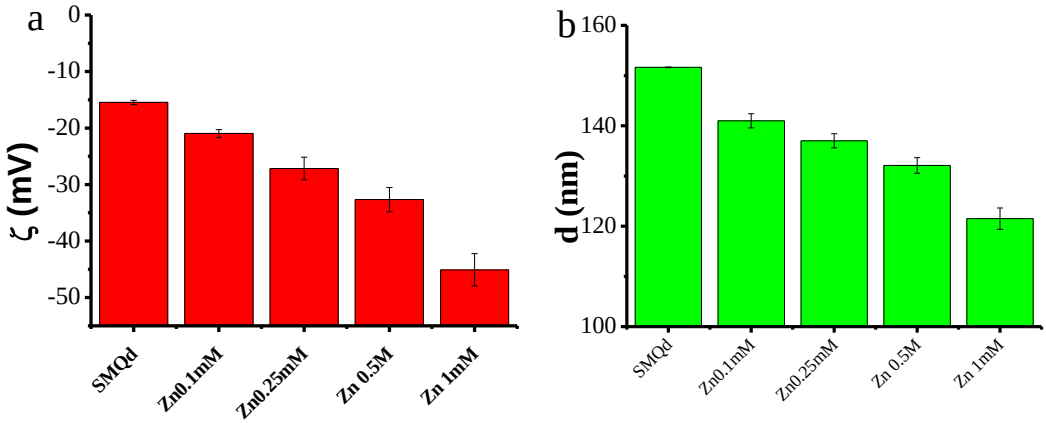

Figure 32: a) Zeta potential of SMGQd and different concentration of zinc incubated SMGQd b) Size of SMGQd and different concentrations of zinc added SMGQd.

4.2. Cysteine gold cluster for the detection of dopamine and cellular imaging

Cysteine is a water-soluble amino acid, and it is used for the synthesis of different nanoparticles. Here,it is used as a capping agent for the synthesis of gold cluster.

4.2.1. Synthesis and characterisation of cysteine cluster (AuC)

Chloroauric acid and cysteine were used to prepare gold cluster (3.3.2). Sodium borohydride asthe reducing agent andsodium hydroxide provided thebasic medium for the reaction mixture.Different batches of synthesis were carried out for optimizing the synthesis of the gold cluster. Different concentrations of chloroauric acid, cysteine, sodium borohydride, and sodium hydroxide weretried. Also, the synthesis was optimized by changing the pH of the solution.

As gold clusters have characteristic UV-visible absorption spectra, we utilized this parameter for optimizing the synthesis protocol to get the most suitable cluster for the use. UV-visible absorption spectraof the samples from different batches are shown in Figure 33 a-e.

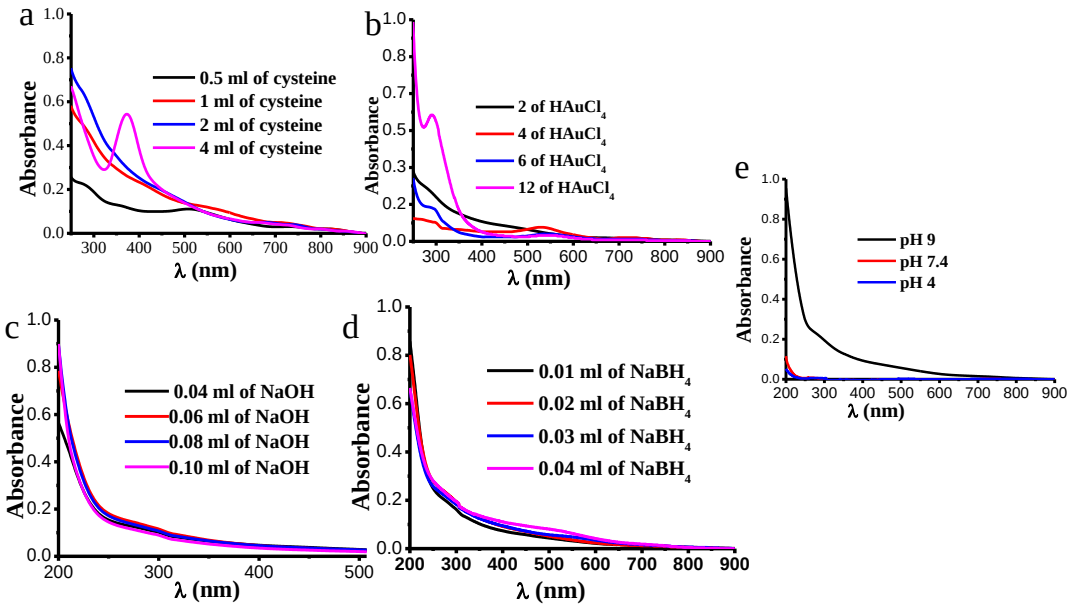

Figure 33: UV-visible absorption spectra of gold cluster synthesized with different concentrations of a) cysteine b) $HAuCl_4$ c) NaOH and d) $NaBH_4$ e) cluster synthesized at different pH.

Change in concentrations of cysteine and $HAuCl_4$ in the reaction mixture resulted in UV-visible absorption spectra similar tosystems that have different shape compared with typical gold cluster spectra. With change in concentrations of sodium borohydride and sodium hydroxide, the spectra indicated different sized clusters (Figure 33 c & d). On changing the pH of the reaction mixture, acidic and neutral pH do not show any cluster formation. But in the case of the basic pH cluster, the formation was observed (Figure 33 e) as seen by the characteristic UV- visible absorption spectra of clusters.

From the above clusters, the most suitable one, which showed the characteristic absorption spectra, was chosen. Figure 34a shows the absorption spectrum of optimized gold cluster. The optimized cluster(AuC)was synthesized with 1 mL of 1 mM cysteine& 2 mL of 2.5 mM $HAuCl_4$at basic pH. It showed emission at 606 nm for 400 nm excitation (Figure 34 b).

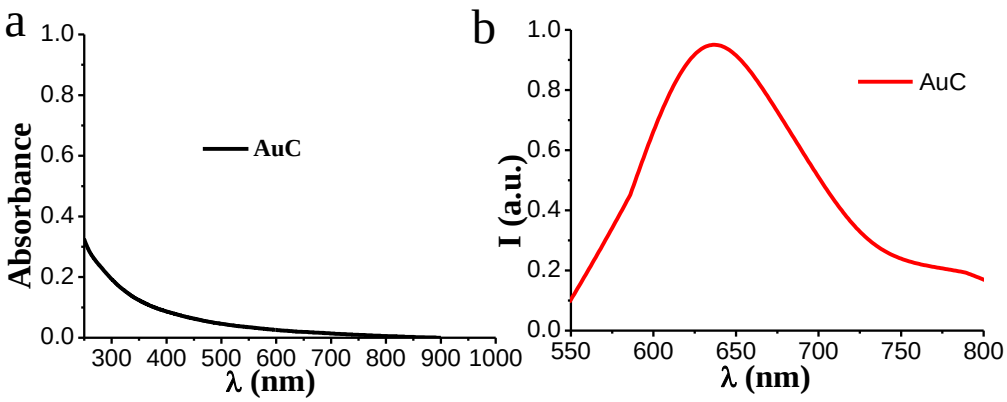

Figure 34:a) Absorption and b)emission spectra of AuC.

FT-IR spectra of cysteine and AuC were recorded to confirm the formation of AuC. It was found that carboxylic peaks were absent in AuC spectrum (Figure 35). The peak at 1629 cm^{-1} indicates the presence of an amine group in the AuC, suggesting that cysteine act as a chelating molecule for AuC.

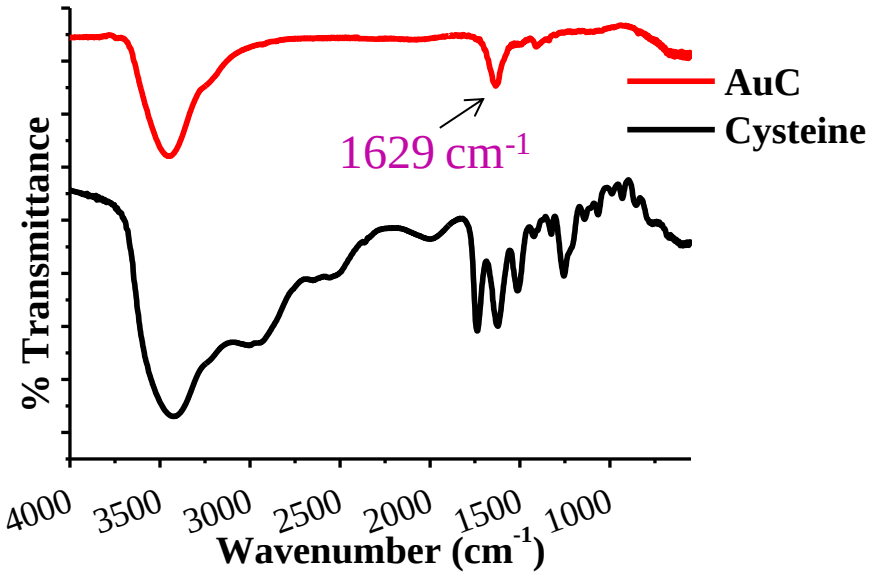

Figure35: FT-IR spectra of AuC and cysteine.

Transmission electron micrographic images showedAuCwith a size of less than 1.7nm(Figure 36b).MALDI-MS shows complete fragmentation (Figure 36a)of the gold cluster.

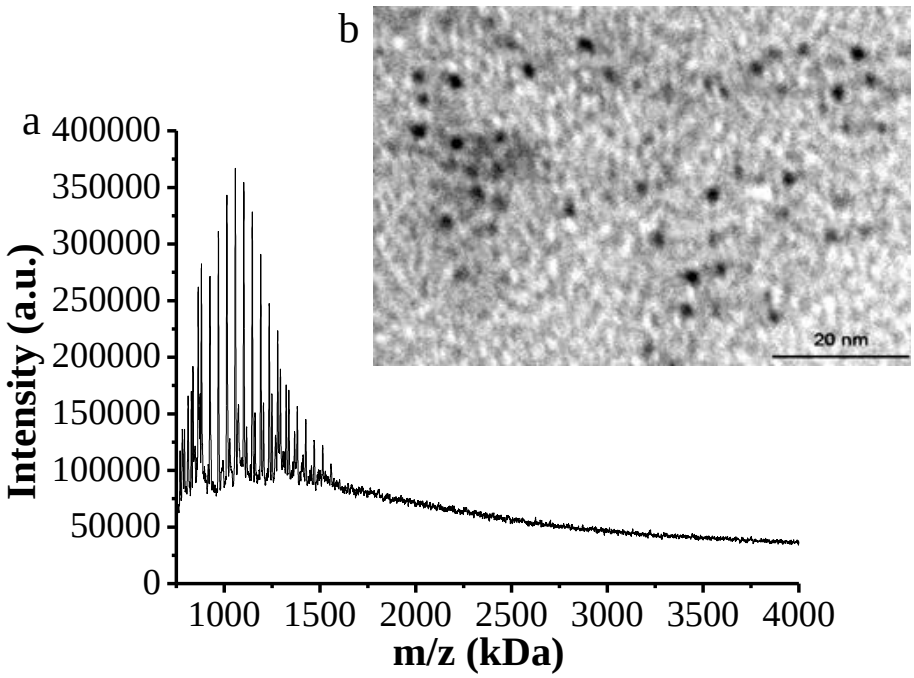

Figure 36:a) MALDI-MS of AuC and b) TEM image of AuC.

4.2.2. Sensing of dopamine using cysteine gold cluster

Cysteine stabilized gold cluster was used for the sensing of dopamine by spikingdifferent concentrations of dopamine to the sensor solution. A concentration-based increase in fluorescence was observed for the peak at 606 nm (Figure 37a).The selectivity of AuC was checked for dopamine over other biologically relevant molecules such as urea, uric acid, sodium borohydride, ascorbic acid, etc.

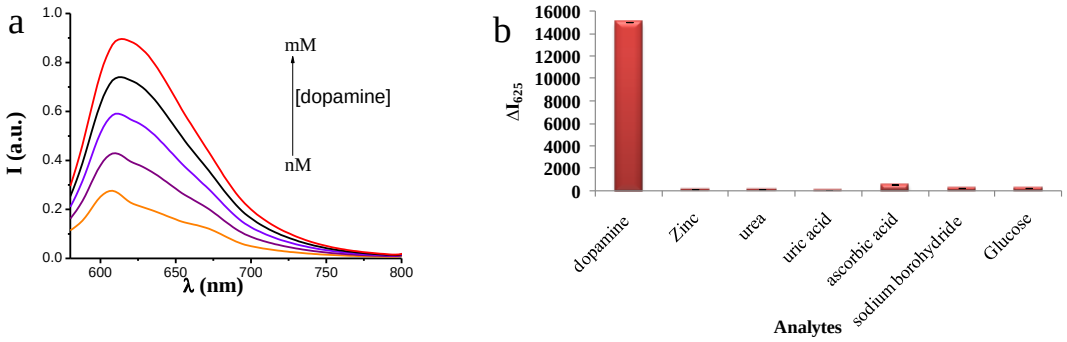

Figure 37: a) Increase in fluorescence intensity with an increase in dopamine concentration b) Selectivity of cysteine gold cluster on dopamine detection.

On finding the sensing possibility of dopamine in aqueous solution, dopamine sensing was attempted in live cells. Dopamine is a neurotransmitter, and it is usually seen in brain cells. Hence the detection of dopamine was tested using C6 brain cells. The presence of dopamine was evaluated after incubating with different concentrations of dopamineinAuC (1 mg/mL) for30 s inC6 cells. The fluorescence emission from the cysteine cluster facilitated the microscopic imaging of the cells when different concentrations of dopamine were added(Figure 38a). As the concentration of dopamine increases, showed an enhanced fluorescence intensity. It is also evident from the fluorescence intensity scale reading (Figure 38b). Herein, AuC not only takes part in sensing application but also contribute to the microscopic imaging of the cells.

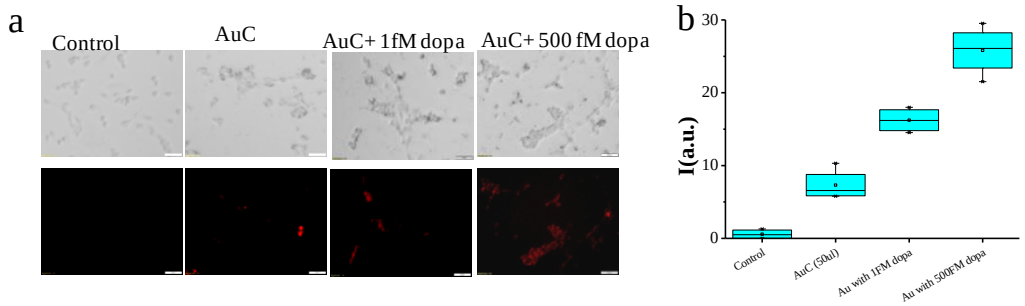

Figure 38:a) Fluorescence microscopic images of C6 cells incubated with dopamine in femtomolar concentration (fM), b) Gary scale reading of dopamine incubated cells with control.

4.2.3. Size and zeta potential analysis

Size and zeta potential analysis of AuC and dopamine incubated AuC showed that as the concentration of dopamine increases, both size and zeta potential decreases (Figure 39a &b).

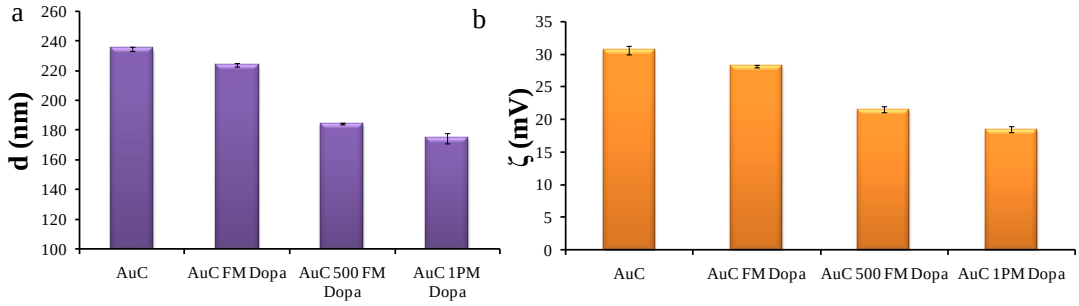

Figure 39: a) Size analysis of AuC and different concentrations of dopamine incubated AuC and b) zeta potential of AuC and different concentrations of dopamine incubated AuC.

4.2.4. *In vitro* imaging of different cell lines using cysteine gold cluster

Before performing *in vitro* imaging, we have checked the *in vitro* cytotoxicity of AuC in L929 and HeLa cells using standard MTT assay(Figure 40).

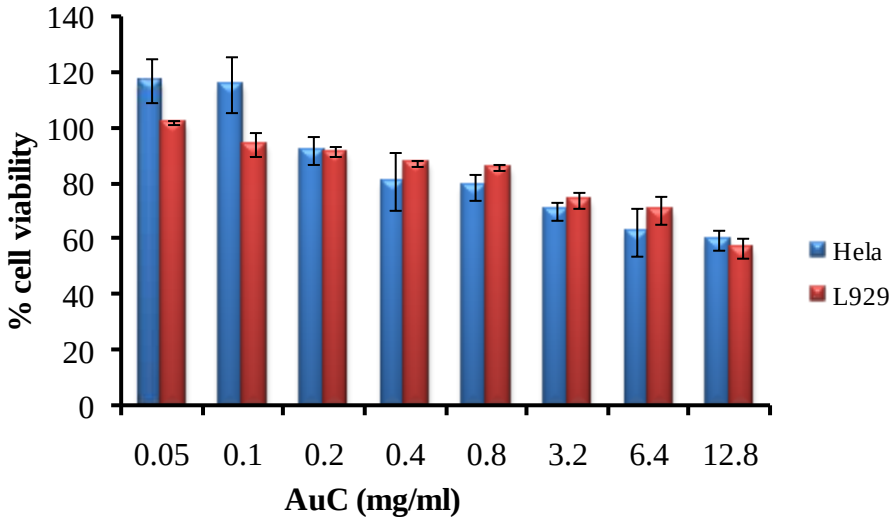

Figure 40: Cytotoxicity of cysteine gold cluster in L929 and HeLa cells.

At lower concentrations,thecells were completely viable and showed more than 50% cellular viability at a higher concentration of 12.8 mg/mL in the case of L929 fibroblasts cells. At lower concentrations, the cell viability was much higher or even 100%.HeLa cells also showed similar results to that of L929. This data confirms that AuC is a safe candidate that can be used in cellular studies.

The red-emittingAuC facilitated the cellular imaging without the addition of highly toxic extra dyes in L929 and HeLa cells. The cells with AuC shows good imaging capacity within 3h of incubation compared to the control cells. This result also an indication of the passive cellular uptake of the material in both L929 and HeLa cells (Figure 41).

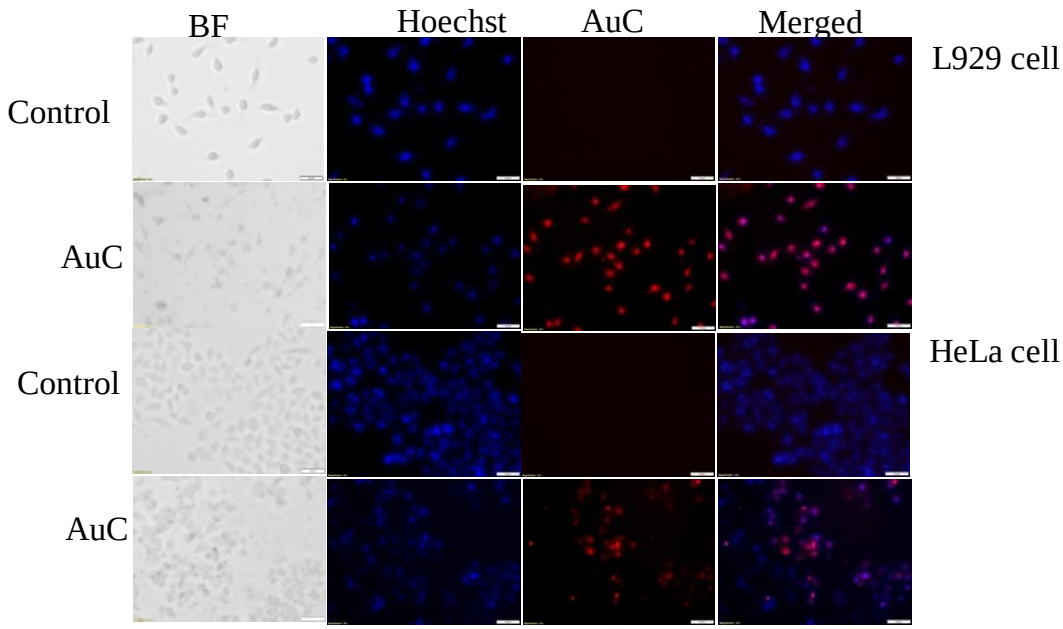

Figure 41: Imaging of cells using AuC.

4.3.Fluorescent multifunctional gold based system for imaging and therapy

Gold nanorod is the most studied anisotropic system, which is used in biomedical applications. It has two surface plasmon bands from longitudinal and transverse absorption. This longitudinal-NIR absorption makes it a suitable candidate for photothermal therapy by heat generation. In this section therapeutic efficacy of GNR (photothermal therapy) along with other therapeutic strategies (chemotherapy & photodynamic therapy) were studied. It consists of two parts;1. imaging and photo-chemo therapy and 2.imaging, photothermal and photodynamic therapeutic approaches. In both parts, folic acid was used as a targeting agent to target cancercells over expressed with folate receptors specifically.

4.3.1. Gold nanorod-MTX (Mitoxantrone) nanomaterial for in vitro cancer imaging and therapy

Mitoxantrone (MTX) is a cancer drug used to treat breast cancer. In this study, a gold nanorod-MTX combined system was used to enhance the therapeutic efficacy by incorporating both photothermal therapy and chemotherapy in a single system.

4.3.1.1. Synthesis and characterisation of gold nanorod-MTX system

Initially,GNR was synthesised using seed mediated method. Then the capping agent,cetyl trimethyl ammonium bromide (CTAB), was removed using thio-amino-PEG (the system was named as PGNR) -followed by the functionalisation of folic acid for target specificity towards cancer cells (this system was named as FPGNR). Then it was functionalised with MTX and is designated asMTX@FPGNR (3.4.2-3.4.4). The functionalisations were confirmed using the UV-visible spectra of the successive products.The absorption spectrum of GNR shows typical absorption bands due to the longitudinal oscillation of electrons at 786 nm and transverse plasmon absorption band at 534 nm (Figure 42a).

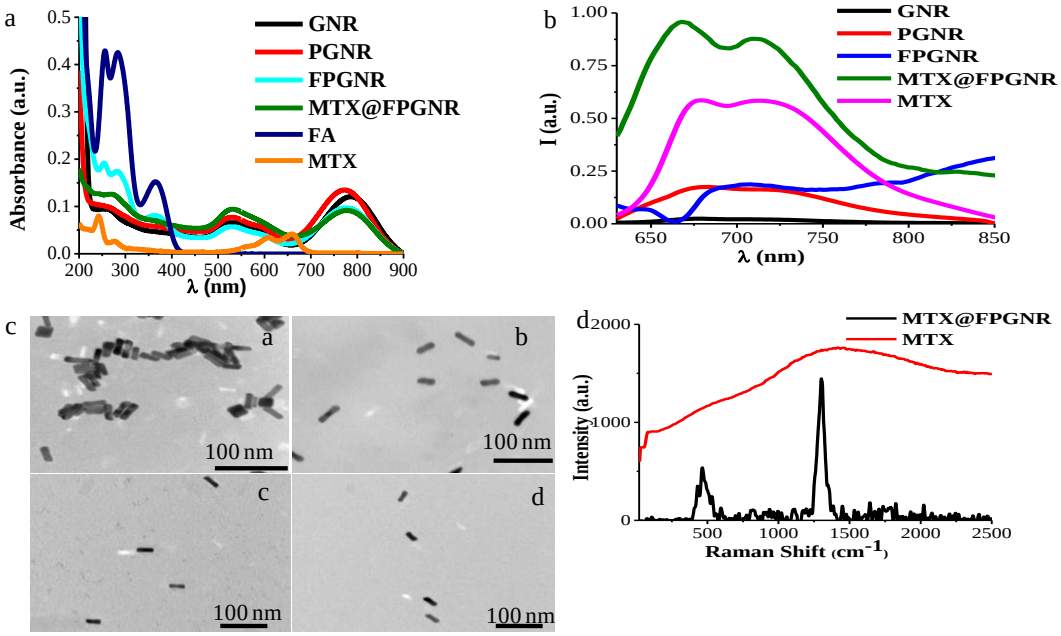

Figure 42: a)UV-Visible absorption spectra of GNR, PGNR, FPGNR, and MTX@FPGNR. b) Emission spectra of GNR, PGNR, FPGNR, and MTX@FPGNR. c) Transmission electron microscopy images of a) GNR b) PGNR c) FPGNR d)MTX@FPGNR d) Raman spectra of MTX and MTX@FPGNR.

A slightly blue shifted absorption peak at 770 nm compared to 786 nm of GNR is observed when CTAB is replaced with thio-amino-PEG to form PGNR. PGNR was further functionalized with folic acid using EDC/NHS coupling. The resultant system, FPGNR, has absorption bands at 371, 283, and 255 nm along with the longitudinal and transverse plasmon absorption bands of GNR indicating the presence of folic acid in FPGNR. After functionalisation with MTX, the peaks at 283 and 255 nm indicate the presence of both folic acid and MTX in the final system. Shoulder peak at 371 nm can be due to the presence of folic acid (Figure 42a) in MTX@FPGNR.

The fluorescence spectroscopic study shows very weak emission profile for PGNR and FPGNR in the NIR region at 600 nm excitation. The drug MTX has two prominent emission peaks at 679 and 714 nm (Figure 42b).After conjugation of MTX, two peaksat 668 and 711 nm are available for MTX@FPGNR. Electron microscopic analysis reveals the formation of anisotropic GNR with an average aspect ratio of 3.2±0.18. Further functionalisation did not alter the aspect ratio considerably (Figure 42c).

Raman spectrum of the drug, MTX in the aqueous medium, did not show any prominent peaks due to the interference of high fluorescence. However, the Raman peaks are well defined in the case of MTX@FPGNR, probably because of the enhancement of Raman peaks due to SERS phenomenon withGNR. Raman spectrum of MTX@FPGNR shows prominent peaks at 1300 cm^{-1} and 464 cm^{-1}. These are due to ring stretching mode coupled with C-O bond vibrations and C-N in the aromatic ring and C-C-O bonds present in folic acid and MTX of MTX@FPGNR(Figure 42d). Modifications of GNR at different stages were also confirmed using FT-IR spectroscopy (Figure 43). The initial system, GNR, showed the characteristic vibrations at 929, 1000, 1061 $cm^{-1}$of CTAB (Figure43). Upon surface modification with PEG, all peaks of CTAB disappeared, and other additional peaks were observed. The peak is the range 3269-3196 $cm^{-1}$is due to the primary amine and peak at 2892 $cm^{-1}$is due to CH stretching vibration. Peaks at 1597, 1122, and 667 $cm^{-1}$are the vibrational bands of amino groups. FT-IR spectrum of FPGNR showed peaks of amino group and amide group at3391 and 653 cm^{-1}, and 1606, 1119 $cm^{-1,}$ respectively.The presence of an aromatic ring peak at 891 cm^{-1} was also observed.

MTX@FPGNR showed peaks at 3268 cm^{-1} due to the vibrations of phenolic OH group. Peak at 2880 and 2326 cm^{-1} are due to CH and C=C vibrations. The peaks at 1739, 1373 cm^{-1}indicate the vibrations of ester groups formed by the bonding of MTX to FPGNR. Peak at 1655 and 860 $cm^{-1}$are the vibrations of amide group and aromatic ring, respectively.The peak at 1556 cm^{-1}indicates the presence of an amine group in it.

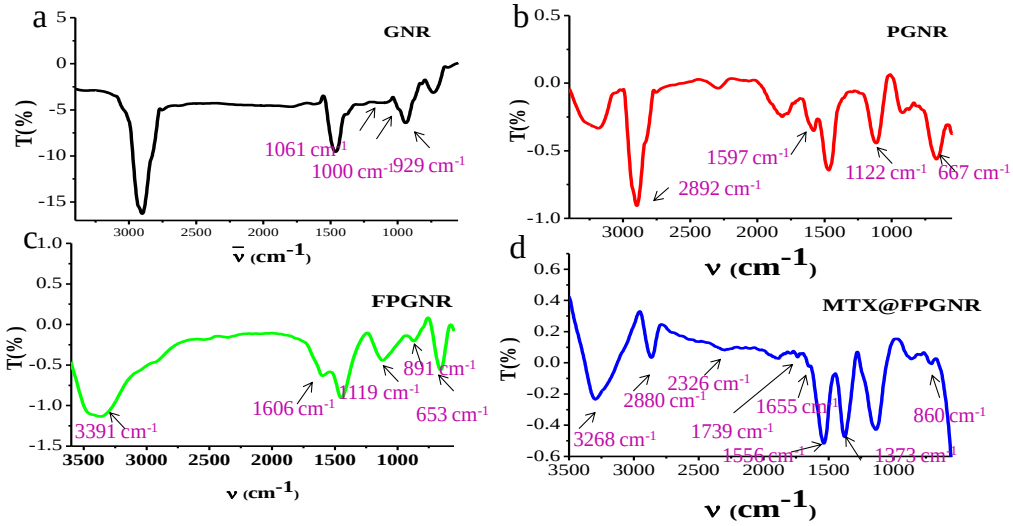

Figure 43: FT-IR Spectra of a) GNR, b)PGNR, c) FPGNR, and d) MTX@FPGNR.

Heat generation efficacy of MTX@FPGNR was evaluated with GNR and MTX. It is found that MTX@FPGNR achieved 50°C within 5 minutes of 808 nm laser irradiation, while GNR alone generated heat of the order of 60°C (Figure 45). In the case of MTX drug alone, the heat generation was only up to 32°C, which is not sufficient to kill cancer cells. So, the combined system could serve as a good candidate for photothermal treatment.

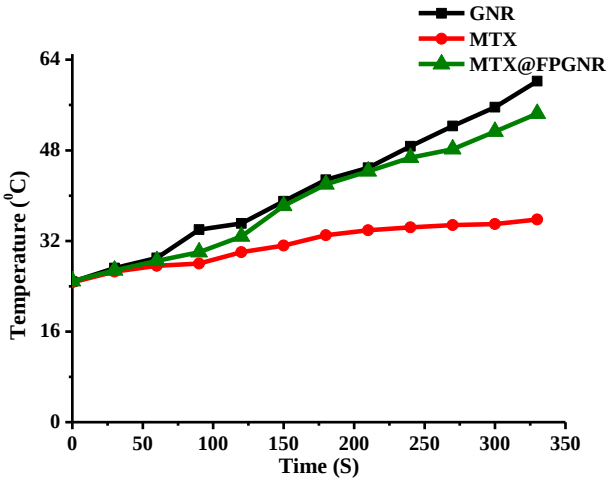

Figure 44: Heat generation upon 808 nm laser irradiation with GNR, MTX, and MTX@FPGNR.

Zeta potential at every stage of functionalisation was monitored to evaluate more about the behavior of the particles. When the first system, GNR, had a zeta potential of +14.6 mV, the zeta potential of PGNR decreased to +7.19 mV. Further, conjugation with folic acid reduced the zeta potential to -5.86 mV. Finally, MTX@FPGNR at normal pH gives a zeta potential of -1.06, which in acidic pH changes to 4.93 mV (Figure 45).

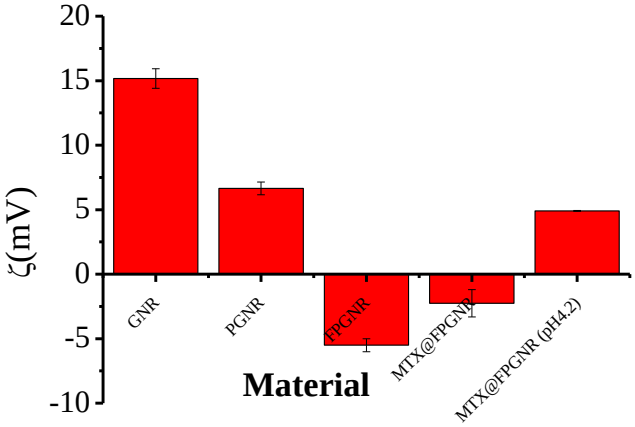

Figure 45: Zeta potential of GNR, PGNR, FPGNR, MTX@FPGNR, and MTX@FPGNR at pH 4.2.

The release of drug MTX from MTX@FPGNR was studied using fluorescence spectroscopy. On laser irradiation, a controlled and effective release of the drugis observed at acidic pH followed by an increase in the fluorescence from the drug due to the unique design of the final system (Figure 46). The drug release not effective at neutral pH and also at both pHs without laser irradiation.

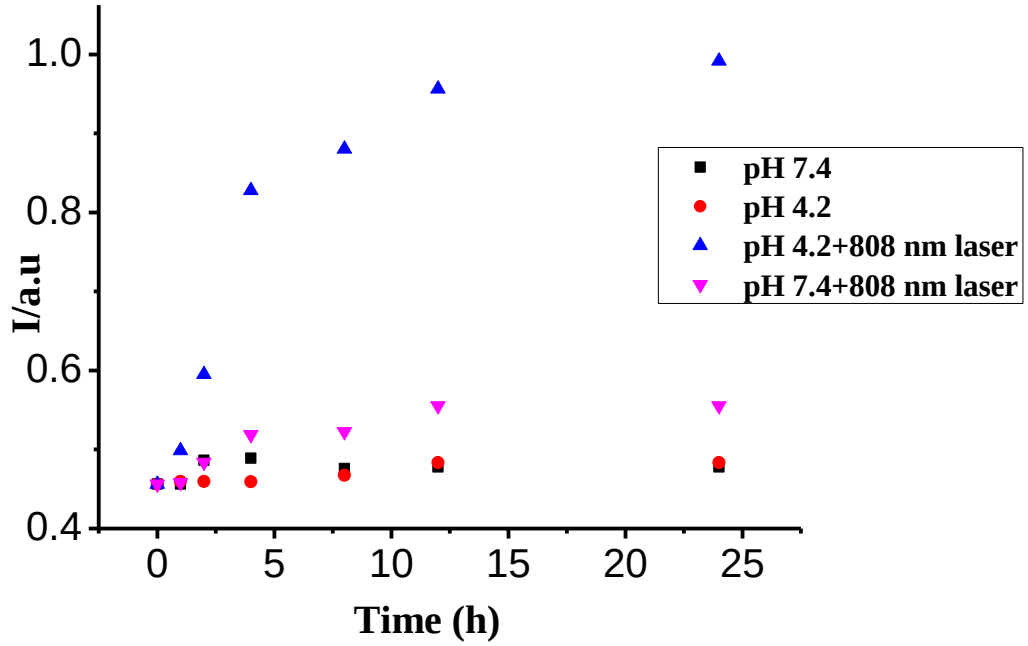

Figure 46: Time-dependent fluorescence enhancement (drug release study) at pH 7.4, pH 4.2, pH 4.2 after laser irradiation, and pH 7.4 after laser irradiation.

4.3.1.2. In vitro studies

Theso developedgold nanomaterials were tested for its long term cellular cytotoxicity in normal L929 fibroblast cell line, using standard MTT assay (Figure 47).At 24 h of incubation, GNR showed less cellular viability of the order of below 80%. The functionalisation of GNR with PEG and folic acid reduced the toxicity showing cell viability of more than 95% even at a higher concentration of 2 mg/mL.On encapsulation of MTX drug in FPGNR, the cell compatibility was retained in L929 fibroblast cells.

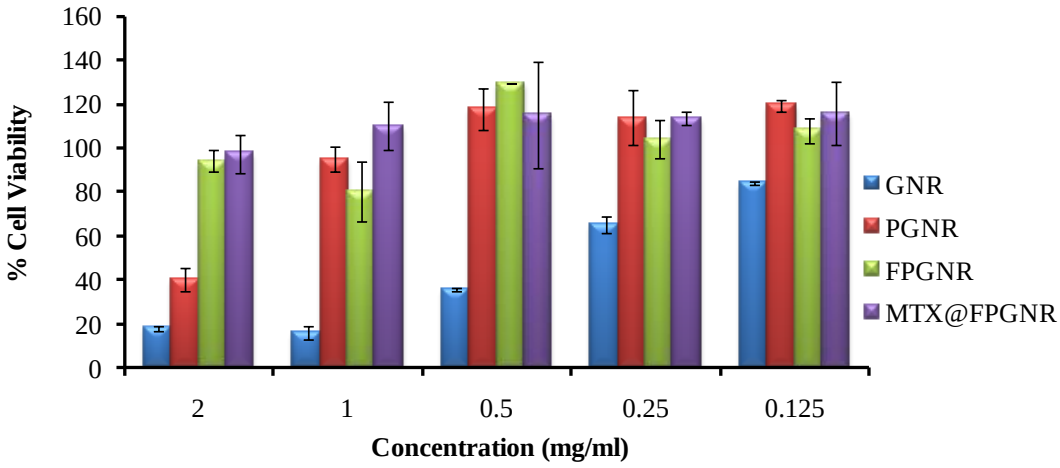

Figure 47: Cytotoxicity of GNR. PGNR, FPGNR, and MTX@FPGNR in L929 cells.

Cancer cell targeting potential of MTX@FPGNR was studied in different cell lines; L929, C6, and HeLa having different degrees of folate overexpression. Cellular uptake over 6 h was noted by fluorescence microscopic images (Figure 49). According to the degree of folate receptor overexpression, L929 cells showed very less uptake, C6 cells show more material uptake, and HeLa cells showed the most significant and higher material uptake, fromthe fluorescence intensity.

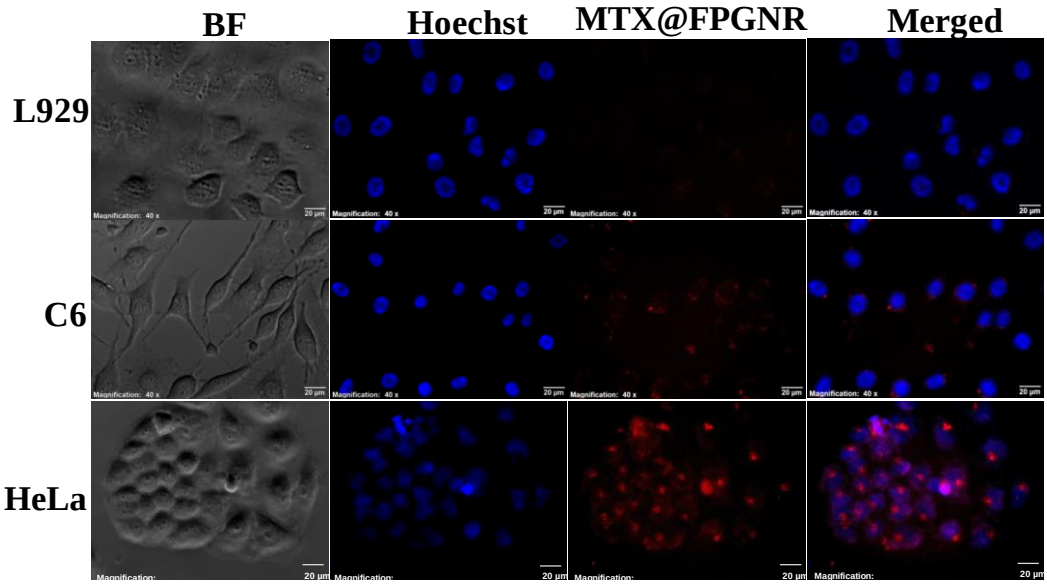

Figure 48: Cellular uptake of MTX@FPGNR. a) bright field b) Hoechst c) MTX@FPGNR and d) Overlay Images.

In vitro drug release study was done using C6 and HeLa cells. Irradiation of 808 nm laser on the cells incubated with the materials an enhanced fluorescence

intensity was observed, it maybedue to the release of the drug. The drug release was again confirmed using SERS, where non-irradiated cells showed well defined Raman peaks due to the SERS effect.At the same time, 808 nm laser irradiated cells showed an unresolved Raman spectrum hindered by the fluorescence of the drug on its release during laser irradiation (Figure 49).

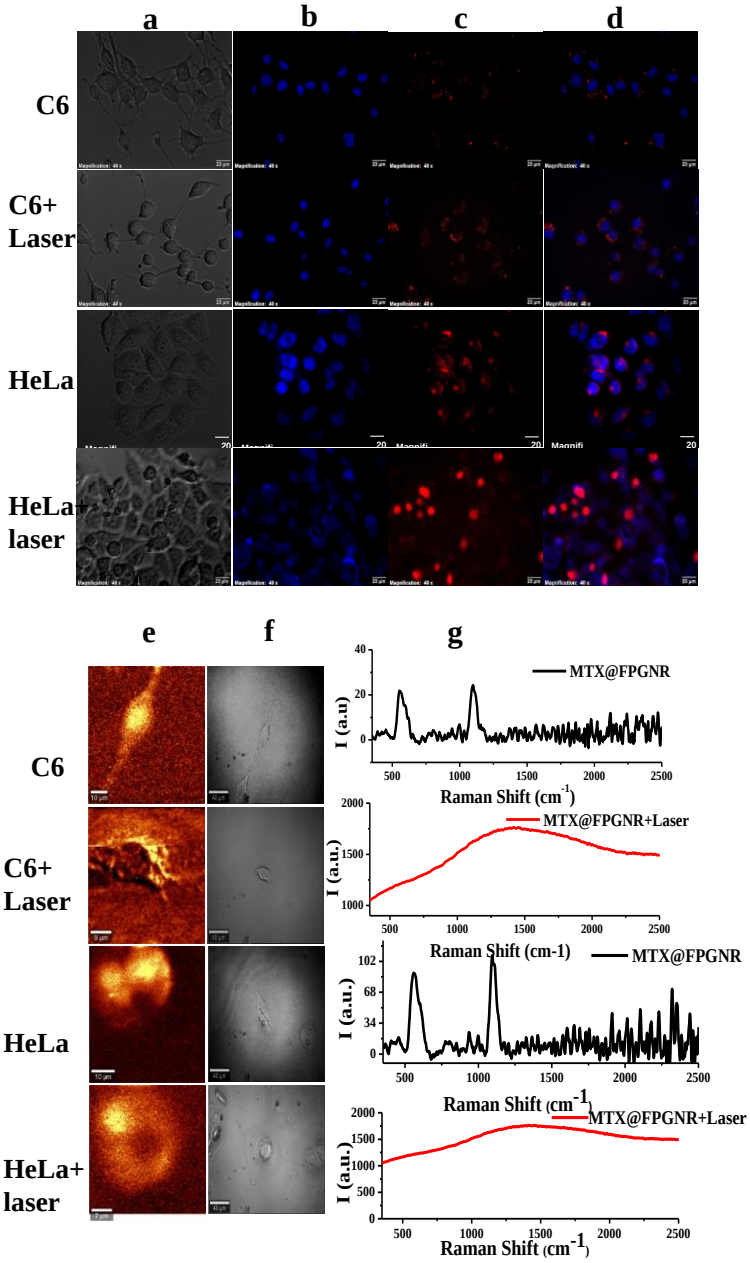

Figure 49: Drug release evaluation using fluorescence microscopy and Raman imaging. a) bright field b) hoechst c) MTX@FPGNR and d) Overlaid images e) Raman image f) Raman map g) Raman spectra of corresponding cells.

After proving the imaging property, the photo thermal therapeutic effect was evaluated in C6 glial cells and HeLa cells using live/dead assay and MTT assay, with 808nm laser irradiation (Figure 49a, c,andd). Also, the therapeutic efficacy of the system MTX@FPGNR and MTX (drug) after irradiation with 808 nm laserwas compared. It is found that the combined system showed more effective cell death in comparison with MTX (49 d).

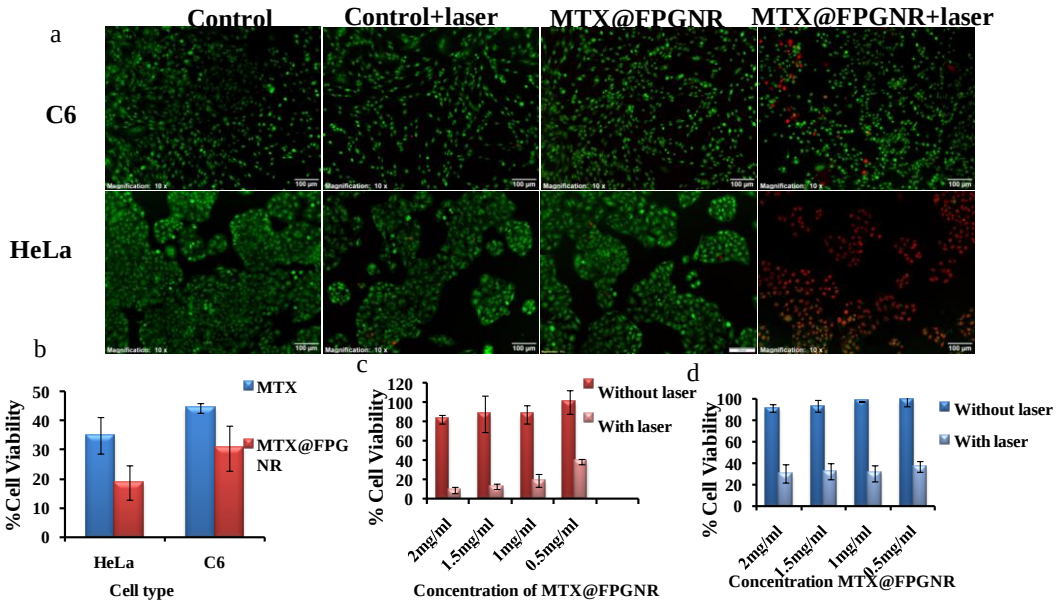

Figure 50: a)Live dead assay of MTX@FPGNR in HeLa and C6 cells b) comparison of therapeutic efficacy of MTX and MTX@FPGNR after laser irradiation using MTT assay. MTT evaluation of therapy with and without laser incubated with MTX@FPGNR (c- HeLa, d- C6).

Owing to its strong NIR absorbance and high heat generation efficiency in solution, MTX@FPGNR incubated and laser (808 nm, for 1.30 s) irradiated cells showed more cell death in comparison withnon-irradiated region. MTT assay also showed more cell death in laser-irradiated cells having MTX@FPGNR compared with the non- irradiated region.

4.3.2. Gold nanorod-protoporphyrin (PPIX) nanomaterial for cancer imaging and therapy

4.3.2.1 Synthesis and characterisation of gold nanorod-PPIX

Cetyl trimethyl ammonium bromide (CTAB)-GNRs were synthesised by the seed mediated method. CTAB was replaced with reduced glutathione, and the system was abbreviated as GSH@GNR. Protoporphyrin IX was added to GSH@GNR as an imaging and photodynamic therapeutic moiety. This system is abbreviated as P@GNR. Finally, folic acid was functionalised with the P@GNRsystem as a targeting molecule. The final system was termed asF@PGNR (3.5.1-3.5.2). The functionalization and their respective properties were confirmed at different stages.

UV-visible absorption spectra of different stages of synthesis were done (Figure 51). It was noted that the absorption spectrum of GNR shows longitudinal and transverse peaks at 523 and 743 nm. GSH@GNR also retains both the plasmon peaks.

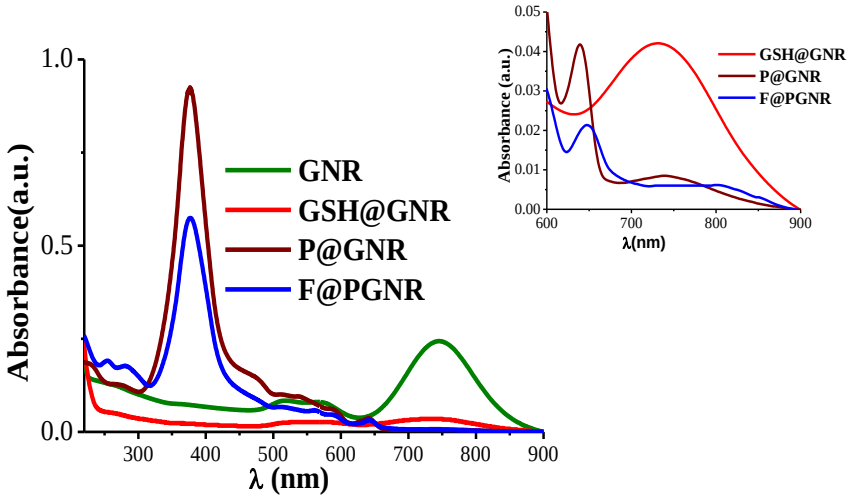

Figure 51: Absorption spectra of GNR, GSH@GNR, P@GNR, and F@PGNR. Inset shows the absorbance of GSH@GNR, P@GNR, and F@PGNR in the region 600-900 nm.

After PPIX conjugation, P@GNR shows the characteristic soret band of the photosensitizer (PS) at 376 nm. A slight blue shift of the Q bands (536, 585, and 640 nm) is observed in P@GNR compared to pure PPIX (Figure52).

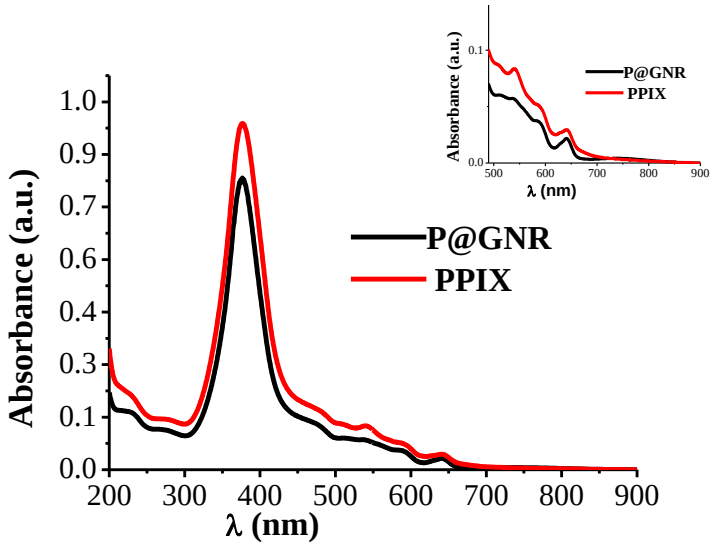

Figure 52: UV- Visible absorption spectra of P@GNR and PPIX. Inset shows the absorption of P@GNR and PPIX in the region 500-900 nm.

Additional absorbance peaks at 284 and 254 nm are observed on folic acid conjugation in F@PGNR (figure 43). In the case of P@GNR and F@PGNR, less intense broad shoulder peaks observed in the range of 450 to 550 nm are due to the transverse surface plasmon absorption of GNR (figure 52).

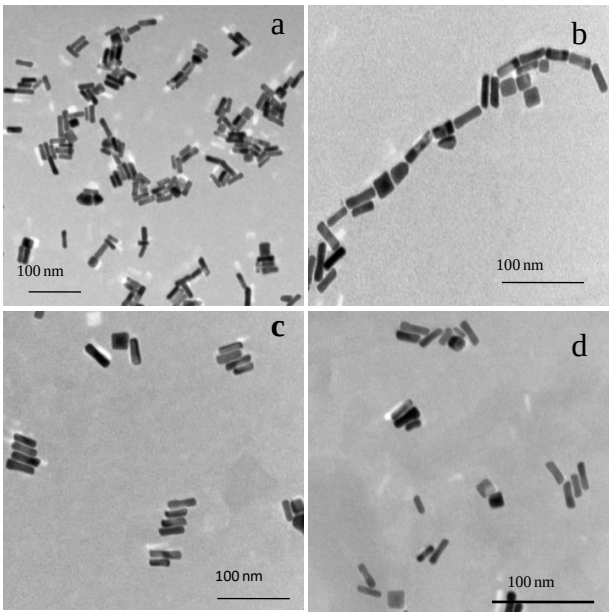

Figure 53: TEM images of a) GNR b) GSH@GNR c) P@GNR and d) F@PGNR

The formation of GNR morphology is clear from the TEM images (Figure 53a) whose aspect ratio was 3.3±0.3. TEM of GSH@GNR witnessed a linear assembly (Figure 53b). On conjugation with protoporphyrin IX, the linear assembly breaks (Figure 53c), and a peculiar lateral assembly is formed. Finally, on folic acid conjugation, the system retains the same orientation with a partial breakage of lateral assembly.

FT-IR data gives enough information to confirm the functionalisation of GNR. The initial system, GNR, showed peaks at 961, 936, and 1484 cm^{-1} in the FT-IR spectrum (Figure 54). Strong, broad vibrational peak around 3421 $cm^{-1}$was observed for GSH@GNR. On functionalisation with PPIX, the peak at 3400 cm^{-1} was observed. The amide bond is clear from 1272 cm^{-1} peak was observed in P@GNR. The presence of carboxylic acid in P@GNR gives rise to the 1724 cm^{-1} peak. Similar observations are seen in the case of F@PGNR.

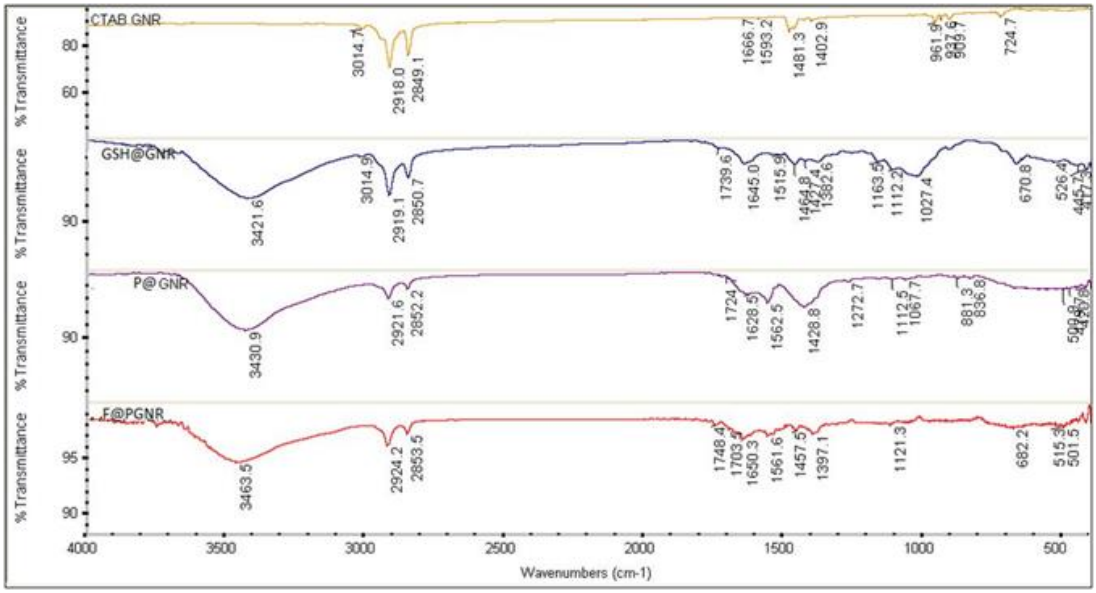

Figure 54: FT-IR spectra of GNR,GSH@GNR, P@GNR, and F@PGNR.

Fluorescence emission profiles of the samples at various stages of synthesis were evaluated and are shown in Figure 55a. Developed GNR shows characteristic weak emission at 592 nm at an excitation of 500 nm (Figure 55b &c). GSH@GNR retains GNR fluorescence. On conjugation with protoporphyrin, the combined

system gives rise to a strong NIR emission at 703 nm, whereas the emission at 592 nm weakens on surface functionalisation of P@GNR with folic acid, the emission of F@PGNR further redshifts to 730 nm. In the case of GNR conjugated with a fluorescent molecule, usually, a decrease inthefluorescence or quenching is witnessed. However, here we are noticing a retained fluorescence. The fluorescence lifetimes of the emission at 592 nm of GNR and P@GNR were noted with two excitations (451 nm and 344 nm) to explain the origin of this red emission. At 451 nm, the lifetime of GNR and P@GNR is 5.58 ns and 4.43 ns, respectively (figure 55e). Whereas at 344 nm excitation, the lifetime values are 0.021 and 2.34 ns (figure 55f).

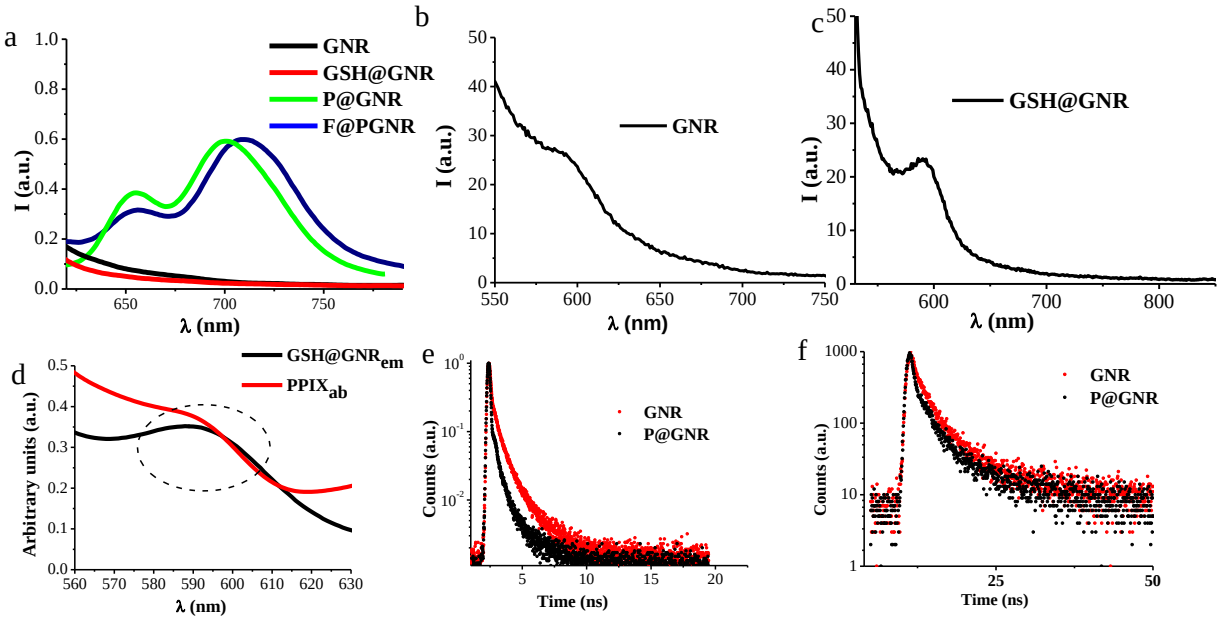

Figure 55: Emission spectra of a) P@GNR and F@PGNR b) GNR and c) GSH@GNR d) Combined spectra- absorption of PPIX and GSH@GNR e)fluorescence lifetime decay of GNR and P@GNR at 451 nm f) fluorescence lifetime decay of GNR and P@GNR at 344 nm.

Considering the importance of zeta potential evaluation during different functionalisation over GNR, zeta potential at every stage of synthesis was measured (figure 56 b). While GNR had a zeta potential of +15.45 mV, it has decreased to +3.5 mV for GSH@GNR. Further, conjugation with PPIX decreased the zeta potential to -29.3 mV. F@PGNR showed a zeta potential value of -43.4 mV.

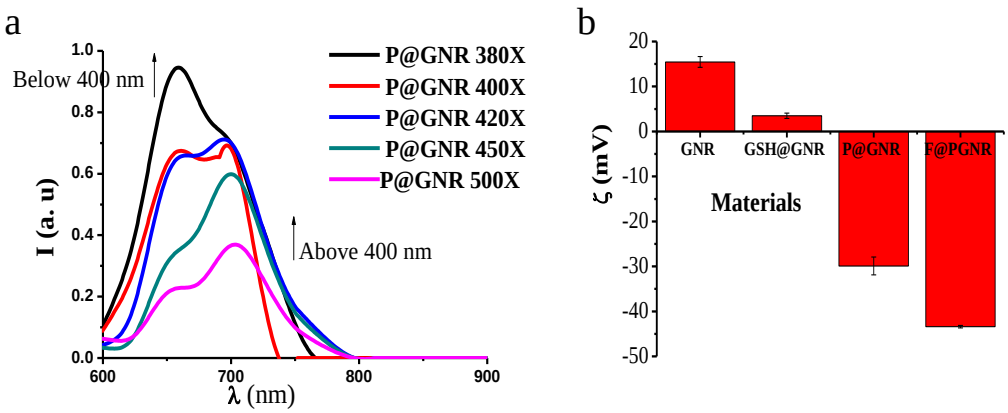

Figure 56: a) Emission spectra of P@GNR at different excitation b) Zeta potential of GNR, GSH@GNR, P@GNR and F@PGNR.

The imaging capability of P@GNR and F@PGNR was checked by evaluatingthe fluorescence signal from the samples using the imaging system (IVIS imaging system). In comparison with PBS, both P@GNR and F@PGNR showed a higher fluorescence signal, with F@GNR showing maximum signal (Figure 57).

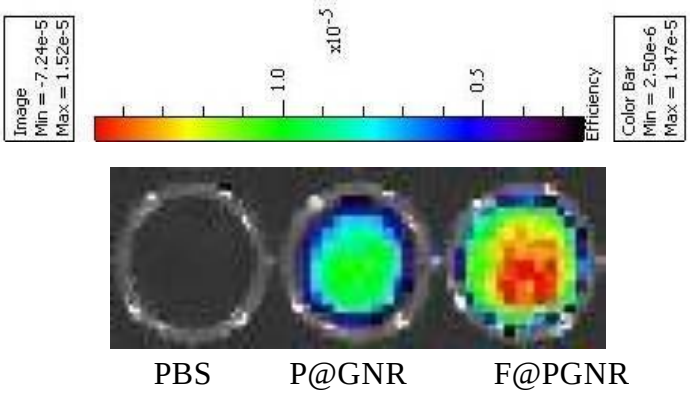

Figure 57: Fluorescence signal from PBS, P@GNR, and F@PGNR.

Further, to exploit the therapeutic potential of the developed system, the photothermal efficacy of F@PGNR was evaluated using 808 nm laser irradiation. The strong absorption of GNR in the NIR region will facilitate thermal therapy applications. Heat generation and increase in temperature to the order of 60^0C was achieved within 4 minutes of irradiation, at which temperature cancer cells are prone to cell death while undergoing photothermal therapy (PTT) (Figure 58).

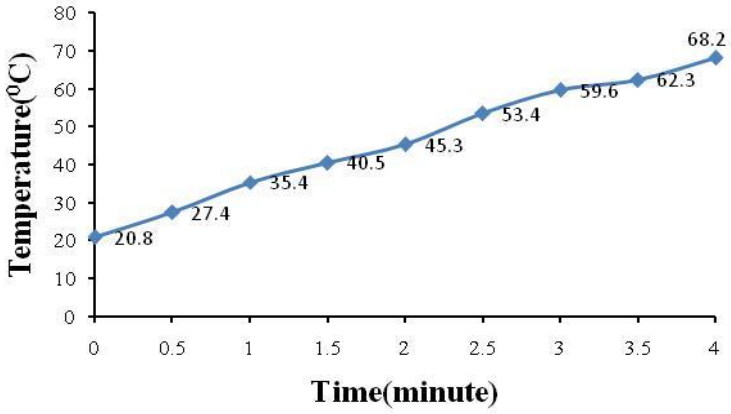

Figure 58: Time-dependent temperature enhancement of F@PGNR on exposure with 808 nm laser.

The singlet oxygen generation capacity of the system was also evaluated for PDT application to impart a dual therapeutic approach,which could increase the efficiency of treatment. The singlet oxygen production was confirmed from time-dependent depletion of the absorption of diphenylisobenzofuraan (DPBF) at 398 nm. When compared to PPIX, which is an FDA approved PS for PDT, P@GNR shows a singlet oxygen yield of 44.7% (Figure 59). The final system, F@PGNR, showed an increase in the singlet oxygen generation upon 67.56%.

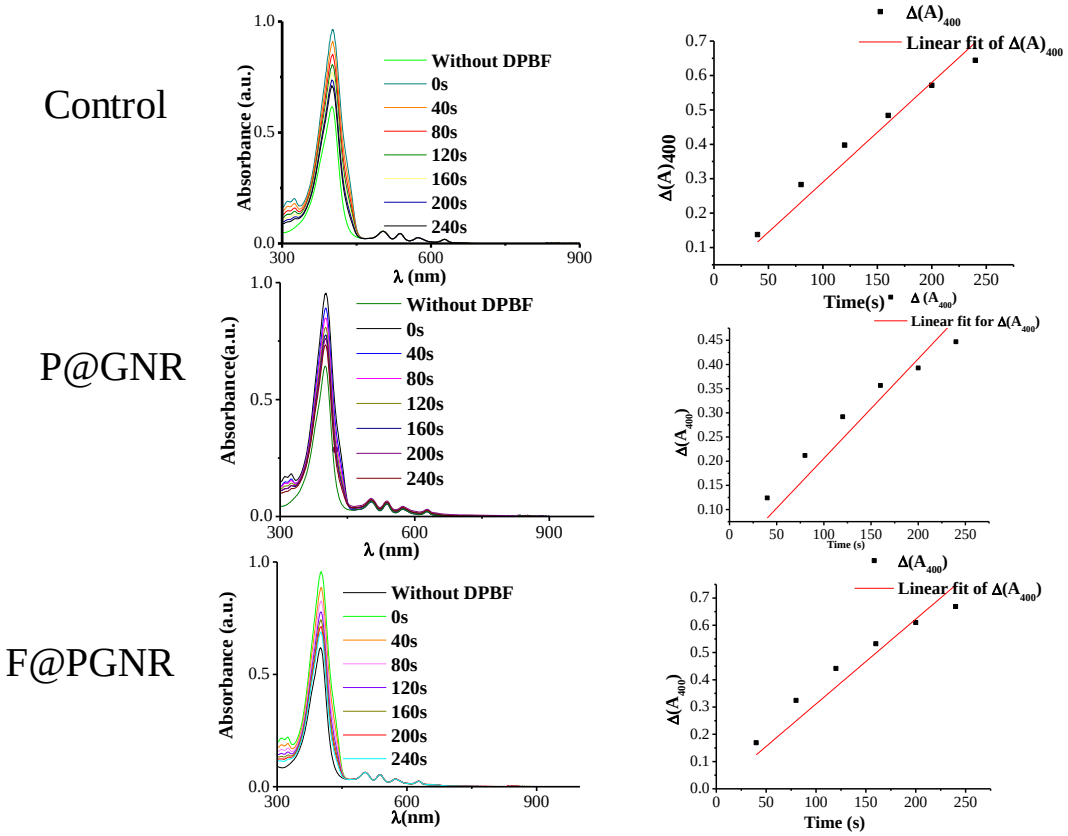

Figure 59: PDT, evaluation of singlet oxygen capacity of P@GNR and F@PGNR using PPIX as standard.

4.3.2.2.In vitro analysis of gold nanorod-PPIX system

The biocompatibility of the developed materials was checked in the normal mouse fibroblast cell line (L929) using MTT assay (Figure 60). GNR is found to be less cytocompatible due to the presence of highly toxic CTAB over it. The toxicity is reduced substantially in GSH@GNR due to the replacement of CTAB with GSH. The final multifunctional system (F@PGNR) showed more than 80% cell viability even at a higher concentration of 1 mg/mL and for a longer period (72h) of incubation. From the observation,it is clear that even after a long time period of incubation, the material is safe for the normal cell line.

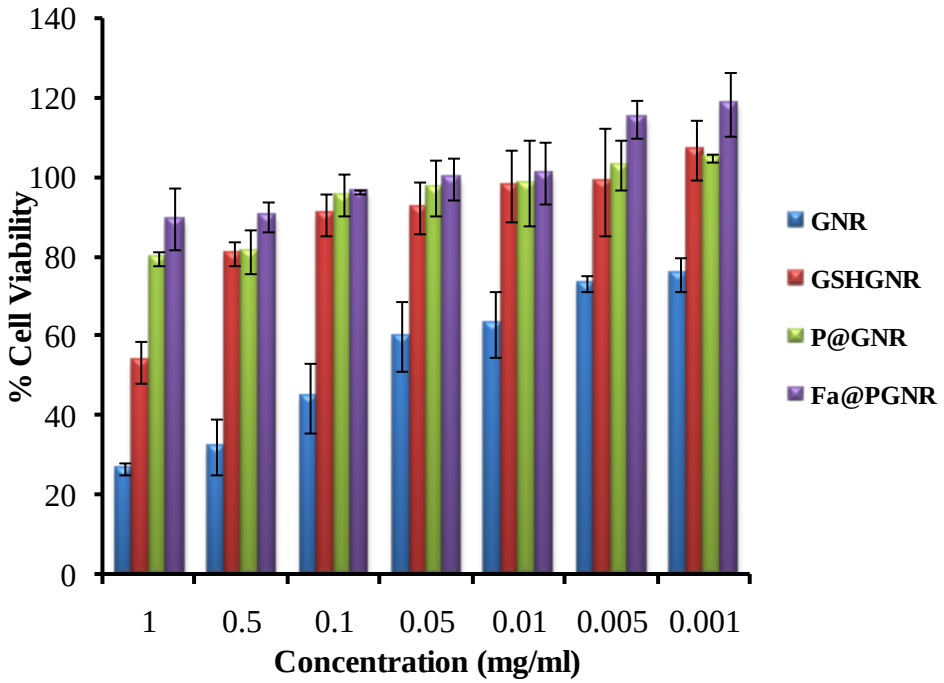

Figure 60: Cytotoxicity study (MTT assay) of GNR, GSH@GNR, P@GNR and F@PGNR using L929 cell.

To prove the cellular uptake and targeted PTT and PDT at the cellular level, breast cancer cell lines, MCF7 was used as it is known to have folate receptors over-expressed. F@PGNR showed enhanced cell uptake after 3h of incubation in comparison with P@GNR (Figure 61A&B). From Z-stacking images most of the particles are localized inside the cytoplasm with little uptake in the nucleus was observed. It was due to the nonspecificity in the uptake of the nanoparticles by the nucleus (Figure 61C). Targeted PDT and PTT of P@GNR and F@PGNR were also checked in MCF 7 cells by irradiating it with 530 nm (40 s irradiation) and 808 nm (50 s irradiation) lasers respectively. Concentration-dependent toxicity of cancer cells was quantified by measuring the activity of live cells using mitochondrial reductase enzyme assay (Figure 62a&b). MCF7 cells treated with P@GNR and F@PGNR without laser irradiation showed more than 80% cell viability even with 1mg/mL solution of the materials. On laser irradiation, all the concentrations showed a decrease in viability. IC_{50} values for PTT and PDT are found to be 1 mg/mL and 0.5 mg/mL respectively.

PDT and PTT were also confirmed using the live/dead assay using MCF7 cells. After treating the cells with the particles for 3h, the washed cells were irradiated with 530 nm laser for 40 s with a power of 0.1W, for PDT. The acridine orange & ethidium bromide-stained F@PGNR treated cells showed considerable cell death compared to P@GNR treated group (Figure 61 a2-c2). Live dead assay of the cells after performing PTT for 50 s with 808 nm laserusing F@PGNR also showed considerable cell death in comparison with control and nontargeted material treated cells (Figure 61a1-c1).

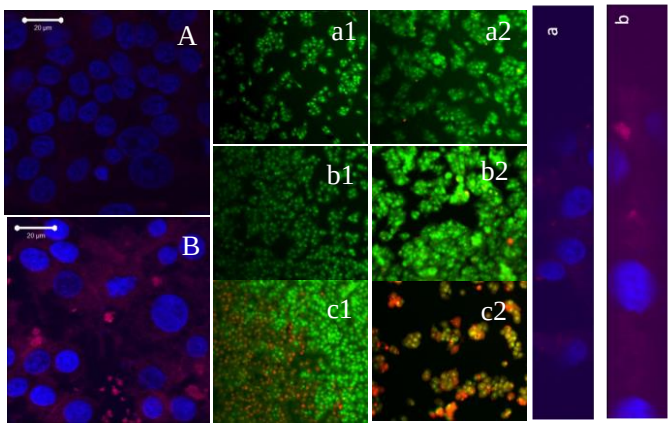

Figure 61: Uptake of P@GNR and F@PGNR using MCF7 cells (A-C), Live dead assay after PTT; control, P@GNR, and F@PGNR (a1, b1,c1, respectively).Live dead assay after PDT; control, P@GNR, and F@PGNR (a2, b2, c2, respectively).

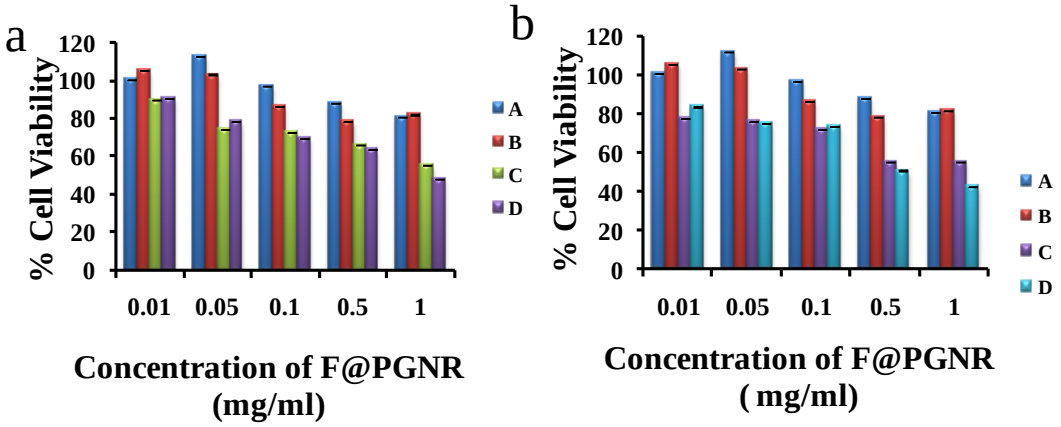

Figure 62: a) Cellular viability of different concentrations of F@PGNR with and without 808nm laser (PTT) using MCF7 cells at two different period of incubation b) Cellular viability of different concentrations of F@PGNR with and without 530 nm laser (PDT) using MCF7 cells at two different period of incubation.

4.3.2.3. In vivo analysis of gold nanorod-PPIX system

Followed by the proof of successful PDT and PTT efficiency *in vitro*, P@GNR and F@PGNR were evaluated *in vivo* in mouse tumor models. Initially, the targeted imaging capacity of the materials was evaluated by intravenous injection of 500 µl of 1mg/mL P@GNR, and F@PGNR in two groups of animals and the third group of tumor-bearing animals withsaline injection served as control. The imaging potential of the system F@PGNR was evaluated in a live animal using the Xenogen IVIS Spectrum animal imaging system. Enhanced and focused signal from the induced tumor was clear for animals injected with F@PGNR. The targeted and specific tumor imaging potential is also clear, as seen by the high signal exhibited at the tumor site by the folic acid conjugated particles compared to the animals injected with P@GNR (Figure 63). After 3h, animals were sacrificed, and the harvested organs were imaged to see the bio-distribution. Here also, it is clear that the tumor mass shows maximum fluorescence (Figure 64 aandb). In case of both F@PGNR and PGNR, the fluorescence was observed from the kidneys which indicate the clearance of this particle through normal excretory system.

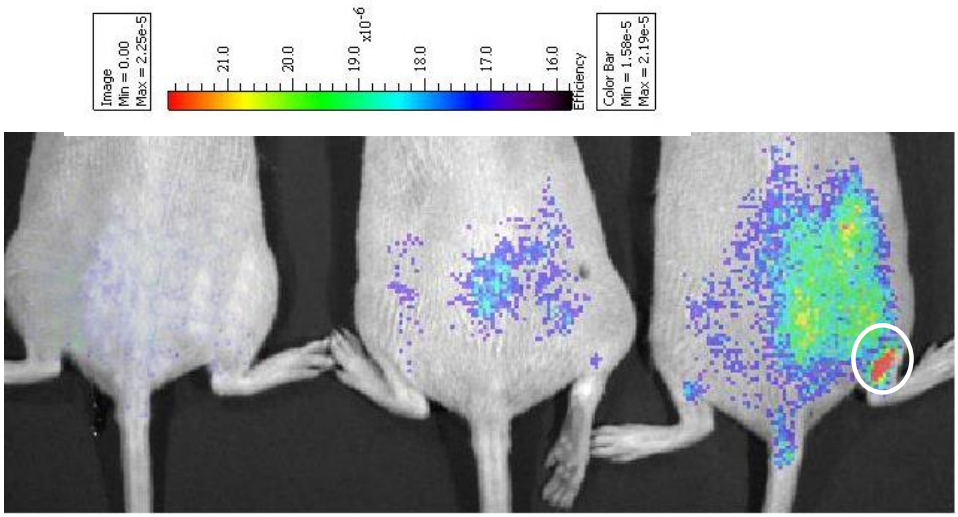

Figure 63: *In vivo* imaging of a) control b) P@GNR and c) F@PGNR.

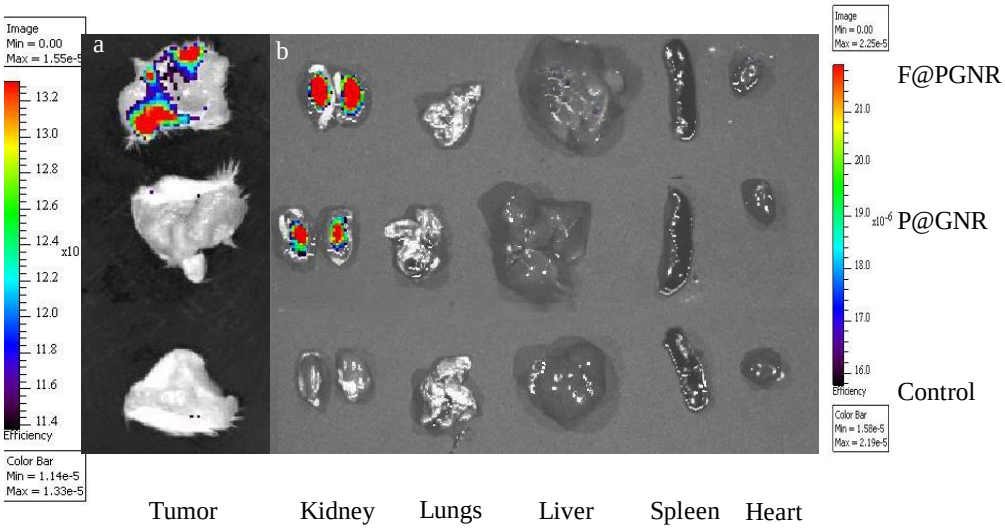

Figure 64: a)*Ex vivo* imaging of tumor region of control, P@GNR, and F@PGNR
b) Bio distribution of P@GNR and F@PGNR compared with control organs other than tumor.

After the imaging experiments, two separate groups of animals were subjected to *in vivo* PDT and PTT experiments. Animals under the PDT groups were irradiated with 530 nm laser, where two separate groups received P@GNR and F@PGNR separately. Tumor-bearing animals with saline injection, irradiated with 530 nm laser served as control. The therapeutic efficiency was evaluated by quantifying the hemoglobin concentration and redox ratio using fluorescence spectral analysis (Figure 65a&b). In the case of PDT, a reduction in hemoglobin concentration and an increase in redox ratio were seen up to 9 days, indicating the successful therapy.

Again, another set of animals in three groups were subjected to PTT with 808 nm laser irradiation with P@GNR and F@PGNR injection, separately. Tumor without particle treatment and with laser irradiation served as control (Figure 65 c&d).Animals that have undergone PTT showed a reduction in hemoglobin concentration and an increase in redox ratio within 6 days, indicating the efficacy of therapy.

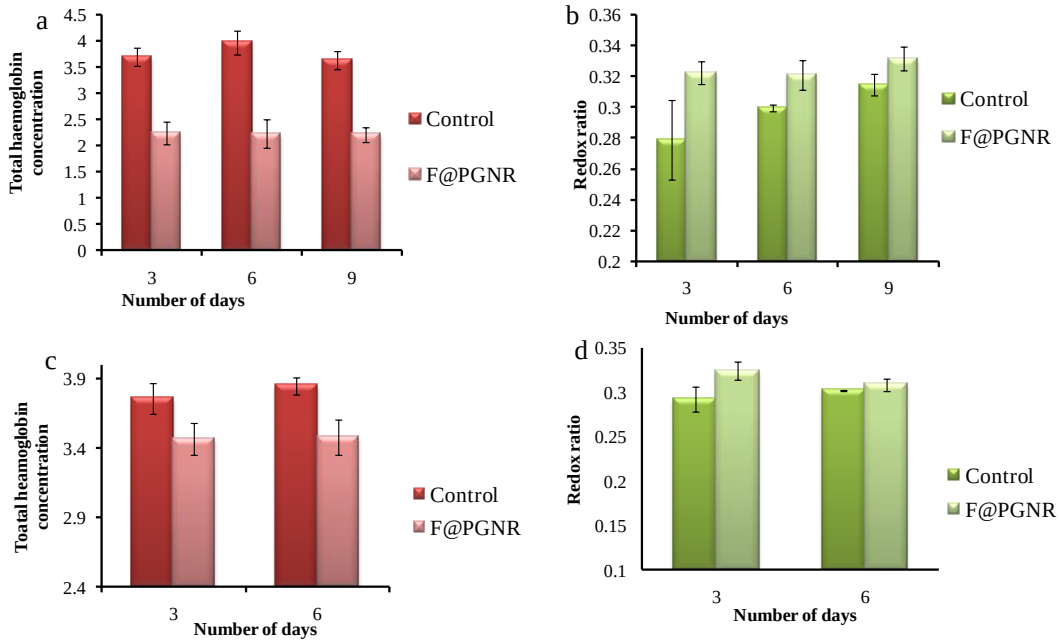

Figure 65: a& b) *In vivo* photodynamic therapeutic efficiency as evaluated by variation in total hemoglobin concentration and redox ratio,c& d) *In vivo* photothermal therapeutic efficiency as evaluated by variation in total hemoglobin concentration and redox ratio.

4.4. Gold nanorod-gold cluster hybrid nanomaterial for cancer imaging and therapy

4.4.1. Synthesis of gold nanorod-gold cluster and its characterisation

GNR was synthesised using seed-mediated method with CTAB as the ligand. For synthesising gold clusters, initially, gold nanoparticles were prepared using mercaptosuccinic acid followed by ligand etching using glutathione (3.6.2) (gold nanoparticles are termed here as GMSA). The final glutathione stabilized cluster was termed as GQC. The UV-visible spectrum of GMSA shows 520 nm absorption where as GQC didn't show any characteristic peaks (Figure 66a). It showed a valley like absorption, which is typical for gold clusters. GNR showed characteristic longitudinal and transverse absorption peaks at 707 nm and 532 nm (Figure 66b). GQC has an emission at 740 nm (Figure 66c). Transmission electron micrographs showed well dispersed GQC and GNR (Figure 66d &e).GNRhasanaspect ratio of 3.5 (Figure 66d).

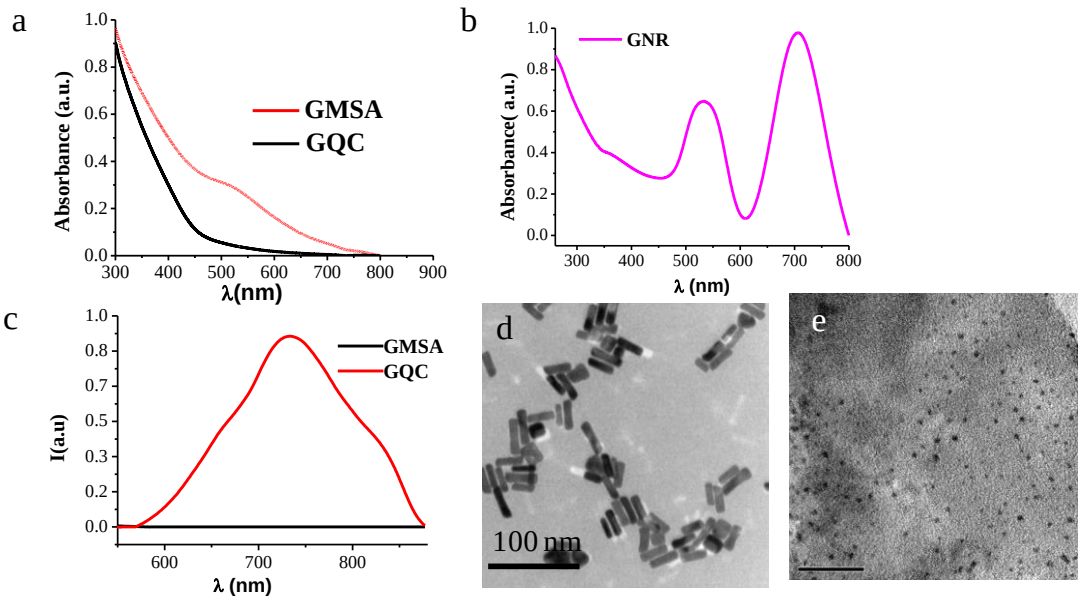

Figure 66: UV-visible spectrum of GMSA and GQC b) UV-visible absorption spectrum of GNR c) Emission of GQC and TEM images of d) GNR and e) GQC.

To have a hybrid system of GNR and GQC, they were reacted together with different reaction conditions so that the final system retains the properties of the individual systems.In one set of experiments, GNR maintained at different pHs (acidic (pH 4), basic (pH 11), neutral (pH 7)) were added to neutral GQC, and in another one, GQCs maintained at different pHs were added to neutral GNR. The absorption and emission spectra of all the samples were recorded to evaluate whether it maintains the properties of GQC and GNR (Figure 66).

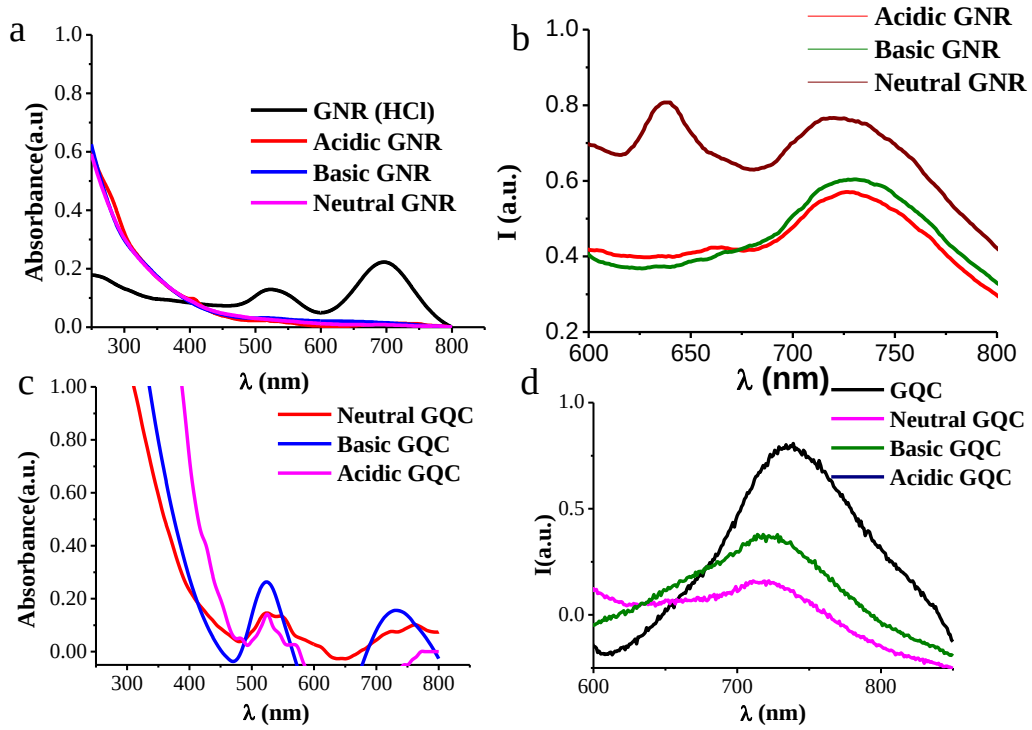

Figure 67: a) Absorption spectra of GNR, acidic, basic and neutral GNR added to neutral GQC b) corresponding emission spectra, c) Absorption spectra of acidic, basic and neutral GQC to neutral GNR and d) corresponding emission spectra.

From the spectra,acidic, basic, and neutral GNR added to neutral GQC didn't show any characteristics peaks of GNR (longitudinal and transverse peak as in figure 66 b). Whereas acidic, basic, and neutralGQC added to neutral GNR, retained the characteristics absorption of GNR. Also all showed a fluorescence emission similar to that of GQC.

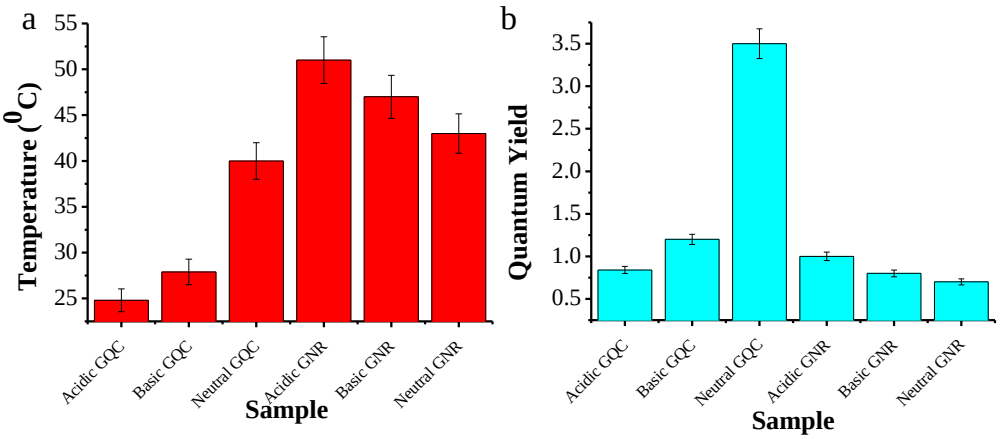

Figure 68: a) Temperature generation upon 808 nm laser irradiation b) Quantum yield of different materials.

The temperature generation capability of different systems evaluated and applying it for PTT. From the temperature generation graph,neutral GQC to neutral GNR and neutral, acidic, and basic GNR to neutral GQC systems showed temperature generation above 40^0C (68a),which is sufficient to kill cancer cells. The rest of the system showed a temperature generation below 40^0C (68a), which cannot be used for cancer treatment. For imaging applications, the quantum yield of different systems was evaluated.Neutral GQC added to neutral GNR showed a relative quantum yieldof 3.5 in comparison with bare cluster (68b)whereas all other systems showed a quantum yield of less than 1.5 in comparison with bare cluster.So,since the neutral GQC added to neutral GNR, it has temperature generation upto 40^0C and has sufficient quantum yield, this system was used for further imaging and therapy studies. It is termed as GQC-GNR.

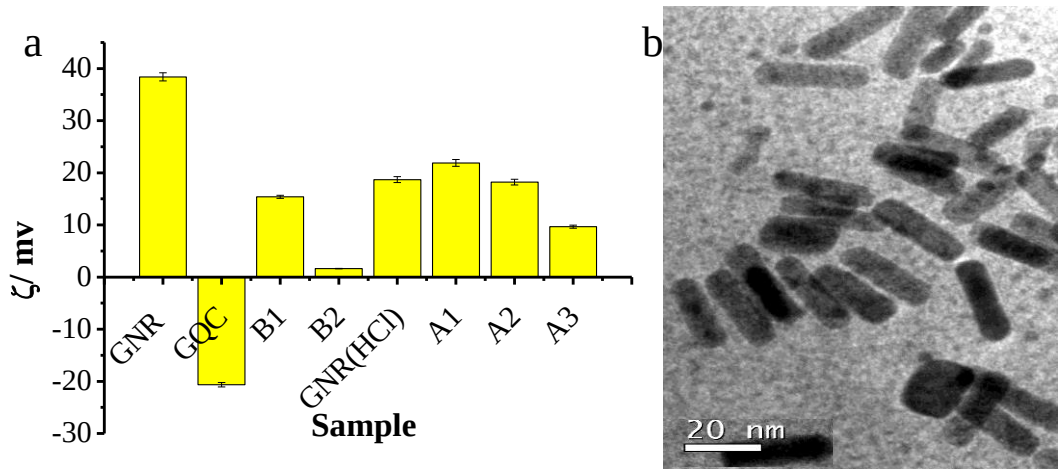

Figure 69: a) Zeta potential of different samples (A1, A2, and A3- Acidic, basic and neutral GQC to neutral GNR and B1,B2 and B3- Acidic, basic and neutral GNR to neutral GQC), b) TEM image of GQC-GNR.

GNR has +40 mVof zeta potential,whereas GQC showed -20 mV zeta potential values. All other systems showed an intermediate positive zeta potential value (Figure 69a) but less than +40 mV. The surface charge of GQC and GNR was changing when reacted together, indicating the change in surface properties because of the reaction between them.The TEM images of the final system GQC-GNR showed GQC embedded in the vicinity of GNR (Figure 69 b). The image also shows that the particles are not aggregating, and they kept their identity in the solution.

4.4.2. Conjugation of GQC-GNR with folic acid

GQC-GNR was functionalised with folic acid for tumor targeting and is confirmed by the characteristic peak at 291 nm (Figure70). It also retains the longitudinal peak of GNR at 707 nm (Insets of figure 70)

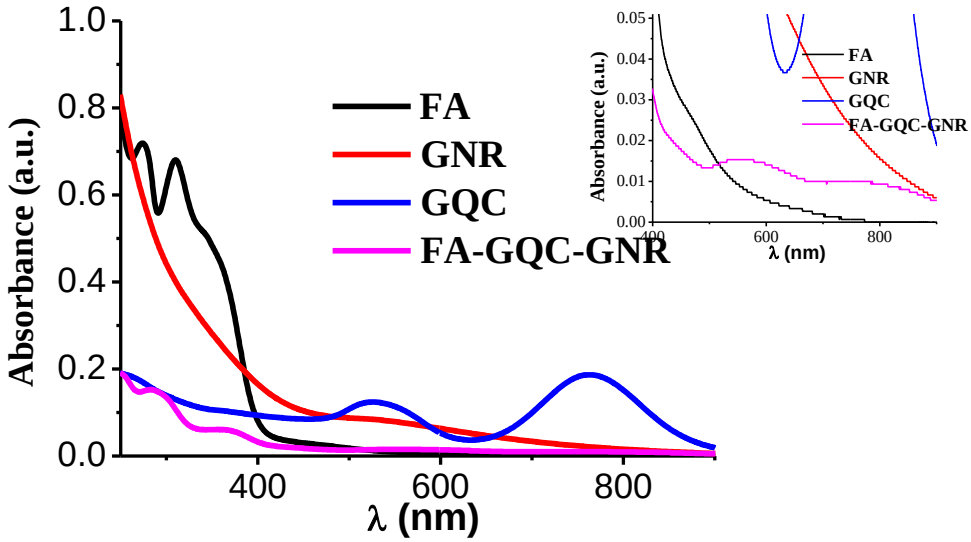

Figure 70: UV-visible spectra of FA, GNR, GQC and FA-GQC-GNR. Insets show the spectra at 400-900 regions.

4.4.3. *In vitro* imaging and therapy of GQC-GNR system

Cytotoxicity of GQC-GNR was evaluated in L929 and HeLa cells after 48 h of incubation (Figure 71). It showed concentration-dependent cytotoxicity with an IC_{50} value of 0.5 mg/mL. So,less than 0.5 mg/mL concentration of the hybrid particle is suitable for *in vitro* and *in vivo* applications.

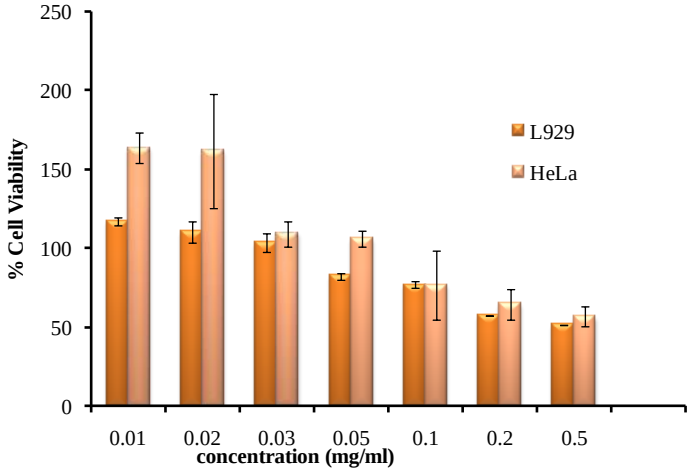

Figure 71: Cellular viability of GQC-GNR on incubation with L929 and HeLa cells.

Since GQC-GNR has high fluorescence quantum yield and cytocompatibility, it was evaluated for imaging efficacy after conjugating with folic acid in HeLa cell. The imaging property of the system was compared with that of its parent GQC and GNR.GQC-GNR has comparable fluorescence to that of GQC incubated cells (Figure 72), whereas GNR incubated cells didn'tshow any fluorescence, as expected.

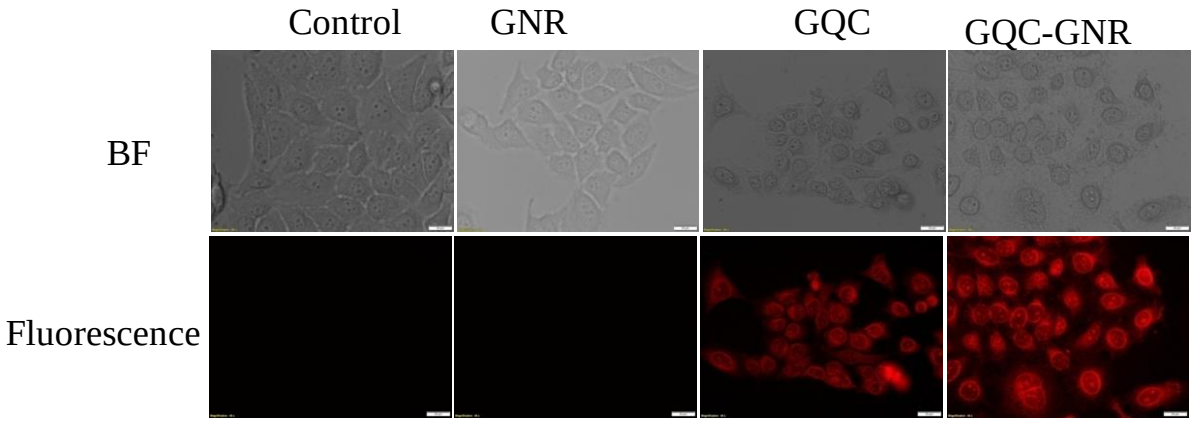

Figure 72: Fluorescence imaging of the HeLa cells using GNR, GQC, and GQC-GNR with control cells.

The therapeutic efficacy of GQC-GNR was evaluated by live/dead assay after incubating the material for 3h followed by irradiation of 808 nm laser. The laser-irradiated region showed more cell death compared to the non irradiated region (Figure 73).GQC-GNR showed a similar pattern of cell death as that of GNR, indicating that the particle retains the photothermal property of GNR. In the case of GQC, there is no effect on laser irradiation and is similar to that of control cells.

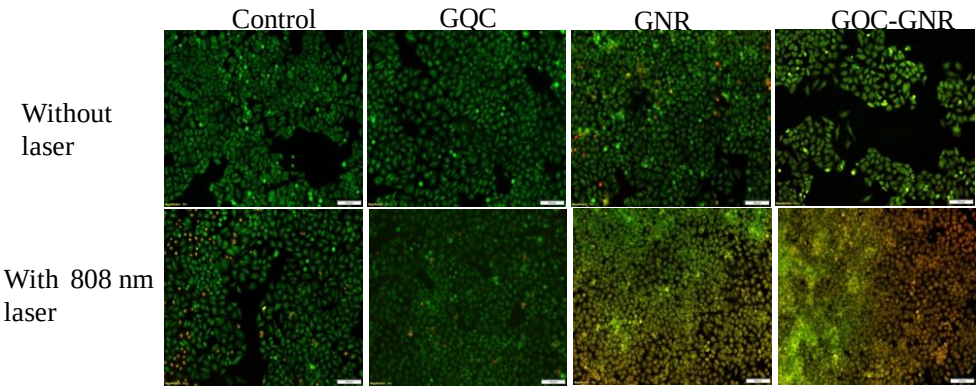

Figure 73: Live/ dead images of HeLa cells incubated with GQC, GNR and GQC-GNR with and without laser irradiation.

Therapy was quantitatively analysed using MTT assay after incubating GQC-GNR for 3h in HeLa cells (Figure 74). With laser irradiation,there was a concentration-dependent decrease in cellular viability

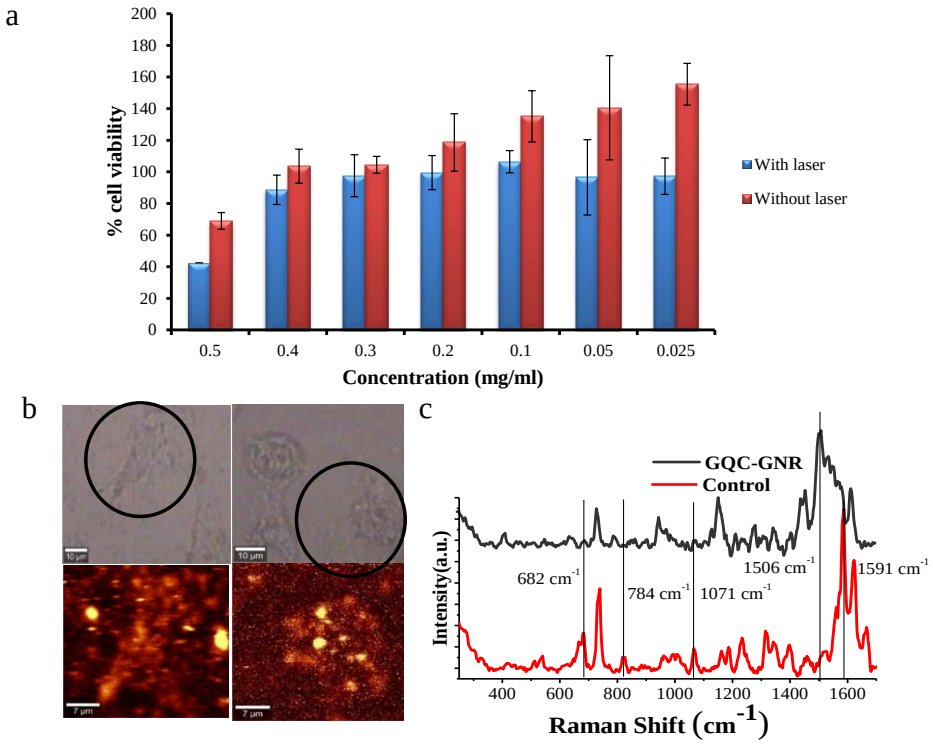

Figure 74: a) Cellular viability of HeLa cells after incubating with GQC-GNR with and without 808 nm laser irradiation, b) Raman imaging of HeLa cells with and without laser after 808 nm laser irradiation c) corresponding Raman spectra.

The cell death was again confirmed using Raman spectroscopy. The presence of GNR facilitated the enhancement of Raman signals.The decrease in the

peaks corresponding to the vibrations of proteins and DNA at 682 cm^{-1}, 784 cm^{-1}, 1071 cm $^{-1}$, 1506 $cm^{-1,}$ and increase in the peak of591 $cm^{-1}$is the indication of aromatic ring protein which is the sign of cell death upon laser irradiation.

4.4.4. *In vivo* imaging study of GQC-GNR system

The imaging property of the material was evaluated in tumor-bearing mice models by tail vein injection of folate conjugated GNR-GQC system. The control animals were injected with saline. The tumor-specific material uptake had happened, which showed higher fluorescence intensity at the tumor site as compared with controlanimal (Figure 75).

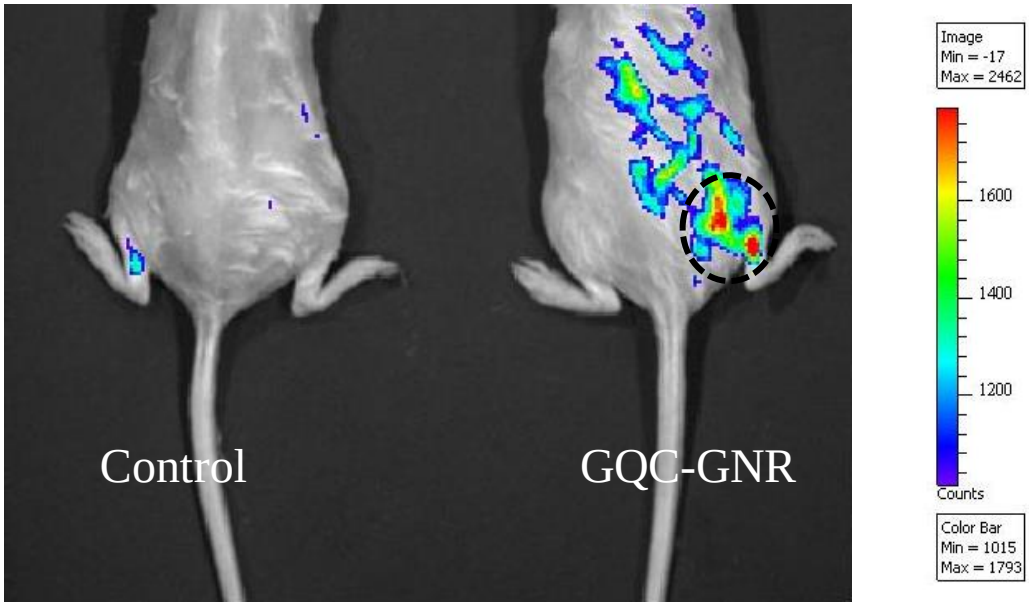

Figure 75: *In vivo* imaging of tumor-bearing mice by injecting GQC-GNR.

On sacrificing the animals, the biodistribution of the material in different organs was checked(Figure 76).The cancer targetability of GNR-GQC is clear from the highest fluorescence intensityobserved in theGNR-GQC injected animal's tumorregion compared with other organs and controlthe animal's organs.

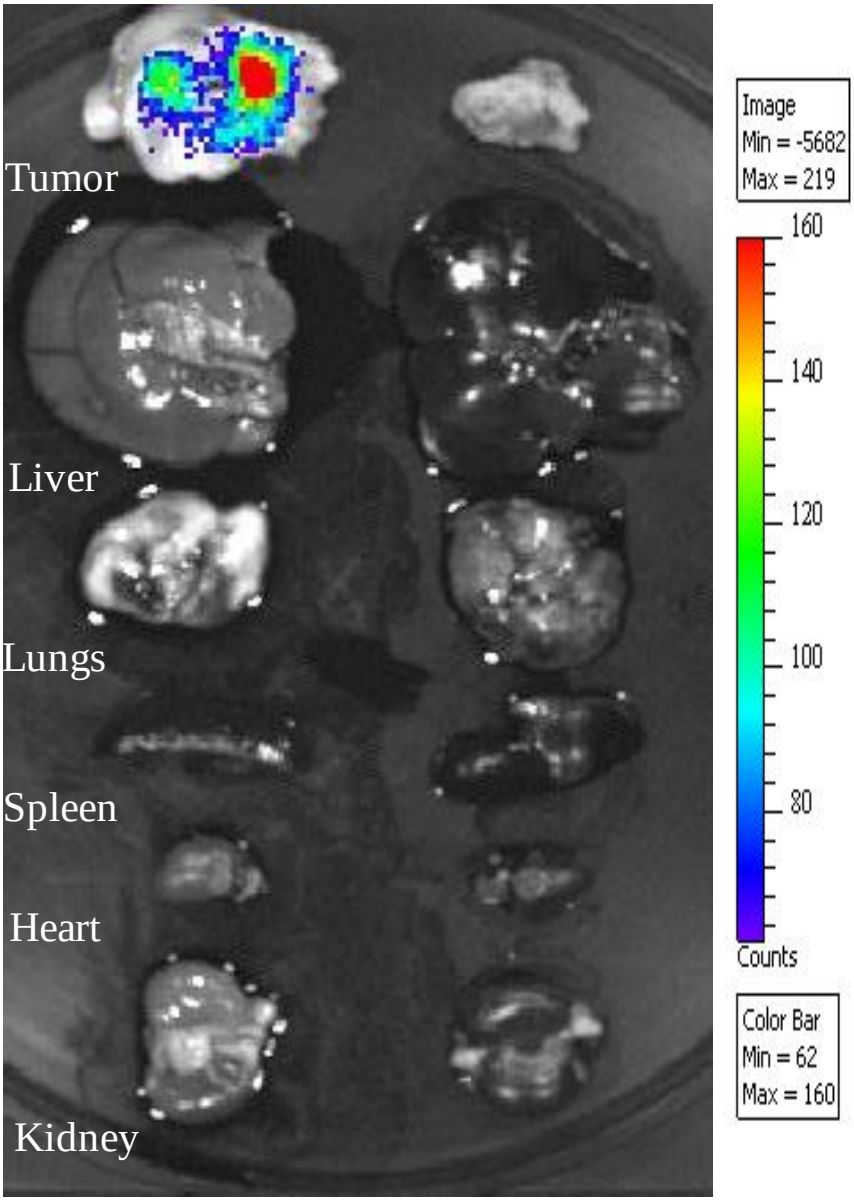

Figure 76: *Ex-vivo* image of material injected tumor animal and control.

Chapter 5

Discussions

This chapter discusses in detail the results of the thesis, as given in chapter 4.

5.1. *Quantum dot based multianalyte detection*

5.1.1. Cadmium selenide quantum dots for simultaneous detection of copper and creatinine

Quantum dots are fluorescent nanomaterials with a sizeless than 10 nm. One of the well studiedquantum dots is cadmium selenide (CdSe) with different capping agents. Here, we are making use of cysteine cadmium selenide quantum dots with green emission for the simultaneous detection of copper and creatinine. Copper and creatinine are two essential materials present in the body. Creatinine is the waste product of creatine, and copper is an essential element. The detection of these molecules is essential for the identification of different diseased conditions associated with it. For the dual-sensing, the green-emitting quantum dot was modified to have dual emission, blue and green.

5.1.1.1.Synthesis of cadmium selenide quantum dot (Qd) based sensor (PAQd) and characterisation

The sensor, PAQd, was synthesised using Qd, picric acid (PA) and 1-Ethyl-3-(3-dimethylaminopropyl)carbodiimide (EDC). Cysteine was used as a capping agent for Qddue to its ability to form complex with Cu like metals.From the UV-visible spectra, the absorption ofQd was observed at 515 nm. The absence of absorption peak at 693 nm (figure 11a),which usually appear in the presence of bulk cadmium selenide, confirms the formation of Qd of this material(Amiri, Fatahian &Mahmoudi 2013). Qd was then conjugated with picric acid considering its high affinity towards creat. Picric acid (PA) conjugation resulted in an additional peak in the absorbance spectra around 354 nm, with a shoulder peak around 403 nm (Figure 11a). These peaks, which are characteristics of PA confirmed the functionalisation of PA to Qd. In the case of PAQd, ablueshift from 515 nm to 502 nm was observed. It is due to the conjugation of the picric acid-EDC complex over Qd. Qd embedded in the organic

matrix has high energy and hence will be less stable as compared with Qd, making it susceptible to bind with the analytes to attain stability. The electron micrographs of PAQd confirmed the presence of organic matrix around Qd, and the size of the complexed system was 5.05±0.4 nm (Figure 11c). The bandgap of Qd shows a change from 2.41 to 2.47 eV from absorption spectra, indicating a change in size to lower range, as seen in electron micrographs.

The fluorescence property of Qd shows a green emission of around 543 nm upon excitation at 390 nm (Figure 12a). It was blue-shifted to 531 nm, upon picric acid functionalisation. This blue shift is due to the presence of EDC-picric acid complex over Qd, leading to an electron cloud density change around Qd, resulting in the shift in fluorescence peak. The change was also reflected in the absorption peak of Qd. However, the emission of PA in this region was very weak. The complex system Qd-EDC-picric acid (PAQd) showed another prominent emission peak at 446 nm upon 290 nm (Figure 12b) excitation, which is absent in Qd and picric acid. Thus, PAQd possesses two independent emissions at two different excitations, which are utilized for making the system as a multianalyte sensor. Both the emission peaks are having fluorescence lifetimes of 4 and 5 ns (Figure 12 c &d), which are suitable for imaging applications.

The absence of 2561 cm^{-1} peak of the S-H bond of cysteine inthe FT-IR spectrum (Figure 13) confirmed the formation of the S-M (metal) bond in Qd. The broad peak at 3425 $cm^{-1}$is due to the presence of intermolecular hydrogen bonding. The hydroxyl peak of PA at 3425 cm^{-1} disappears in PAQd due to the involvement of the hydroxyl group in the formation of the complex. The presence of aromatic ring was confirmed from the peaks around 3000 cm^{-1} and 600-900 cm^{-1} and nitro group from1334 cm^{-1} peak. Presence of the peak of carboxylate group at 1695 cm^{-1} indicateed its proximityto nitrogen atom confirming the complex formation with Qd. From the results of FT-IR, it can be confirmed that the hydroxyl group of picric acid is binding to the active site of Qd-EDC (Figure 13). The peak corresponding to carboxylic hydrogen is not observed due to the formation of intermolecular hydrogen bonding, which is in agreement with the FT-IR data in NMR data (Figure 14a).. In the NMR spectrum of PAQd, no acidic hydrogen is observed, indicating that the phenolic OH is participating in the reaction of sensor formation from Qd. The picric

acid conjugation is reflected by the presence of aromatic ring in the 8.86 ppm and 8.36 ppm. All other characteristics peaks of NH, CH, and CH_2 were observed with minor chemical shifts, indicative of different functionalisation of the system (Figure 14b).Zeta potential of Qd was -16.7 ±0.835mV (Figure 15). A decrease in the zeta potential value of Qd from -16.7 mV to -14.9 mV in PAQd suggests the functionalisation and the presence of nitro group and decrease in the carboxyl group at the surface.

Based on the above results, a mechanism for the formation of the sensor is proposed. EDC forms an electrostatic bond with O^- of cysteine. The carbodiimide group of EDC reacts with picric acid (PA), resulting in the formation of PAQd. The reaction leads to the formation of the Meisenheimer complex arising from the reaction of two equivalents of propylcarbodiimide with the substituted phenol. The result is the formation of a substituted s-triazinespirocyclohexadiene ring system(Al-kaysi, Creed & Valente 2004). The presence of 1695 cm^{-1} peak in the FT-IR spectrum of PAQd confirms the formation of the complex. Due to the presence of Qd, it loses zwitterionic nature by binding the positive part to negatively charged Qds. In scheme 1 the proposed structure for PAQd is depicted as obtained from experimental data.

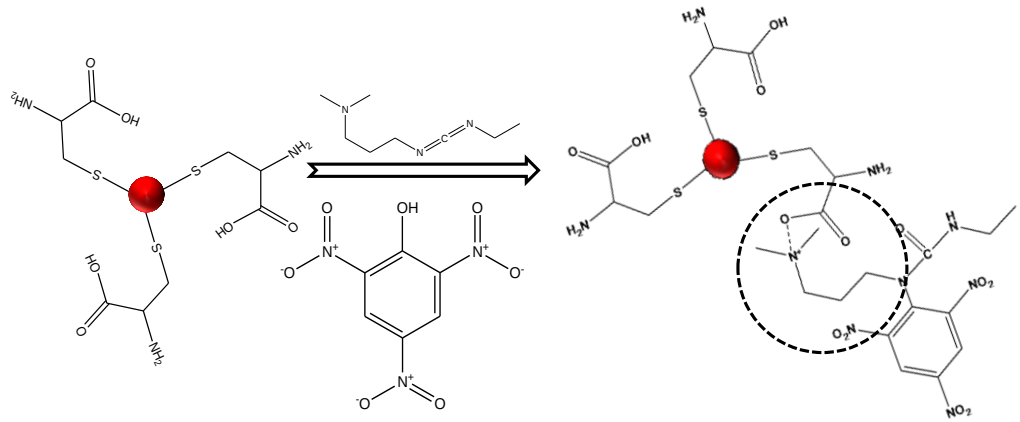

Scheme 1: Schematic representation of the formation of PAQd from Qd. Complex formation of PA, EDC, and Qd is represented in the circle.

5.1.1.2.Sensing of bioanalytes (copper and creatinine) using PAQd

The multianalyte sensing ability of PAQd was demonstrated by adding different known concentrations of Creatinine (Creat) and Cu to 1mg/ mL of the same. In the presence of Creat, emission peak c.a. 446 nm showed concentration-dependent enhancement when excited at 290 nm. The sensor (1mg/ mL PAQd) could detect the Creat level in the range from 3 nM to 0.003 mM in solution (figure 16a). Similarly, upon Cu addition to unimilli gram per milliliter of PAQd, the fluorescence quenching of the Qd peak at 531 nm was observed. The range of detection of copper ranged from 20.5 µM to 3.3 mM (figure 16b). The probe acts as a turn-on turn–off sensor for creatinine and copper, respectively. Figure 77is the diagrammatic representation of copper and creatinine detection using PAQd.

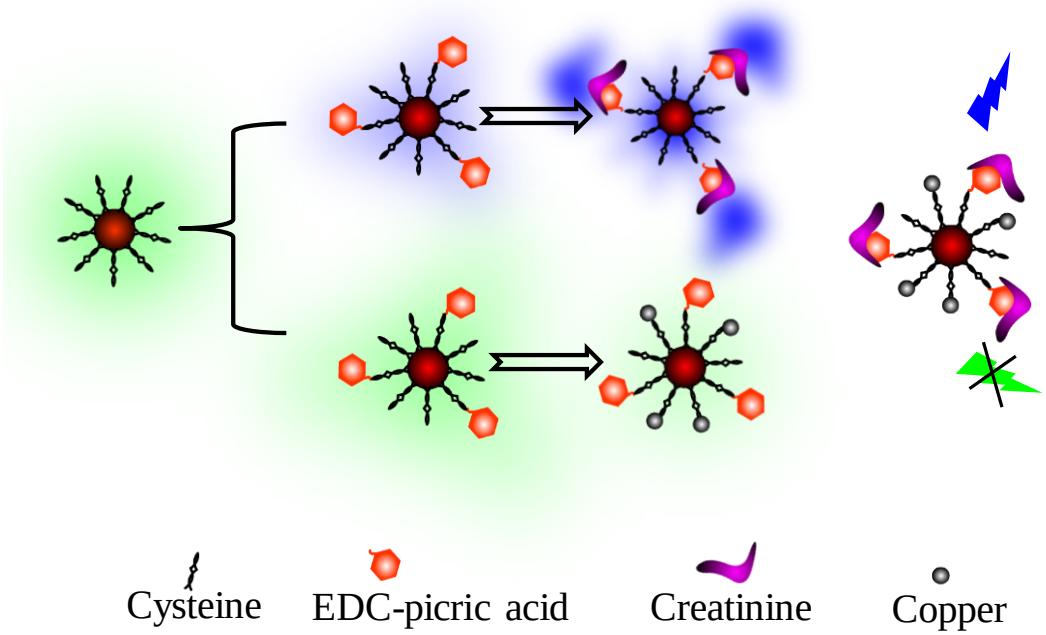

Figure 77: Cartoon of simultaneous detection of copper and creatinine.

The feasibility of using the sensor was checked in blood serum. For this, copper and creatinine were added to the human blood serum containing 0.01 mg/mL of sensor, and incubated for 2 minutes. The results of spectral analysis followed the pattern of the aqueous solution. As the concentration of creatinine increases, emission peak at

440 nm increased (Figure 17a), and as the concentration of Cu increases, emission spectra at 531 nm decreased (Figure 17b), proving the efficiency of the simultaneous determination of Cu and creatinine from human blood serum.

Efficacy of this probe was also checked in the cellular environment since both Creat and Cu are playing a vital role in metabolic activity and regulate and influence the blood analyte levels. Before performing the cellular study, the cytotoxicity of Qd and PAQd was assessed using MTT assay in two different cells viz. in L929 mouse fibroblast cells and MDA-MB-231carcinoma cell lines. The cells were viable for different concentrations upto 1 mg/mL for a long incubation period of 72 h (Figure 18a &b). Later, sensing efficacy of PAQd towards Creat and Cu was checked on the above two cells.

Because analytes of interest could be present both inside and outside the cells, extracellular and intracellular sensing efficacy of the sensor PAQd was checked. For intracellular Creat sensing, Creat was added to the cells and incubated for 30 minutes and washed with PBS, followed by incubation with PAQd for 3h. Similarly, intracellular Cu was also evaluated. Intracellular creat showed fluorescence enhancement in L929 and MDA-MB231 cells, while fluorescence quenching was observed for Cu. For extracellular Creat sensing, sensor PAQd was incubated for 3 h followed by Creat incubation for 3 minutes.

Similarly, the same procedure was used for extracellular sensing of copper. Here also enhancement and quenching of fluorescence were observed for creat and Cu, respectively, when tested in L929 cells. However, this was not observed with MDA-MB231 cells. The reason for this difference in two cell lines could be due to the difference in the environmental conditions of cancer cells and normal cells. When the analyte is incubated first, due to ion channel effect, analyte molecules get trapped into the cell. However, when the probe PAQd is added, the cancer cells block the binding site of the probe preventing it from attaching to the analyte molecule. This is due to the quick internalization of PAQd with the cancer cells, showing less intensity difference (Figure 19& Figure 20).

On confirming the efficiency of PAQd for simultaneous sensing of Creat and Cu, selectivity against other heavy metals and small molecules such as Pb, Mg, Mn, Ca, urea, and uric acid was checked. The changes in the emission peaks were found

to be specific for Creat and Cu (Figure 21a& b) without any interference from the presence of these metals or molecules. The simultaneous detection of the two analytes without interference from each other was also monitored with the help of zeta potential and selectivity study by checking the effect of creatinine onto the probe, which already contains copper, which is susceptible to aggregation (Figure 22a). The result revealed that there is no interference of Creat on copper detection and vice versa (results in detail are explained below while describing the mechanism).

Exploring the science behind the sensing, it is seen that the organic layer of PAQd disappears on addition of Creat (Figure 11c & Figure 22 b) because the organic part- picric acid-EDC complex reacts more strongly with creatinine, reducing the presence of organic layer, subsequently increasing the fluorescence output. The addition of Cu to PAQd increased the size of quantum dots (figure 22c). This increase in size is explained based on the decrease in the stability of quantum dots, leading to aggregation. Zeta potential value also supports this, as at high concentration of Cu, the value approaches zero (Figure 22a), and upon addition of creat to it, the value increases.It is due to the stabilization effect of the large complex molecule in the presence of creatinine, which prevents Qd from complete aggregation or destabilization.

The binding of PA to Qd makes the meta nitro group of picric acid active, leading to the binding of the methylene group of creatinine to picric acid. Upon addition of creat, the organic layer of the sensor disappears due to the binding of creatinine to Meisenheimer complex, weakening the bond from Qd. The presence of more electron-withdrawing groups causes a decrease in zeta potential value. Beyond the sensitive range of uM to mM, its zeta potential value remains the same, which indicates that only picric acid binding sites are bound to creatinine.

Cysteine molecules of Qd that have not taken part in the formation of the complex with EDC-PA contribute to the detection of Cu by forming a complex, cuprous bis-cysteine (Mehta, Kumar & Kailasa 2013) which is responsible for the fluorescence quenching. The complex formation and fluorescence quenching take place at physiological pH 7.4, and it is attributed to inner-filter effects, non-radiative recombination pathways, and electron transfer processes(Lou *et al.,* 2011; Mehta,

Kumar & Kailasa 2013b). The electron transfer effects are clear from the observation of size and zeta potential analysis. As the concentration of Cu increases, size of the probe also increases due to the strong binding of Cu to the cysteine leading to the clustering of Qd followed by an increase in the size. The zeta potential study shows that the value approaches zero upon the addition of a higher amount of Cu, but never reaches zero. This trend in zeta potential is because of the presence of picric acid EDC system over Qd. Scheme 2 represents the chemistry behind the simultaneous detection of PAQd.

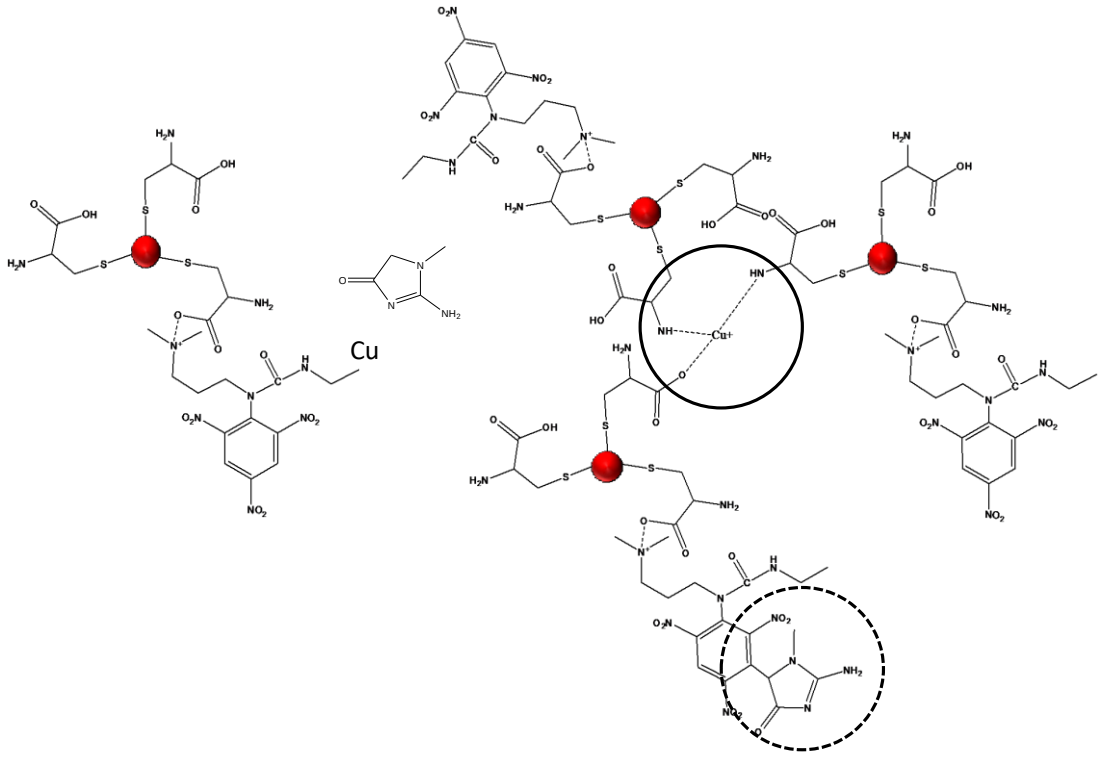

Scheme 2: Simultaneous detection of copper and creatinine by PAQd. Solid circle represents the complex formation of free cysteine of Qd and copper, and the dashed circle represents the bond formation of creatinine with picric acid present in PAQd.

5.1.2.Cadmium selenide quantum dots for the detection of lead and zinc

Cadmium selenide quantum dots are well studied material for its fluorescence properties. The previous section deals with quantum dot capped with cysteine, which is a comparatively small amino acid and which showed the emission in the blue and green regions. In this section, we explain a more biocompatible quantum dot with red emission. For this, we chose a higher molecular weight amino acid, glutathione,

for the synthesis of cadmium selenide quantum dots. Glutathione can bind with heavy metal ions, especially with the lead ion. This quantum dot is used for the detection of lead and zinc ions. Detection of these metals are very important in healthcare because zinc is an essential element in almost all organs and body functions, whereas lead is a toxic metal, the trace amount of which is toxic to the body.

5.1.2.1 . Synthesis and characterisation of glutathione capped cadmium selenide quantum dots (GQd)

Synthesised GQd solution, as per section 3.2.2 had a clear yellow color, which was separated by centrifugation using the isopropanol-water system. In the UV-visible spectrum, the absence of a peak at 693 nm indicates the absence of bulk cadmium selenide. A characteristics peak was observed at 431 nm, indicating the formation of quantum dots with a band gap of 2.88 eV (figure 23a). The size of the particles formed was in the range of quantum dots (Figure 23b),i.e., ~6 nm. At 420 nm excitation, it shows an intense red emission at 680 nm (Figure 23c). In the FT-IR spectrum, the absence of 2509 cm^{-1} peak (S-H) indicates the successful binding of glutathione to cadmium selenide dot through the metal sulphur bond. The presence of bands at 3249 cm^{-1} along with shoulder peak at 1626 cm^{-1} indicates carboxylic group and a peak at 1582 cm^{-1}corresponding to amino group in the FT-IR spectrum of GQd (figure 24). The structure of GQd (Scheme 3) was proposed as below. Here, the S-H group of glutathione directly reacts with metals and form metal thiol bonds.

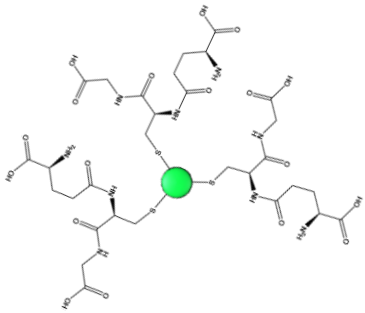

Scheme 3: Chemical structure of glutathione quantum dots (GQd). S-metal bonds formed results in the formation of GQd.

5.1.2.2.Detection of lead using GQd

1 mg/mL of GQd was added to a series of solutions with different concentrations of lead ions. As the concentration of lead ion increases, fluorescence emission get quenched. This quenching in fluorescence indicates that the lead ions attach to glutathione are interfering with the identity of GQd. In the presence of lead ions, glutathione strongly binds with another glutathione leading to the formation of dimers or trimers. More specifically, lead ions are acting as a chelator for glutathione; as a result, it loses the inherent fluorescence of GQd. It results in the fluorescence quenching by aggregation (figure 25).

It has high selectivity in comparison with other metals, amino acid, or biologically relevant molecules (figure 26). This indicates that lead ions itself havea unique capability to bind with glutathione than other molecules.

The mechanism of aggregation was again confirmed with the help of dynamic light scattering (DLS) analysis (figure 27). Zeta potential of the sensor and sensor with analytes were evaluated and found that as concentration increases, zeta potential decreases towards zero, implying loss of identity and stability of GQd. Moreover, size analysis using DLS showed an increase in size with respect to lead ion concentration. This again confirms the formation of aggregates when lead ions are introduced to the solution containingGQd. These aggregates increase the size of the GQd. From the experimental evidences, a chemical structure is proposed for the sensing of lead by GQd (Scheme 4) in which lead ions induces aggregation ofGQd.

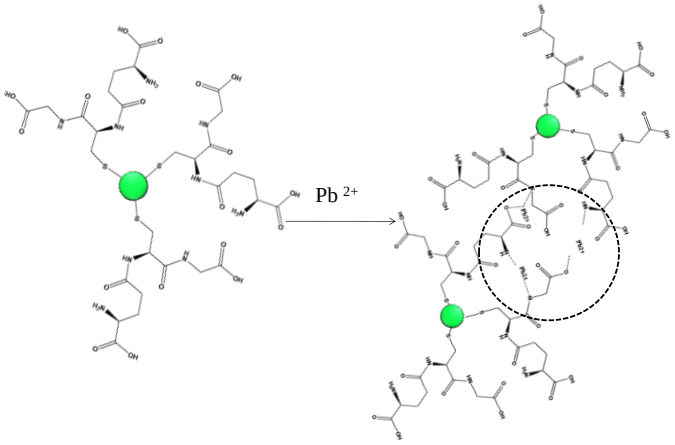

Scheme 4: Schematic representation of GQd binding with lead ions. The dotted circle represents the formation of the trimer of glutathione by lead ions.

5.1.2.3.Functionalisation of GQd with sulfamethoxazole

Sulfamethoxazole was functionalized to GQd for making it suitable for the detection of zinc ion. The UV-visible spectrum of the functionalised system showed a 255 nm peak, as mentioned in chapter 4 (figure28a). This peak corresponds to sulfamethoxazole, and the additional peak at 383 nm corresponds to the GQd peak. The blue shift observed from the original peak of 398 nm of GQd in the UV-visible spectrum attributes to the decrease in the size, which is confirmed by transmission electron microscopic images (figure 28b). A bathochromic shift was observed in comparison with GQd in the fluorescence spectrum, i.e., 680 nm emission shifted to 586 nm (figure 28c). It can be discussed as the sulfamethoxazole participation in the stabilization of GQdmaking the system slightly smaller. The formation of SMGQd can be schematically represented as follows (Scheme 5). FT-IR spectrum of SMGQd (figure 29) showed peak at 1121 $cm^{-1,}$ indicating the presence of S=O peak of sulfamethoxazole. 1458 cm^{-1}peak indicating the presence of an amide group, confirming the binding of sulfamethoxazole to GQd.

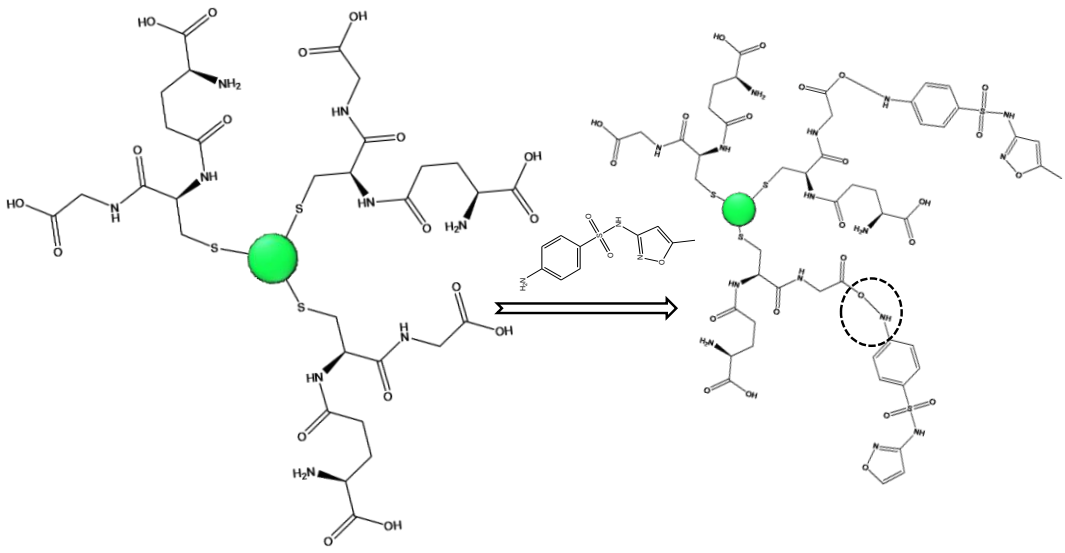

Scheme 5: Representation of synthesis of SMGQd from GQd. Bond with GQd and sulfamethoxazole is shown in the circle.

5.1.2.4.Detection of zinc using SMGQd

1 mg/mL of SMGQd was added to the aqueous solution containing different concentrations of zinc, and the fluorescence intensity of the solutions was noted. As the concentration of zinc increases, fluorescence intensity also increases (figure 30). Here, sulfamethoxazole is binding to zinc ion rather than to GQd.

Zinc ions form a co-ordinate bond with sulfamethoxazole. The fluorescence intensity change of SMGQd on the addition of other analytes such as cadmium, lead, calcium, manganese, iron, etc. did not show any change in the fluorescence intensity except with cadmium and lead. But the percentage of increment is less for both so that its presence will not interfere with the results of zinc ions. Moreover, the presence of cadmium is not expected in the biological systems; the detection of zinc will not be affected by the presence of cadmium in such systems. Among other analytes, zinc ions have the highest selectivity (figure 31). This sensor has sensitivity ranges from nM to mM.

The zeta potential analysis showed that as the concentration of zinc increases, zeta potential value increases, which attribute to the fact that the system becomes more stable when zinc ion binds to SMGQd. A small decrease in the size was observed when the concentration of zinc ion is increased. It is due to the formation co-ordination bond of SMGQd with zinc ion, which weakens the covalent bonding between sulfamethoxazole and glutathione (figure 32). This change in size indicates that the presence of zinc ion does not affect the existence of GQd. Instead, it affects the identity of GQd with the co-ordination bond formed between zinc and sulfamethoxazole, which leads to charge transfer increasing in fluorescence intensity.

The mechanism of detection of zinc ions can be schematically represented as follows (scheme 6). In the scheme, the co-ordinate bond between zinc ions and the S=O-N group of sulfamethoxazole is represented.

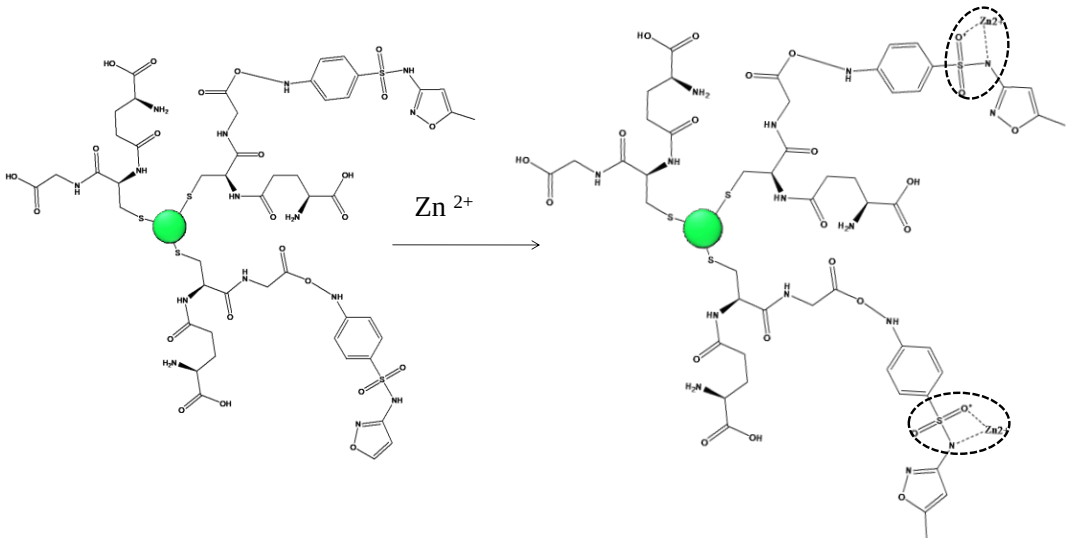

Scheme 6: Detection of zinc using SMGQd. Binding of the zinc ions to SMGQd is represented with circle.

In conclusion, the glutathione quantum dot is designed with appropriate surface ligands to facilitate the detection of lead and zinc using the same basic nanosystem. Pictorial representation of same is given below (Figure 78)

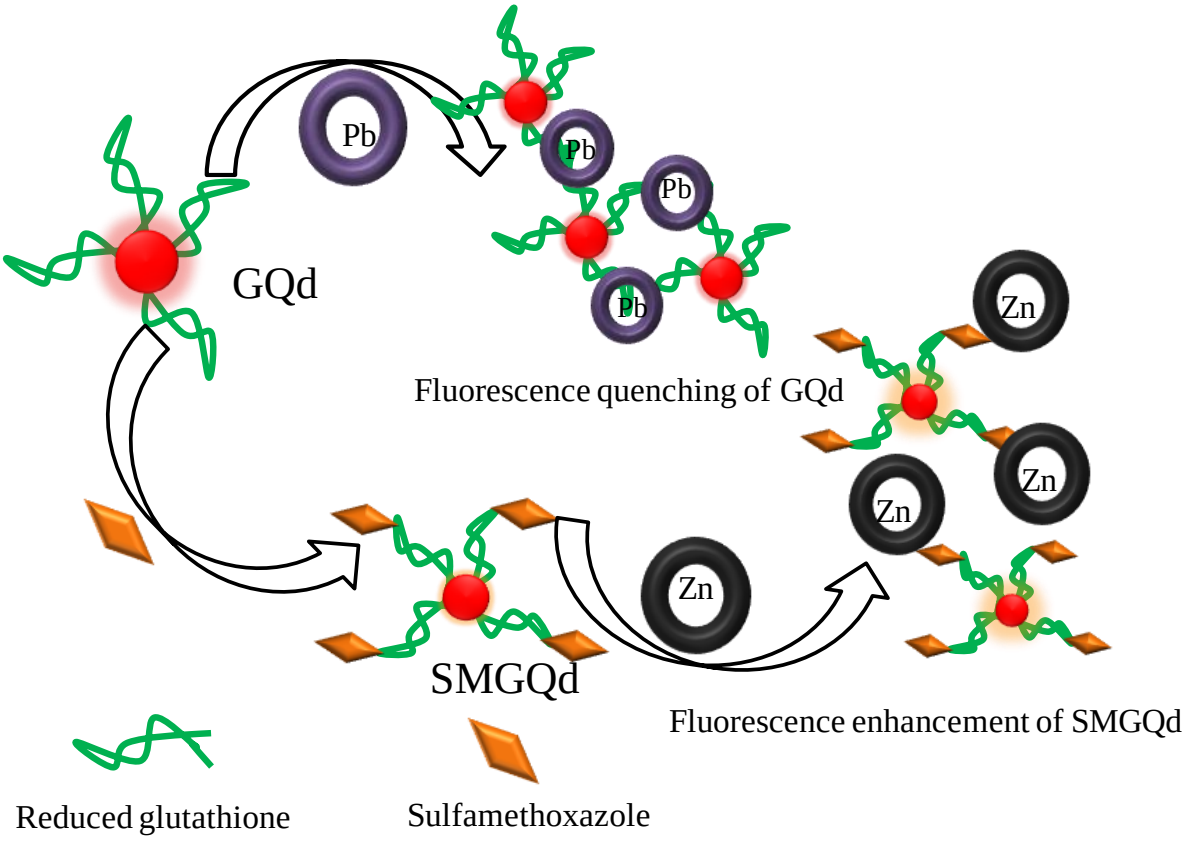

Figure 78: Schematic representation shows the detection of zinc and lead using GQd and SMGQd.

5.2. Cysteine gold cluster for dopamine detection and imaging

5.2.1. Synthesis and characterisation of cysteine cluster

Generally, the formation of the gold cluster has been reported based on the stabilization of large molecules. Cysteine is an amino acid that contains one carboxylic acid, amino group, and thio group in it, and the formation of cysteine stabilised gold cluster was challenging and is not reported. The synthesis of a cysteine cluster and its application for biosensing is explained here. The reactants used in the synthesis were chloroauric acid, cysteine, sodium borohydride, and sodium hydroxide. By varying the concentrations of these reactants, the synthesis was optimized. The effect of change in pH from acidic to basic on cluster formation was also noted.

UV-visible spectra of different batches (figure 33) of synthesized clusters were recorded. Changing the concentration of cysteine molecule showed drastic variations in the spectra. It is due to the formation of different gold nanostructures from clusters to anisotropic models (figure 33a). Similarly, change in the concentration of chloroauric acid also leads to the formation of different shapes of materials (figure 33 b). It is because, as the concentration of cysteine and chloroauric acid varies in the presence of a reducing agent, there is an increasing tendency to grow to larger nanoparticles with different shapes. Both the reactants directly influence the growth of the nanoparticle.

When the concentration of sodium borohydride and sodium hydroxide are varied in an increment of 0.02 mL, it is noted that the valley of the absorption spectrum varies, an indication of the difference in the size of the cluster formation (figure 33c). This is as expected whena change in the concentration of sodium borohydride, which is responsible for the reduction of goldis varied, without altering the concentration of other reactants. It leads to the variation in the cluster size and number, but not the shape of the system. If the concentration of sodium borohydride is increased to more than double, aggregation of the gold system takes place due to the complete reduction of gold. Similarly, the concentration of sodium hydroxide

provides a basic medium for cluster formation, and a variation in its concentration affects the size and number of clusters, not the shape.

From the above observations, it is inferred that chloroauric acid and cysteine with a ratio of 2:1 results in the formation of a cluster with NIR emission in basic pH by reduction with sodium borohydride. It shows emission at 606 nm (figure 34b). The occurrence of emission in the gold cluster is due to the intra–inter electron transfer between gold and cysteine molecules. From the FT-IR spectrum, it was clear that almost all the functional groups of cysteine are absent after the cluster formation (figure 35). It is because the cysteine used for the reaction is very less(1mM), and to form a cluster, it acts as a multidentate ligand to gold. All the functional groups of the cysteine hold gold atoms to form a gold cluster. From the TEM images, they are in the subnano size, and laser fragmented MALDI-MS data indicates the purity of the system (figure 36). Overall, a well-dispersed cysteine gold cluster having NIR emission was synthesized and is used as a base material for dopamine sensing.

5.2.2. Sensing of dopamine using cysteine gold cluster

Dopamine is a catecholamine mainly found in the neurons, other than in blood and urine. It has very important role in the case of Parkinson's disease and other neurological conditions. Cysteine gold cluster was used for the detection of dopamine, due to the high affinity of dopamine to cysteine molecules. The emission of the cluster showed a concentration-dependent increase with dopamine (figure37). Dopamine molecule tends to form quinine structure and also polymerise to form fluorescent structures. Likewise, with the addition of dopamine to the gold cluster, it binds to both bare gold surface and to the neighboring cysteine (a competition), resulting in the enhancement of fluorescence intensity of cluster due to surface stabilization by large polymeric like molecules. Schematic representation of dopamine detection is shown below (scheme 7). Cysteine gold cluster was highly selective towards dopamine in comparison with other analytes (urea, uric acid, sodium borohydride, ascorbic acid).

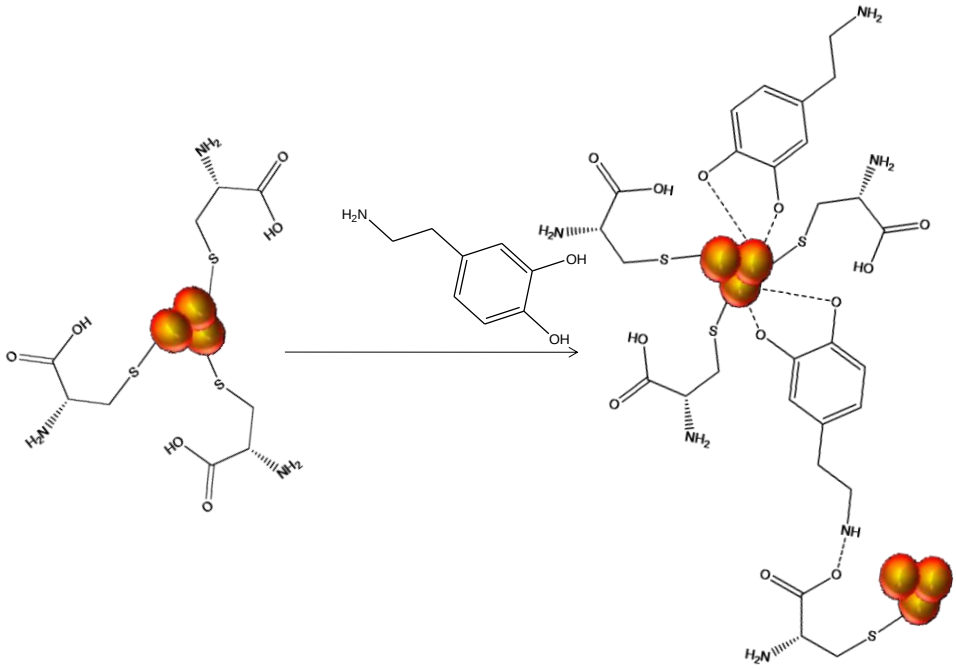

Scheme 7: Detection of dopamine using cysteine capped gold cluster.

Zeta potential analysis of gold cluster and gold cluster incubated with dopamine indicate that as the concentration of dopamine increases, zeta potential decreases (figure 39). Another observation was that as concentration increases, the size of the cluster decreases. This is because dopamine molecules showed a competitive binding with cysteine as well as core gold atoms. In the presence of dopamine, the cysteine molecule present on the gold cluster form fluorescent self chains leading to an increase in fluorescence emission, since the ratio of cysteine in the composition is less. Cysteine cluster is also used to detect dopamine concentration in C6 glial cells. The intensity plot describes that the increase in the concentration of dopamine increases the fluorescence intensity (figure 38).

5.2.3. *In vitro* imaging using cysteine gold cluster

The red emission at 653 nm of the cysteine gold cluster is utilized for cellular imaging applications. The bare gold cluster was incubated with L929 and HeLa cells for 3 h to check the cytocompatibility (figure 40). 12 mg/mL of AuC showed more than 60% cell viability indicating its high cytocompatibility. Imaging property of the system was observed in both L929 and HeLa cells after 3 h of incubation (Figure

41). Fluorescence signals indicate the passive uptake of material by the cells due to its smaller size.

Thus, the cysteine gold cluster is a good candidate for dopamine detection and cellular imaging and has proven to be a very good candidate for biomedical applications. It is diagrammatically represented below (figure 79).

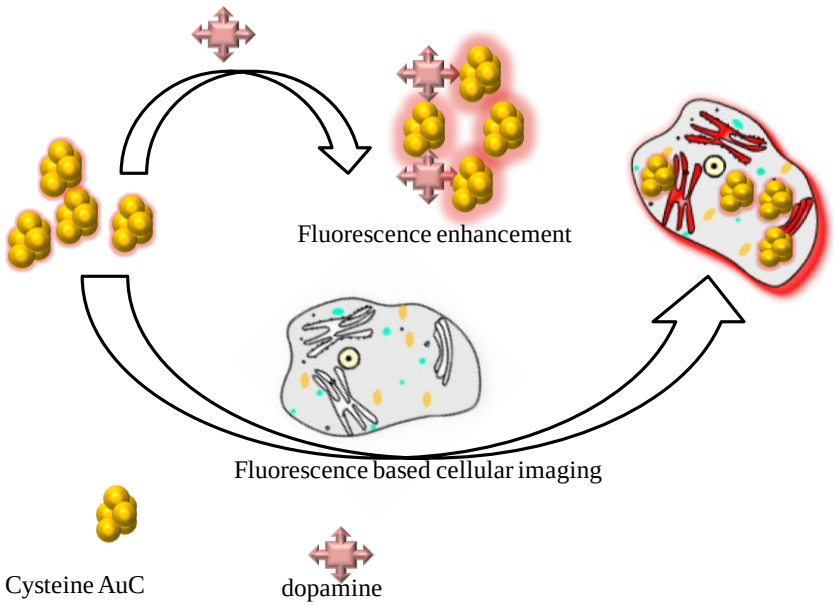

Figure 79: *In vitro* imaging and dopamine detection using AuC.

5.3. Fluorescent multifunctional gold nanorod nanomaterial for imaging and therapy

5.3.1. Gold nanorod-MTX nanomaterial for *in vitro* cancer imaging and therapy

5.3.1.1. *Synthesis and characterisation of gold nanorod-MTX*

Gold Nanorod (GNR) was synthesised by seed mediated growth method as described elsewhere, using CTAB as a capping agent (C. V Durgadas *et al.*, 2011; Nikoobakht & El-sayed 2003). Uniform sized GNRs were obtained after removing excess CTAB by centrifugation. The absorption spectrum shows typical absorption bands of GNR due to longitudinal oscillation of electrons at 786 nm and transverse plasmon absorption band at 534 nm (figure 42a). The longitudinal absorption band in the NIR region is the main attraction to use GNR as an excellent candidate for PTT.

The surface of GNR was then modified with thio-amino PEG to reduce its toxicity(Kaneti*et al.*, 2015). A slightly blue-shifted absorption band at 770 nm

compared to 786 nm of GNR is an indication of the presence of PEG over GNR. No shift in the transverse absorption peak was observed after PEG modification (figure 42a). PEG-modified GNR, PGNR was further functionalized with folic acid using EDC/NHS coupling. The resultant system, FPGNR, has absorption bands at 371, 283 and 255 nm along with the longitudinal and transverse plasmonic absorption bands of GNR indicating the presence of folic acid in FPGNR (figure 42a).

Mitoxantrone (MTX), a cancer drug, was encapsulated in FPGNR for simultaneous chemo and photothermal therapy and also for fluorescence imaging. The absorption spectrum of the final system, MTX@FPGNR also shows both the absorption bands of GNR (figure 42a), with a slight shift in the transverse oscillation-band, due to the presence of MTX. The longitudinal and transverse absorption bands of MTX@FPGNR and GNR have almost equal intensity. Moreover, the shoulder peak around 594 nm observed in all other constructs vanishes in MTX@FPGNR. It might be due to the overlapping of the absorption frequency of MTX with FPGNR. This further confirms the encapsulation of the drug. The peaks at 283 and 255 nm indicate the presence of both folic acid and MTX in the final system. Shoulder peak at 371 nm can be due to the presence of folic acid (figure 42a) in MTX@FPGNR. The schematic representation of the synthesis of MTX@FPGNR is shown in scheme 8(Nair, Santhakumar & Jayasree 2018).

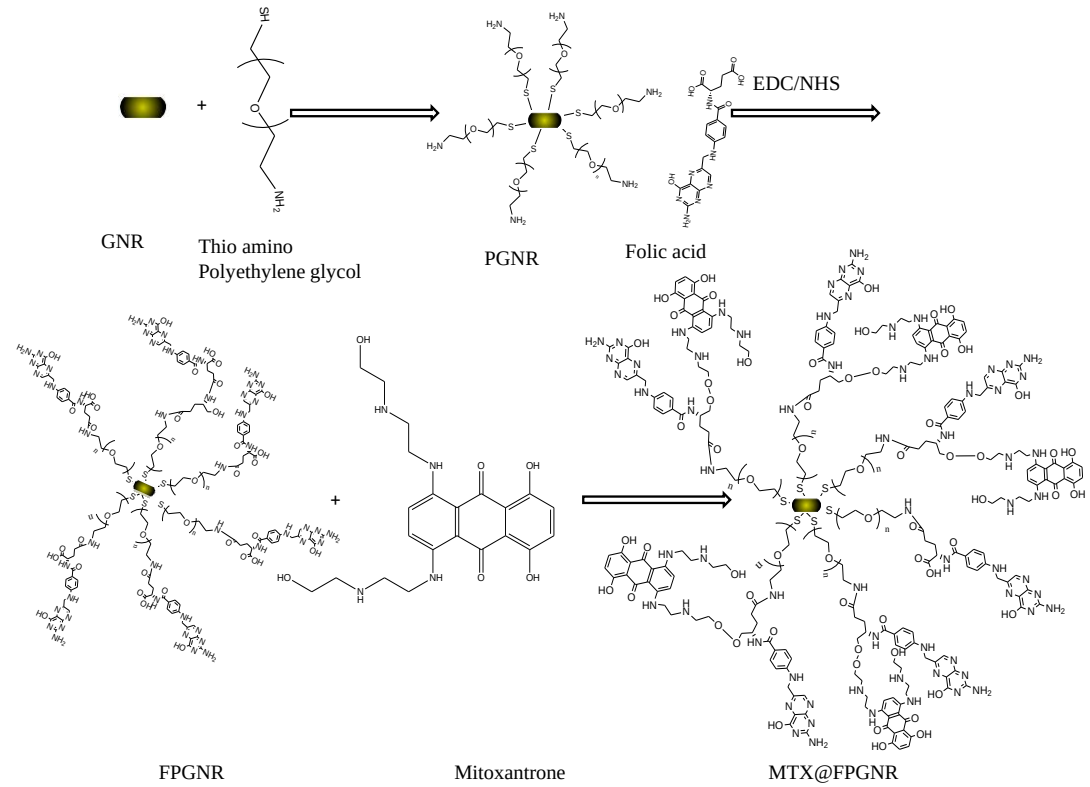

Scheme 8: Schematic representation on the synthesis of MTX@FPGNR at different stages.

Modifications of GNR at different stages were also confirmed using FT-IR spectroscopy (figure 43). The initial system, GNR, showed the characteristic vibrations of trimethyl ammonium ion of CTAB around 929, 1000, 1061 cm^{-1} (figure 43). Upon surface modification with PEG, additional peaks corresponding to primary amino groups are observed in the range 3269-3196 cm^{-1}. 2892 cm^{-1} peak is assigned to CH stretching vibrations. Vibrational bands of amino groups are also visible at 1597, 1122, and 667 cm^{-1}. Peaks corresponding to CTAB are absent in PGNR, which proves the complete elimination of CTAB and the successful covering of amino PEG over GNR. The peak at 2598 cm^{-1} is absent in PGNR, which indicates the bonding of thiol group to GNR. FT-IR spectrum of FPGNR showedpeaks corresponding to amino group and amide groups at 3391 and 653 cm^{-1} , and 1606 and 1119 cm^{-1} respectively. 891 cm^{-1}peak indicate the presence of aromatic groups. The peaks corresponding to mitoxantrone are prominent in MTX@FPGNR. The peak at 3268 cm^{-1} is due to the vibrations of the phenolic OH group, whereas 2880 and 2326 cm^{-1} peaks are due to CH and C=C vibrations. The presence of peaks at 1739 and 1373

cm^{-1} indicate the vibrations of ester groups formed by the bonding of MTX to FPGNR. Peaks at 1655 and 860 cm^{-1} are assigned to the vibrations of the amide group and aromatic ring, respectively. The peak at 1556 cm^{-1} is assigned to the vibrations of the amine group. From these it was clear that the ester bond formation in MTX@FPGNR with MTX and FPGNR.

The fluorescence spectroscopic study shows a weak emission profile for PGNR and FPGNR in the NIR region at 600 nm excitation. This is attributed to the fluorescence of gold nanorod and enhanced in the presence of PEG and folic acid. Two strong emission peaks at 668 and 711 nm are available for the final GNR construct, MTX@FPGNR. The drug MTX has two prominent emission peaks at 679 and 714 nm (figure 42b). In this case, the fluorescence of the drug is retained even in the presence of GNR, unlike in the case of many other studies where the fluorescence of the fluorophores in the proximity of GNR gets quenched(Jang *et al.*, 2011c). The reason behind the retaining of fluorescence in this study is due to the presence of polymer covering over GNR, which separates the fluorophore (MTX) 10 nm apart and prevents quenching of fluorescence of MTX. The strong NIR emission of the final system makes it suitable for bioimaging. Electron microscopic analysis reveals the formation of anisotropic GNR with an average aspect ratio of 3.2±0.18. Further functionalisation did not alter the aspect ratio considerably (figure 42c) and hence the heat generation property. This is confirmed by monitoring the temperature increase of the final system in aqueous solution with an NIR laser irradiation. Heat generation of more than 48^0C was achieved with MTX@FPGNR within 5 minutes of laser irradiation while GNR alone generated heat of the order of 60^0C (figure44). When the temperature above 40^0C is sufficient for effective photothermal therapy, the effect of surface functionalisation is attributed to the observed decreases in the heat generation.

Zeta potential at every stages of functionalisation was monitored to know more about the behavior of particles. When the first system, GNR had a zeta potential of +14.6 mV, zeta potential of PGNR is decreased to +7.19 mV, which could be due to the presence of NH_2 in the amino PEG. Further, conjugation with folic acid decreased the zeta potential to -5.86 mV, due to the presence of more –

COOH and NH_2 groups. Finally, MTX@FPGNR at normal pH gives a zeta potential of -1.06 which in acidic pH changes to 4.93 mV (figure45).

Raman spectrum of the drug, MTX in aqueous medium did not show any prominent peaks, due to the interference of high fluorescence from the drug. However, the Raman peaks are well defined in the case of MTX@FPGNR because the gold construct act as a SERS substrate to enhances the Raman signals multifold. Raman spectrum of MTX@FPGNR shows a prominent peak at 1300 cm^{-1} which is assigned to the ring stretching mode coupled with C-O bond vibrations (figure 42d). Strong peak at 464 cm^{-1} indicates the presence of C-N in the aromatic ring and C-C-O bonds present in folic acid and MTX(Nabiev*et al.,* 1995).

With laser irradiation, a controlled release of the drug followed by increase in the fluorescence from the drug is expected due to unique design of the final system. Drug release followed by increase in the fluorescence intensity was studied at different time period with and without laser irradiation (figure 46). The drug release study revealed that at all pH, the material is stable upto 8h. A very less amount of drug release was observed in acidic pH without laser irradiation, neutral pH with and without laser irradiation. But the combined effect of acidic environment and laser irradiation induces spontaneous drug release. This finding could be used for cancer treatment where the pH is acidic with controlled laser irradiation. At normal pH, no drug release was observed even after 24h indicating the stability of material without laser irradiation. The drug release mechanism is explained as follows: when the alcoholic side chains of MTX molecule reacts with the acid groups of folic acid, ester bonds are formed. This is confirmed in FTIR spectrum. In acidic pH and the high temperature by laser irradiation induces ester hydrolysis leading to drug release followed by the increase in fluorescence intensity. Thus the system works on the principle of laser induced drug release.

5.3.1.2 In vitro studies

To evaluate the cytocompatibility, the different gold constructs were tested for its long term cellular cytotoxicity in normal L929 fibroblast cell line, using standard MTT assay (figure 47). At 24 h of incubation, GNR showed less cellular viability which may be due to the presence of toxic CTAB. The functionalisation of GNR with PEG and folic acid reduced the toxicity showing a cell viability of more

than 95% even at a higher concentration of 2 mg/mL proving its suitability to use under cellular environment, safely. On encapsulation of MTX drug in FPGNR, the cell compatibility was retained in L929 fibroblast cells. This result indicates that the drug is not released under normal conditions without the laser stimulation and is stable inside the cell. Overall, the results suggest that MTX@FPGNR can serve as a biocompatible material for the combined photothermal-chemo therapy for cancer, without affecting the neighboring normal cells.

The targeting of the GNR construct to the cancer cells is achieved by folic acid conjugation. Different cell lines with varying folate receptor expression were chosen to prove this. It is reported that the normal L929 fibroblast cells have very low folate receptor expression compared to the cancerous cell lines (Bhattacharya *et al.,* 2011). Between the two cancer cells considered, rat brain glioma cells (C6) have moderate folate receptor expression than human cervical cancer cells (HeLa)(Saul *et al.,* 2003). The cell uptake study was performed using these three cell lines with an incubation period of 6h (figure 48). The results show that receptor mediated uptake of MTX@FPGNR is maximum in HeLa cells where the folate receptor expression is highest followed by C6 glioma cells and least uptake is observed in L929 cells. From the red fluorescence of the material and the nucleus specific Hoechst staining, it is clear that the construct is concentrated mostly in the cytoplasm than in the nucleus. The result of the cell uptake study gives a clear indication of the folate receptor over expressed cancer cell targeting efficiency of MTX@FPGNR.

On achieving excellent cancer targeting ability, MTX@FPGNR was further tested for its drug release efficacy in both the cancer cells, with phothermal triggering. The observed increase of red fluorescence is a clear indication of the drug release upon laser irradiation compared to non-irradiated cells (figure 49a). Both HeLa and C6 cells showed increase in fluorescence during drug release in accordance with the material uptake efficiency, which reflected the difference in folate receptor expression level. The drug release study was also confirmed with Raman spectral analysis where the presence of GNR contributed to SERS activity and thus was instrumental in getting Raman signals even in the presence of fluorescent MTX (figure49e-g). For this, cells incubated with the final system for 6 h, with and without laser irradiation were monitored. Due to the intense fluorescence

of the released drug, no Raman peaks could be identified from the laser irradiated cells where as the material incubated cells without laser showed distinct Raman peaks (figure49g). The Raman peaks of GNR construct in the cells were assigned in accordance with that of the same in aqueous solution. The most prominent peak observed at 1300 cm^{-1} in the Raman spectrum of MTX@FPGNR in solution is absent in cells. This is because in the acidic environment of cancer cells, the ring stretching modes of MTX@FPGNR are restricted. HeLa cells show Raman peak at 1104 cm^{-1} due to the C-O and C-N vibrations. Peaks at 556 and 994 $cm^{-1}$are assigned to the ring deformation and C-C vibrations of the construct. 463 cm^{-1} peak represents C-N vibration of the drug, MTX. Less intense Raman peaks of the cells were also observed in the spectrum. Similar trends were also seen in C6 cells.

However, in HeLa cells the less intense peaks corresponding to the signature of cells are prominent than in the C6 cells. This may be due to the lack of sufficient amount of GNR substrate inside the cells to support SERS, as the cell uptake efficiency was less in the case of C6. The Raman spectra of laser irradiated cells appear to be similar to that of the drug, MTX in solution where no peaks are identified. This is due to the switching ‘on’ of strong fluorescence from the released drug upon laser irradiation.

Owing to its strong NIR absorbance and high heat generation efficiency in solution, MTX@FPGNR was further studiedfor its combined photothermal and chemotherapy potential in cancer cells. Live/dead assay was performed in the cancerous cells, HeLa and C6 after laser irradiation with 808 nm, using acrydine orange/ethidium bromide staining for qualitative finding and MTT assay for quantitative assessment (figure 50). For the quantitative assay, cells were treated with MTT. MTX@FPGNR incubated cells along with laser irradiation showed considerable cell death in comparison with non irradiated control cells (figure 50). The results showed that MTX@FPGNR induced more significant therapeutic effect in HeLa cells than in the C6 cells, because of the high expression of folate receptors in HeLa cells. This is in accordance with qualitative result of live dead assay (figure 50a). The efficacy of combined therapy was evaluated with chemotherapy of MTX alone. Extensive cell death was observed in GNR construct incubated cells with laser irradiation, than the MTX alone treated cells (figure 50b). The treatment efficacy of

MTX@FPGNR was further compared with GNR, PGNR and FPGNR. MTT assay was carried out using C6 and HeLa cells after 6h of incubation of different GNR systems at different concentrations, after laser irradiation (figure 50c &d). From this, it is clear that the treatment efficacy is higher in HeLa cells compared to C6 cells. These results suggest that the combined photothermal and chemotherapy induced by MTX@FPGNR led to irreversible and serious damage to HeLa cells which has high expression of folate receptor. More detailed study is necessary in order to examine the mechanism of cell death, eg., apoptosis.

To summarise, the construct MTX@FPGNR possesses several unique properties and functionalities, such as long term stability, controlled drug release capability with laser irradiation, excellent heat generation capacity, cancer-targeting propery and biocompatibility, which makes it an ideal photothermal cum chemotherapy agent for folate receptor overexpressed cancer cells. The study is schematically represented in figure 80 below (Nair, Santhakumar & Jayasree 2018).

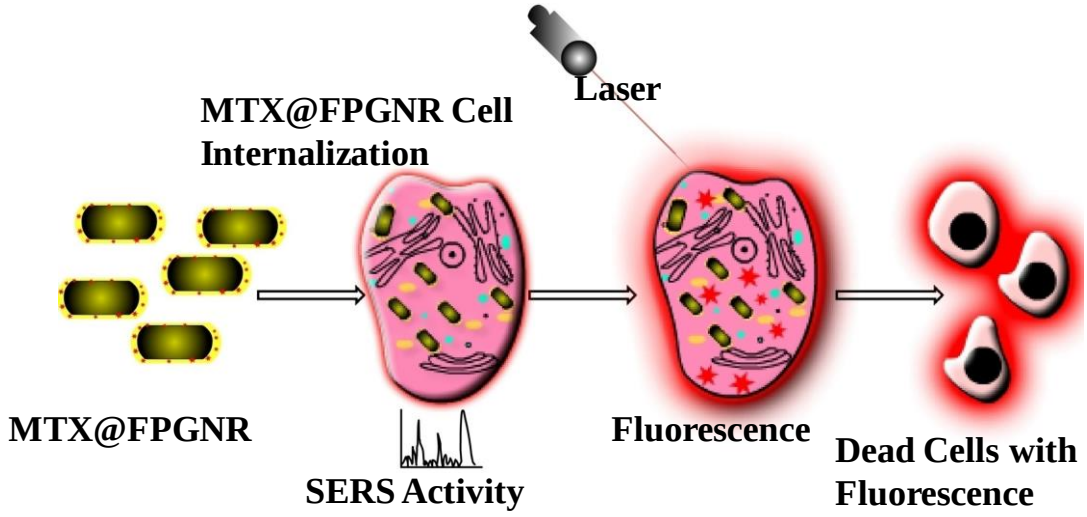

Figure 80: Schematic representation of interaction of cancer cell with MTX@FPGNR.

5.3.2. Gold nanorod-PPIX nanomaterial for cancer imaging and therapy

5.3.2.1.Synthesis and characterisation of gold nanrod-PPIX

The synthesized GNR has two characteristic plasmon absorptions at 523 and 743 nm due to transverse and longitudinal surface plasmon resonance (figure 51). On replacing CTAB with GSH, GSH@GNR retains both the plasmon peaks. After PPIX conjugation, P@GNR shows the characteristic soret band of PS at 376 nm. A slight blue shift of the Q bands (536, 585 and 640 nm) is observed in P@GNR compared to pure PPIX (figure52). The observed lateral assembly of P@GNR (figure 44c) accounts for the blue shift of the longitudinal plasmon peak. Additional absorbance peaks at 284 and 254 nm are observed on folic acid conjugation in F@PGNR. In the case of P@GNR and F@PGNR, less intense broad shoulder peaks observed in the range 450 to 550 nm are due to the transverse surface plasmon absorption of GNR. The aspect ratio of GNR was found to be 3.3±0.3 (figure 53a). TEM of GSH@GNR witnessed a linear assembly (figure 53b) which is attributed to the formation of intermolecular hydrogen bonding between glutathione molecules at the long ends of the rods. The low molecular weight of reduced glutathione is expected to trigger end to end assembly of GNR (C. V. Durgadas *et al.,* 2011). The terminal glutathione molecules are flexible and free to make hydrogen bonds with another glutathione molecule of a second GNR. On conjugation with protoporphyrin IX, the linear assembly breaks (figure 53c) and a peculiar lateral assembly is formed. This indicates the formation of oligomeric aggregates due to the covalent binding of activated COOH with the two NH_2 moieties of GSH@GNR. PPIX cannot form stable bond at the short end of GNR due to the large size and hence it forms side by side assembly by breaking the weak bonds which was responsible for linear assembly in the case of GSH@GNR. The higher molecular weight of PPIX also favors the lateral assembly of GNR(Xue*et al.,* 2013). Finally, on folic acid conjugation, the system retains the same orientation with a partial breakage of lateral assembly. It may be due to the formation of amide bond between self assembled protoporphyrin IX and folic acid. Since the concentration of folic acid used was chosen in such a way (1.7663×10^{-5} and 1.0894×10^{-5} mole) that the final system has both functionality of PS and FA, the lateral assembly is maintained partially. Pictorial representation of the formation of F@PGNR is shown below.

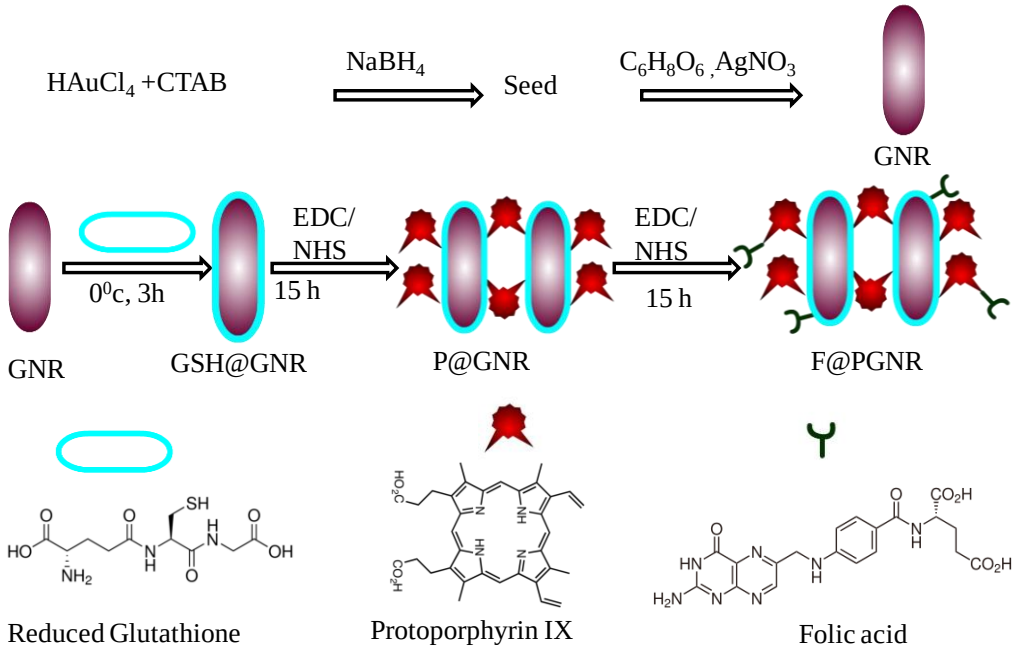

Scheme 9: Schematic representation of different stages of synthesis of F@PGNR.

Fluorescence emission profiles of the samples at various stages of synthesis were evaluated and are shown in Figure 55a. Developed GNR shows characteristic weak emission at 592 nm at an excitation of 500 nm (figure 55b). The origin of fluorescence of gold nanorods due to the excitation of the surface plasmon coherent electronic motion and the d-electrons has been reported earlier (Mohamed *et al.*, 2000). Relaxation of these electronic motions followed by the recombination of the sp- band electrons with holes in the d-band accounts for the emission (Mohamed *et al.*, 2000). The fluorescence is retained in GSH@GNR. Further, protoporphyrin molecule was conjugated as a PDT agent, which also takes part in the energy transfer mechanism to enhance the emission of the combined system making it suitable for imaging applications. As a result of the energy transfer from GNR to PPIX, the combined system P@GNR gives rise to a strong NIR emission at 703 nm whereas the emission at 592 nm weakens. This unique mechanism of energy transfer from GNR to PPIX results from the overlapping of the emission of GNR (592 nm) and the absorption of PPIX (580 to 605 nm) (Figure 55d). Subsequently, the emission spectrum of P@GNR shows a red shift to 703 nm along with a shoulder peak c.a. 660 nm in comparison with PPIX (figure 55a). This agrees with the blue shift of the

Q band of the combined system (figure 51). The functionalisation on the surface of the protoporphyrin ring is always reflected on the changes in Q band energy transition. The successful functionalisation of GSH@GNR over the porphyrin ring results in a change in the absorption and emission profile of PPIX. To confirm the energy transfer from GNR to PS, fluorescence decay was measured at two different excitations, 451 and 344 nm. The fluorescence life times of GNR and P@GNR evaluated at 592 nm emission are 5.58 ns and 4.43 ns respectively (Figure 55e) when excited with 451 nm source. A decrease in the life time of GNR in the combined system, P@GNR is an evidence of the fact that GNR act as an energy donor at this excitation wavelength (500 nm) resulting in the desired strong fluorescence of P@GNR in the NIR region. This has not been observed in any other GNR-chromophore combination, where fluorescence quenching is generally witnessed (Jang *et al.,* 2011a). To further understand this unique behavior, the lifetime at lower wavelength excitation was also studied. An active reverse energy transfer is clear from the life time of GNR and P@GNR (0.021 and 2.34 ns respectively) at 344 nm excitation (figure 55f). This explains that the excitation wavelength plays an important role in deciding the role of donor or acceptor, depending on which the fluorescence enrichment or quenching occurs. Excitation below 451 nm results in the fluorescence quenching or the reverse charge transfer. This switch over of the charge transfer is also evident in the excitation dependent emission of P@GNR in which excitation above 400 nm enhances the NIR emission peak (figure 56a).

On surface functionalisation of P@GNR with folic acid, the emission of F@PGNR further red shifts to 730 nm, which can also be explained based on the change in the functionality over PPIX ring. The shift in the spectrum indicates the decrease in aggregation of PPIX in solution(Xue*et al.,* 2013). The NIR emission exhibited by the final system makes it suitable for *in vivo* imaging applications.

Considering the importance of zeta potential during different functionalisation over GNR, zeta potential at every stages of functionalisation was measured (figure 56b). While GNR had a zeta potential of +15.45 mV, it decreased to +3.5 mV for GSH@GNR, which could be due to the presence of NH_2 and COOH groups of GSH. Further, conjugation with PPIX changes the zeta potential to -29.3

mV, due to the presence of more –COOH groups. F@PGNR showed a zeta potential value of -43.4 mV attributing high stability to the final system.

The imaging capability of aqueous solutions of P@GNR (1 mg/mL) and F@PGNR (1 mg/mL) was evaluated using IVIS Spectrum. Both P@GNR and F@PGNR showed enhanced fluorescence signal compared to PBS, with F@GNR showing maximum signal (figure 57). Enhanced signal in the case of F@GNR is due to the formation of covalent coupling of the folic acid to PPIX which result in breakage of lateral assembly.

Further, to exploit the therapeutic potential of the developed system, photothermal efficacy of F@PGNR in aqueous medium (1 mg/mL) was evaluated using 808 nm laser irradiation (1 W/cm^2). The strong NIR absorption of GNR is responsible for heat generation facilitating thermal therapy applications. An increase in temperature to the order of 60^0C was achieved within 4 min of laser irradiation, at which temperature cancer cells are prone to cell death while undergoing photothermal therapy (PTT) (figure 58).

The singlet oxygen generation capacity of the samples was also evaluated for PDT application, to impart dual therapeutic approach. The singlet oxygen production was confirmed from time-dependent depletion of the absorption of diphenylisobenzofuran (DPBF) at 440 nm(Nair *et al.,* 2015a). When compared to PPIX, which is a FDA approved PS for PDT, P@GNR showed a singlet oxygen yield of 44.7% (Figure 59). The final system, F@PGNR showed an increase in the singlet oxygen generation to 67.56%. This can be due to the covalent coupling of folic acid over P@GNR which resulted in less aggregation of PPIX, which is evident from the red shift in emission spectrum of F@PGNR. This is also reflected in the zeta potential of the final system. The final system, F@PGNR possess all the desired properties like NIR emission, high thermal efficiency and singlet oxygen yield which is required for multifunctional applications like PDT, PTT and *in vivo* imaging.

5.3.2.2. In vitro analysis of gold nanod-PPIX

Biocompatibility of the developed materials was checked in normal mouse fibroblast cell line (L929) using MTT assay (figure 60). GNR is found to be less cytocompatible due to the presence of highly toxic CTAB over it. The toxicity is

reduced substantially in GSH@GNR due to the replacement of CTAB with GSH. The photosensitizer conjugated and final multifunctional system (F@PGNR) has nearly 100% cell viability even at a higher concentration of 1 mg/mL and for longer period (72h) of incubation.

To prove the cellular uptake and targeted PTT and PDT at cellular level, breast cancer cell lines, MCF7 was used as it is known to have folate receptors over-expressed. F@PGNR showed enhanced cell uptake after 3h of incubation in comparison with P@GNR (Figure 61 A&B). This is due to the folate receptor mediated internalization of F@PGNR in comparison with P@GNR. From Z stacking images, it is clear that most of the particles are localized inside the cytoplasm with little uptake in the nucleus due to the non specificity in the uptake of the nanoparticles by the nucleus (Figure 61 a&b).

Targeted PDT and PTT of P@GNR and F@PGNR were checked in MCF 7 cells by irradiating with 530 nm (40s duration) and 808 nm (50s duration) lasers respectively. More than 80% cells were viable in the cells treated with P@GNR and F@PGNR, without laser irradiation. This was so for high concentration of the order of 1 mg/mL of these materials. On the other hand, cells treated with P@GNR and F@PGNR and irradiated with laser showed considerable cell death at all the concentrations studied. This result reconfirms the cytocompatibility of the materials in the absence of laser irradiation and at the same time cytotoxicity of cancer cells when exposed to the particular wavelengths of laser. Concentration dependent toxicity of cancer cells was quantified by measuring the activity of live cells using mitochondrial reductase enzyme assay (figure 62 a&b). IC_{50} values for PTT and PDT were found to be 1 mg/mL and 0.5 mg/mL respectively. The higher IC_{50} value for PTT compared to that of PDT is because PTT depends on the concentration of GNR present in the system. But in the case of PDT, it is the singlet oxygen generated by the system which determines the cell death. Even a lower concentration of PPIX produces a long chain of singlet oxygen.

PDT and PTT were also confirmed using live/dead assay using MCF7 cells. After treating the cells with the particles for 3h, the washed cells were irradiated with 530 nm laser for 40 s with a power of 0.05 W/cm^2 for PDT. The acridine orange & ethidium bromide stained F@PGNR treated cells showed considerable cell death

compared to P@GNR treated group. Live dead assay of the cells after PTT using 808 nm laser (0.05 W/cm^2) irradiation for 50 s, also showed considerable cell death in comparison with control and non targeted material treated cells (Figure 61 a1-c1 & a2-c2).

5.3.2. 3. In vivo analysis of gold nanod-PPIX

On successfully proving PDT and PTT efficiency *in vitro*, synthesised materials were evaluated for their *in vivo* efficacy in mouse tumor models. Initially, the tumor targeted imaging capacity of the material was evaluated by intravenously injecting 500 µL of 1mg/mL P@GNR and F@PGNR in two groups of animals and a third group of tumor bearing animals without any particle injection served as control. The imaging potential of the developed system for live animal imaging was facilitated using Xenogen IVIS Spectrum animal imaging system. Enhanced and focussed signal from the induced tumor was clear in the case of F@PGNR injected animals, indicating that the developed final system is capable of optically image the tumor *site*. The fluorescence signal is not visible in the case of P@GNR injected animals, except in the limb extremity. This is because this system has no tumor targeting property and hence the injected material enters into the circulatory system nd partially gets accumulated in the extremities (Figure 63). After 3h, animals were sacrificed and the organs were harvested and imaged to see the bio-distribution. Here also it is clear that the tumour mass of F@PGNR injected animal shows maximum fluorescence signal compared to control and P@GNR injected animals (Figure 64a). Bio-distribution as seen from the different organs of three groups indicates that the final system F@PGNR follows an efficient clearance mechanism compared to P@GNR (Figure 64b). The fluorescence signal from the kidney and liver gives an indication on this.

Subsequent to the imaging experiments, two separate groups of animals were subjected to *in vivo* PDT and PTT. Animals under the PDT groups received P@GNR and F@PGNR separately and were irradiated with 530 nm laser. Tumour bearing animals without particle injection, irradiated with 530 nm laser served as control. The therapeutic efficiency was followed up using a spectral analysis method. Total hemoglobin concentration and redox ratio were evaluated using fluorescence spectral

analysis of the tumor using fiber optics accessory(Liu & Vo-Dinh 2009; Nazeer *et al.,* 2013, 2014b; Skala *et al.,* 2007). Within a short duration of 3 days, F@PGNR treated animals showed an index similar to that of the normal animals when hemoglobin concentration and redox ratio were considered. This gives an indication of the considerable reduction in the tumor (figure 65 a &b), confirming the PDT efficacy.

Again, another set of animals in three groups were subjected to PTT with 808 nm laser irradiation with P@GNR and F@PGNR injection, separately. Tumour without particle treatment and with laser irradiation served as control. Here also, after successive evaluation using spectral analysis it was observed that F@PGNR treated animal showed a considerable reduction in tumor within 6 days (figure 65 c & d).

In summary, the energy transfer from gold nanorod to the photosensitizer in F@PGNR enhanced emission in the NIR regionto facilitate imaging applications. The inherent thermal property of GNR and singlet oxygen yield of PS contributed to the dual modal cancer therapy. With sufficiently low dose of photosensitiser and laser irradiation, an efficient dual modal cancer treatment strategy was achieved. Both in vitro and in vivo tumor imaging and therapy were successfully demonstrated with the GNR-PS system along with tumor targeting moiety.

Schematic representation of overall work is depicted below

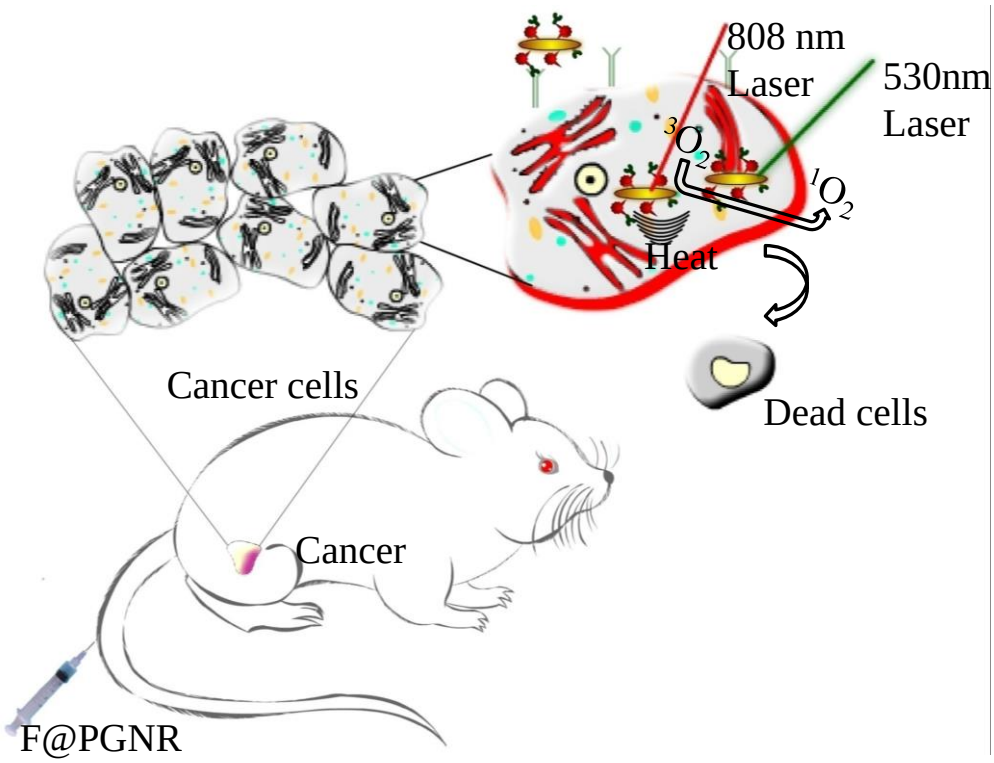

Figure 81: Action of F@PGNR *in vitro* and *in vivo.*

5.4. Gold nanorod-gold cluster hybrid nanomaterial for cancer imaging and therapy

Among the metallic and semiconducting nanomaterials, gold based systems are considered to be most biocompatible. Majority of nanomaterials show definite properties specific to them based on size, shape, nature of materials etc. So combinations ofnanosystems with different properties will be ideal for multifunctional application. Accordingly, considering the good biocompatibility and the unique properties exhibited by different shapes of gold based systems, a gold-gold hybrid system is designed and explained in this section. A highly fluorescent gold nanocluster for imaging application and an anisotropic gold nanorod for therapy were chosen as the candidates.

5.4.1 Synthesis of gold nanorod-gold cluster

Gold nanoclusters(GQC) were synthesised by ligand etching method of gold nanoparticles, ie.,mercaptosucininc acid capped gold nanoparticle (GMSA). GMSA was prepared as described in previous sections. The presence of 520 nm

absorptionindicates the formation of gold nanoparticle. These particles were then etched by glutathione to get gold nanocluster. The gold nanoclusters have clear yellow color with emission at 740 nm (Figure 66). The presence of this NIR fluorescence emission indicates the formation of atomically precise gold quantum clusters. GNR was synthesised in another experiment using seed mediated growth method, as explained in previous sections. The UV-visible spectrum of GNR showed characteristics longitudinal and transverse absorption bands at 707 nm and 532 nm confirming the formation of GNR. On synthesisof the two entities separately, GNR and GQC were tried to combine to make a hybrid system where the identity of both participants are retained, by adopting different reaction conditions and optimizing it (Section 3.6.2.). UV visible spectrum of systems synthesised by adding gold nanorod with acidic, basic and neutral pH to neutral gold cluster exhibited lossof identity of GNR (absence of longitudinal absorption band) (figure 67). Here, change in pH of the GNR system leads to lose of its identity; and the spherical shaped cluster also failed to retain its identity, though all the three systems showed fluorescence. As the pH increased, GNR started to change its shape to other structures and in low pH, the elongation from parent GNR occurs. The anisotropic nature of gold nanorod quenches the fluorescence of gold cluster, and so the combined system does not have the same properties as that of GQC. But it retains the thermal property of GNR (Figure 68).

In order tofulfill the desired outcome, we tried another set of experiments. Now, the neutral GNR system was added to gold cluster with different pH (acidic, basic and neutral). In this case the UV-visible spectra showed peaks of GNR (figure 67). It is because the change in pH of the cluster system does not alter the existence of GNR system. And the emission profiles also indicate that it retains the identity of gold cluster (Figure 67). As the pH of GQC changes, only the nature of glutathione varies depending on its isoelectric point and adjusts the changes itself and doesn't affect GNR. But these changes affect the GNR aggregation. So in acidic and basic pH, aggregation of GNR occurs and leads to decrease in temperature generation property. In case of neutral GQC added to neutral GNR(pH 7), GNR is highly positive and GQC is highly negative resulting in strong electrostatic interaction between them. This force retains the identity of both GQC and GNR (Figure 69).

Again, to choose between these systems, with most favorable property of GNR and GQC, we checked the quantum yield and heat generation capacity of all the systems. It is noted that the second batch (acidic, basic and neutral GQC to neutral GNR)hashigher quantum yield in comparison with first batch (acidic, basic and neutral GNR to neutral GQC) (figure 68). But,the first batch has higher heat generation in comparison with second batch. So, the system with maximum heat generation and fluorescence quantum yield was chosen (figure 68).Accordingly, neutral GQC added to neutral GNR(named as GQC-GNR) is chosen as the best candidate for further studies. So, from these set of experiments and results we confirm that change in pH of the different gold systems will alter its property as well as will affect further reactions. The TEM image of GQC-GNR clearly gives the indication of formation of a hybrid system where an optimum distance is maintained between the two individual components, yet acts as a stable single entity (figure 69). The distance maintained between the two systems would have prevented the energy exchange between the two, helping them to retain their individual properties.

GQC-GNR has the property of fluorescence as well as photothermal capacity and since the material used is only gold,it is comparatively biocompatible. So, this hybrid material was tested for cancer imaging and therapy with folic acid functionalisation for cancer targeting. From UV-visible spectra, 291 nm peak indicates the functionalisation of folic acid to the system. Other major peaks of folic acid were masked by absorption of GQC and GNR (figure 70).

5.4.2. *In vitro* imaging and therapy of GQC-GNR hybrid material

After the successful synthesis of materials with the properties of GNR and GQC, the system was checked for cytotoxicity in L929 and HeLa cells. Both cell lines showed more than 50% cell viability at 0.5 mg/mL of GQC-GNR (figure 71). Without any external stimuli, folate conjugated GQC-GNR showed highly cytocompatible nature making it safe to use in biomedical applications.

Internalisation of folate conjugated GQC-GNR was checked in HeLa cells. In comparison with GNR and control cells, GQC-GNR incubated cells showed well defined fluorescence from the cells, due to internalisation and distribution of folate conjugated GQC-GNR in the HeLa cells. The fluorescence from GQC-GNR was

comparable with GQC alone incubated cells (figure 72).This confirmed the identity of GQC in the cells where GQC-GNR was internalized. The therapeutic efficacy of the system with 808 nm laser irradiation showed a reduction in cell viability in folate conjugated GQC-GNR system due to the photothermal efficacy of the GNR present in GQC-GNR. This treatment efficacy of the system was monitored using MTT assay and Live /dead assay before and after laser irradiation (figure 74a& 73). It is seen that the laser irradiated boundary is acting as clear separation of live and dead cells. It is comparable with the treatment efficacy of GNR alone. But GQC treated and control cells didn't show any thermal therapy effect. The *in vitro* treatment efficacy was again confirmed by Ramanspectral analysis. In comparison with non-irradiated cells, GQC-GNR treated cells followed by laser irradiation showed a decrease in the peak at 682 cm^{-1}, 784, 1071,and1506 cm^{-1} and an increase in the peak of 591 cm^{-1}. It is due to the breakdown of internal phosphate bonds of DNA, decrease inprotein level, degradation of DNA, and expression of new aromatic ring protein(Notingher 2007).

5.4.3. *In vivo* imaging study of GQC-GNR

GQC-GNR was injected intravenously through the tail vein of solid tumor bearing mice to evaluate the imaging and therapeutic potential of the material *in vivo*. For this, the tumor was developed using Daltons Lymphoma Ascites (DLA) cells by subcutaneous injection. On the 4^{th} day of the tumor induction, when the tumor was clearly visible, GQC-GNR was injected through tail vein. The saline-injected animals served as control. All the animals were imaged using IVIS animal imaging system. Only the folic acid conjugated system injected animals showed tumor targeting property (figure 75).Comparatively good quantum yield of the material facilitated the *in vivo* imaging. After 3 h of injection and imaging, animals were sacrificed, and the organs were imaged with an IVIS imaging system (figure 76).It is interesting to see that almost complete targeting of the material is in the tumor region, leaving no traces in any internal organs such as liver, spleen, heart, lungs, etc. High tumor targeting ability and desirable biodistribution endorse this material as a good candidate for *in vitro* cancer imaging and therapy as well as *in vivo* cancer imaging.

In conclusion, a gold based hybrid system was prepared by using a simple method. By controlling the reaction conditions, the individual properties of different components of the hybrid system could be maintained. The imaging and photothermal property of the hybrid system was successfully demonstrated *in vitro* and *in vivo*. Overall work is represented below

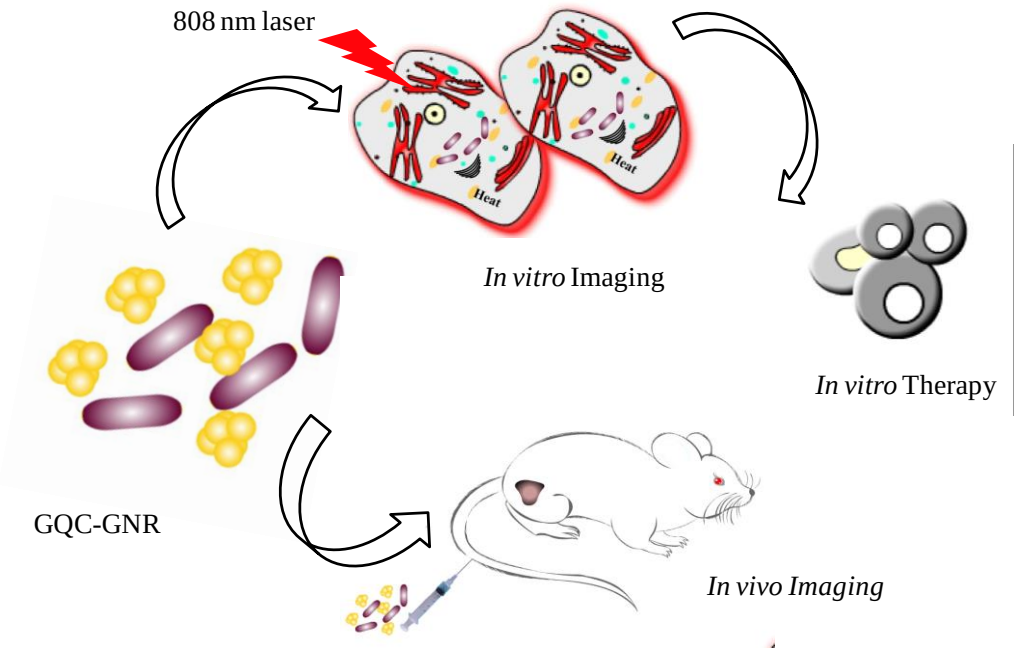

Figure 82: Action of hybrid GQC-GNR to *in vitro* and *in vivo.*

Chapter 6

Summary and Conclusion

Nanotechnology deals with the study of nanosized materials of size in the range of 1-100 nm. Due to its extremely small size, they exhibit unique electronic,

magnetic, and optical properties at the nanosize. These properties make the nanomaterial very special and useful in various fields like data storage, textile industry, cosmetics, and biomedical applications. This thesis deals with the applications of optical nanoparticles in the fields of biosensing, bioimaging, and therapy. The nano candidates considered for this are quantum dots and gold nanostructures like gold nanocluster, nanorods, and a hybrid of both. Based on the level of toxicity and the quantum yield of the materials, they were classified for sensing, imaging and therapy. Quantum dot-based materials were used for the synthesis of nanosensors for the detection of metal ions and biomolecules. Goldbased fluorescent systems were used for sensing, imaging and treatment for cancer. Gold nanorod-cluster hybrid system was synthesised for cancer imaging and therapy.

Thesis consists of mainly four parts: quantum dot based multianalyte detection using optical imaging techniques, cysteine gold cluster for dopamine detection and imaging, fluorescent multifunctional gold nanorod based material for imaging and therapy and gold nanorod- gold cluster hybrid nanomaterialfor cancer imaging and therapy.

The first part of the thesis is subdivided into two- 1)cadmium selenide quantum dots for simultaneous detection of copper and creatinine; 2)cadmium selenide quantum dots for the detection of lead and zinc. In both cases, the basic material used was fluorescing quantum dots. However, it was suitably modified to design the sensors for different analytes. In the first part, a cysteine capped cadmium selenide quantum dots were synthesised and functionalised with 1-Ethyl-3-(3-dimethylaminopropyl)carbodiimide (EDC) and picric acid for the simultaneous detection of copper and creatinine. Cysteine capping and the EDC-picric acid conjugation made the sensor, specific to the molecules of interest Cu and creatinine, respectively. In detail, a cysteine capped cadmium selenide quantum dot with 543 nm emission was synthesised. The quantum dot, functionalised with EDC and picric acid, showed an additional emission peak of 446 nm upon excitation with 290 nm. Thus, the final sensor PAQd had dual emission at 531 nm and 446 nm, the changes of which in the presence of the analytes was utilized for the simultaneous detection of Cu and creatinine. Here Qd-EDC-picric acid forms a Meisenheimer complex (PAQd), which facilitates the simultaneous detection of copper and creatinine. On

addition of copper to PAQd, quenching of 531 nm emissionand enhancement of 446 nm emission peak with creatininewas observed. The sensing property of PAQd was extended to blood serum and cellular environment of L929 and MDA-MB231 cells. The sensing mechanism was explained with the help of transition electron microscopy. Creatinine bound to the meta position of picric acid decreases the organic layer of PAQd due to the high dissolution of molecules formed with picric acid and creatinine. Whereas, on the addition of copper, an increase in the size of the complex was observed due to the formation of a cuprous bis-cysteine complex withcyseine molecule of Qd. Simultaneous detection capacity was proven by zeta potential analysis in which addition of creatinine to PAQd solution containing a highamount of copper showed a decrease in zeta potential value. It indicates that even in the presence of copper, creatinine detection is possible and vice versa.

In the second subdivision of part 1, NIR emitting quantum dots were used for the detection of lead and zinc ions. Qds were synthesised with glutathione as the capping agent (GQd). GQd showed emission at 680 nm at excitation of 420 nm. The FTIR spectrum confirmed the formation of GQd. On addition of lead ions, a decrease in fluorescence intensity or quenching of the 680 nm peak was observed. This quenching is due to the aggregation of glutathione molecule present on the surface of the quantum dot. From DLS analysis, a decrease in size was observed as the concentration of lead ion increases. Lead detection sensitivity ranges from femtomolar to millimolar.Further, GQd was functionalised with sulfamethoxazole for the detection of zinc ions. The FT-IR spectrum of SMGQd confirmed the functionalisation. It showed an emission maximum of 586 nm upon excitation with 420 nm. On adding zinc ions, fluorescence enhancement of the 586 nm peak was observed due to the formation of co-ordination bond with SMGQd and zinc. SMGQd showed nanomolar to millimolar detection range for zinc detection.

In the second part, a novel fluorescent gold cluster was synthesised using cysteine as a stabilizing agent and used for the detection of dopamine, a neurotransmitter, and cell imaging. As the synthesis of cysteine cluster is very difficult, the synthesis procedure was optimized using different concentrations of reactants and was tried at different pHs. The optimized cluster showed an emission maximum at 606 nm at excitation of 400 nm. Upon the addition of dopamine, the

gold cluster showed a fluorescence enhancement. This is due to the competition of dopamine molecules to bind with cysteine molecule of gold cluster, core gold, and neighboring cysteine molecule. The sensing capacity of the system was extended to C6 glial cells. The fluorescence property of the system was utilized for imaging of L929 and HeLa cells. Through MTT assay, this material was found safe for *in vitro* applications. Due to the small size of the gold cluster, passive entry into the cell makes it suitable for cellular imaging of L929 and HeLa. The red emission of the cluster helped in more efficient cellular imaging. Thus, the cysteine gold cluster is proven to be a good candidate for dopamine detection and *in vitro* imaging.

In part 4, gold nanorod based multifunctional system was used for cancer imaging and multimodal therapy. This part is subdivided into two; in the first subdivision, gold nanorod- mitoxantrone drug was used for chemo-photothermal therapy. CTAB stabilization of gold nanorod was replaced by thio-amino PEG to increase biocompatibility followed by folic acid for cancer targeting. Finally, it was functionalised with mitoxantrone, a cancer drug. Different stages of functionalisation were confirmed using UV visible and FT-IR spectra. Bonding of mitoxantrone drug was confirmed from the presence of ester bond in the FTIR spectrum. Due to the strong absorption of the gold nanorod, the drug conjugated system (MTX@FPGNR) showed photothermal efficacy with an increase in the temperature upto 48^{o}C, on 808 nm laser irradiation. MTX@FPGNR showed NIR fluorescence at 711 nm, which is suitable for imaging purposes. Additionally, surface enhanced Raman scattering (SERS) property of gold nanorod was also utilized, so that MTX@FPGNR works on dual imaging property. The drug release study of MTX@FPGNR was performed at different pHs and, with and without laser irradiation. A maximum drug release was observed with acidic pH (pH 4) on irradiation with an 808 nm laser. It is due to the ester hydrolysis of MTX@FPGNR in the presence of an acidic environment on laser irradiation (heat generation). Since the cancer cells have an acidic environment, the same strategy was used for drug release study *in vitro*, using fluorescence and Raman imaging techniques. An increase in NIR fluorescence was observed on the release of the drug upon laser irradiation. Before laser irradiation, well defined Raman peaks of cells were visible due to the SERS effect of MTX@FPGNR. But after laser irradiation, the enhanced fluorescence due to the drug release hinders

Raman detection. From the *in vitro* studies, HeLa cells showed the highest uptake and treatment efficacy because of the extensiveness of folate receptor overexpression compared to the other two cells. MTT and live/dead assay after laser irradiation showed the highest treatment efficacy of MTX@PGNR compared to MTX (chemo) and gold nanorod (photothermal) therapies.

In the second subdivision of part 3, gold nanorod (GNR) was conjugated with a photosensitizer, protoporphyrin IX for combined photothermal and photodynamic therapy, and *in vitro/in vivo* fluorescence imaging. GNR was functionalised with reduced glutathione followed by protoporphyrin IX and finally with folic acid for targeting cancer cells. The functionalisations were confirmed from the presence of additional amide bonds in FT-IR spectra. The final construct (F@PGNR) showed NIR fluorescence at 730 nm, which was utilized for fluorescence imaging. It showed a temperature generation capacity of 60^{o}C within 4 minutes of 808 nm laser irradiation and 67.5 % singlet oxygen generation capacity. The cancer treatment efficacy was checked *in vitro* in MCF7 cells and showed an IC_{50} value of 1 mg/mL and 0.5 mg/mL for PTT and PDT, respectively. Finally, F@PGNR was checked for *in vivo* imaging and therapy in tumor bearing mice. Tumor imaging property, tumor reduction in comparison with the controls, and the biodistribution in the organs were assessed. It was proven to be a good candidate for imaging and therapy.

The fourth and final part is the *in vitro* and *in vivo* cancer imaging and therapy study using a gold hybrid system. The hybrid system was synthesised using a gold nanorod and gold cluster. Gold nanorod having NIR absorption is suitable for therapy and gold cluster having NIR emission is suitable for NIR imaging. By tuning the reaction conditions, the hybrid system was successfully synthesised without compromising the properties of the individual candidates. Properties were evaluated using UV-visible and fluorescence spectra. The final hybrid nanosystemwas functionalised with folic acid for cancer targeting and used for cancer cell imaging and therapy.It showed good efficacy for both imaging and therapy in comparison with its parent counterparts. The material was tested for *in vivo* imaging and found to be a good candidate.

In conclusion, six different optical nanomaterials were developed, with all of them having desirable properties for biomedical applications. Quantum dotbasedmaterials

were developed for sensing and gold based one for sensing, imaging and therapy. The thesis begin with the study of bare quantum dots for sensing applications and explains about the optical properties of anisotropic gold structures such as gold nano rod in the subsequent chapters and quantum confinement of gold cluster showing inherent emission property and finally ends with a hybrid nanomaterialwhich is the future of nanotechnology. In summary, the incorporation of multifunctionality in nanomaterials for better performance of nanosystems is a large area that hasn't explored to its full extent. This thesis is a small contribution towards this field.

Bibliography

Aaron, J, Rosa, E De, Travis, K, Harrison, N, Burt, J & Sokolov, K 2008, 'Polarization microscopy with stellated gold nanoparticles for robust , in-situ monitoring of biomolecules'., *Optics Express*, vol. 16, no. 3, pp.1999–2004.

Abbasian, M, Mahmoodzadeh, F, Salehi, R & Amirshaghaghi, A 2017, 'Chemo – Photothermal Therapy of Cancer Cells Using Gold Nanorods -Cored Stimuli -

Responsive Triblock Copolymer'., *New J. Chem*, vol. 40, no. 2, pp.534–546.

Al-kaysi, RO, Creed, D & Valente, EJ 2004, 'Meisenheimer complex from picric acid and diisopropylcarbodiimide'., *J. Chem. Crystallogr.*, vol. 34, no. 10.

Alagarasi, A 2011, *Introduction to Nanomaterials*.

Ali, EM, Zheng, Y, Yu, H & Ying, JY 2007, 'Ultrasensitive Pb 2 + Detection by Glutathione-Capped Quantum Dots'., *Analytical Chemistry*, vol. 79, no. 24, pp.9452–9458.

Amiri, GR, Fatahian, S & Mahmoudi, S 2013, 'Preparation and Optical Properties Assessment of CdSe Quantum Dots'., *JMSA*, vol. 4, pp.134–137.

Astruc, EB and D 2009, 'Gold nanoparticles in nanomedicine: preparations, imaging, diagnostics, therapies and toxicity'., *Chem.Soc.Rev*, vol. 38, no. 6, pp.1759–1782.

Baptista, P, Pereira, E, Eaton, P, Doria, G, Miranda, A, Gomes, I, Quaresma, P & Franco, R 2008, 'Gold nanoparticles for the development of clinical diagnosis methods'., *Anal Bioanal Chem*, vol. 391, pp.943–950.

Baruah, U, Gogoi, N, Konwar, A, Deka, MJ, Chowdhury, D & Majumdar, G 2014, 'Carbon Dot Based Sensing of Dopamine and Ascorbic Acid'., *J Nanopart Res*, vol. 2014, pp.1–8.

Berlina, AN & Sharma, A 2014, 'Colorimetric Determination of Lead Using Gold Nanoparticles Colorimetric Determination of Lead using Gold Nanoparticles'., *Anal. Lett.*, vol. 48, no. 5, pp.766–782.

Bhattacharya, D, Das, M, Mishra, D, Banerjee, I & Sahu, SK 2011, *Nanoscale Folate receptor targeted , carboxymethyl chitosan functionalized iron oxide nanoparticles : a novel ultradispersed nanoconjugates for bimodal imaging*., pp.1653–1662.

Bucharskaya, A, Maslyakova, G, Terentyuk, G, Yakunin, A, Avetisyan, Y, Bibikova, O, Tuchina, E, Khlebtsov, B & Khlebtsov, N 2016, 'Towards Effective Photothermal / Photodynamic Treatment Using Plasmonic Gold Nanoparticles'., *International Journal of Molecular Sciences*, vol. 17, pp.1–26.

Chen, J, Li, X, Zhao, X, Wu, Q, Zhu, H & Mao, Z 2018, 'Bioactive Materials Doxorubicin-conjugated pH-responsive gold nanorods for combined photothermal therapy and chemotherapy of cancer'., *Bioact. Mater.*, vol. 3, no. 3, pp.347–354. Available from: https://doi.org/10.1016/j.bioactmat.2018.05.003.

Chen, L, Wang, C, Yuan, Z & Chang, H 2015, 'Fluorescent Gold Nanoclusters: Recent Advances in Sensing and Imaging'., *Analytical Chemistry*, vol. 87, pp.216–229.

Chen, P, Roy, P, Chen, L, Ravindranath, R & Chang, H 2014, 'Gold and Silver

Nanomaterial-Based Optical Sensing Systems'., *Part. Part.Syst.Charact*, vol. 31, pp.917–942.

Choi, J, Park, SLJ & Yeon, S 2018, 'Gold nanorod-photosensitizer conjugates with glutathione-sensitive linkages for synergistic cancer photodynamic / photothermal therapy'., *Biotechnology and Bioengineering*, pp.1–15.

Dinicolantonio, JJ, Mangan, D & Keefe, JHO 2018, 'Copper deficiency may be a leading cause of ischaemic heart disease'., *Open hearteart*, vol. 5, pp.1–8.

Du, J, Zhu, B, Leow, WR, Chen, S, Sum, TC, Peng, X & Chen, X 2015, 'Colorimetric Detection of Creatinine Based on Plasmonic Nanoparticles via Synergistic Coordination Chemistry'., *Small*, vol. 11, pp.4104–4110.

Durgadas, C V., Lakshmi, VN, Sharma, CP & Sreenivasan, K 2011, 'Sensing of lead ions using glutathione mediated end to end assembled gold nanorod chains'., *Sensors and Actuators, B: Chemical*, vol. 156, no. 2, pp.791–797.

Durgadas, C V, Lakshmi, VN, Sharma, CP & Sreenivasan, K 2011, 'Chemical Sensing of lead ions using glutathione mediated end to end assembled gold nanorod chains'., *Sens. Actuators B Chem.*, vol. 156, no. 2, pp.791–797. Available from: http://dx.doi.org/10.1016/j.snb.2011.02.040.

Enache, M, Toader, AM & Iancu, EM 2016, 'Mitoxantrone-Surfactant Interactions: A Physicochemical Overview'., *molecules*, vol. 21, no. 1356, pp.1–17.

Eskiizmir, G & Yapıcı, K 2018, 'Photothermal Therapy Learn more about Photothermal Therapy Graphene-based nanomaterials in can- cer treatment and diagnosis'., *ScinceDirect*, no. 2015.

Eustis, S, El-sayed, MA & Kasha, M 2006, *Why gold nanoparticles are more precious than pretty gold : Noble metal surface plasmon resonance and its enhancement of the radiative and nonradiative properties of nanocrystals of different shapes*., pp.209–217.

Fox, EJ 2004, 'Mechanism of action of mitoxantrone'., *Neurology*, vol. 63, no. 12 suppl 6, pp.S15--S18. Available from: https://n.neurology.org/content/63/12_suppl_6/S15.

Frandsen, C & Hansen, MF 2010, 'Magnetic Properties of Nanoparticles'., *Int. J. Mod. Phys. B*, vol. 20, pp.713–744.

Fu, L, Tseng, C, Ju, W & Yang, R 2018, 'Rapid Paper-Based System for Human Serum Creatinine Detection'., *Inventions*, vol. 3, no. 34, pp.1–9.

Ghosh, SK & Pal, T 2007, 'Interparticle coupling effect on the surface plasmon resonance of gold nanoparticles: From theory to applications'., *Chem. Rev.*, vol. 107, no. 11, pp.4797–4862.

Gmoshinskiĭ, Munkhuu & Mazo 2018, '[Trace elements in human nutrition : biological indices of zinc insufficiency].', *Vopr Pitan*, vol. 75, no. 6, p.17313039.

Gobin, M, Lee, MH, Halas, NJ, James, WD, Drezek, RA & West, JL 2007, 'Near-Infrared Resonant Nanoshells for Combined Optical Imaging and Photothermal Cancer Therapy'., *Nano Letters*, vol. 7, no. 7, pp.1929–1934.

Gole, A & Murphy, CJ 2004, 'Seed-Mediated Synthesis of Gold Nanorods : Role of the Size and Nature of the Seed'., *Chem Mater*, vol. 16, no. 21, pp.3633–3640.

Govindaraju, S, Ankireddy, SR, Viswanath, B & Kim, J 2017, 'Fluorescent Gold Nanoclusters for Selective Detection of Dopamine in Cerebrospinal fluid'., *Nature Publishing Group*, pp.1–12. Available from: http://dx.doi.org/10.1038/srep40298.

Gupta, S, Huda, S, Kilpatrick, PK & Velev, OD 2007, 'Characterization and Optimization of Gold Immunoassays'., *Analytical Chemistry*, vol. 79, no. 10, pp.3810–3820.

Han, G, Ghosh, P & Rotello, VM 2007, 'Functionalized gold nanoparticles for drug delivery'., *Nanomedicine*, vol. 2, no. 2, pp.113–123.

Hartland, G V 2011, 'Optical Studies of Dynamics in Noble Metal Nanostructures'., *Chem Rev.*, pp.3858–3887.

Hauck, BTS, Jennings, TL, Yatsenko, T, Kumaradas, JC & Chan, WCW 2008, 'Enhancing the Toxicity of Cancer Chemotherapeutics with Gold Nanorod Hyperthermia **'., *Advanced Materials*, vol. 20, pp.3832–3838.

He, C, Lu, J & Lin, W 2015, 'Hybrid nanoparticles for combination therapy of cancer'., *Journal of Controlled Release*, vol. 219, pp.224–236. Available from: https://doi.org/10.1016/j.jconrel.2015.09.029.

He, Y, Zhang, X & Yu, H 2015, 'Gold nanoparticles-based colorimetric and visual creatinine assay'., *Microchim Acta*, vol. 182, pp.2037–2043.

Hegazy, MA & El-hameed, AMA 2014, 'Characterization of CdSe-nanocrystals used in semiconductors for aerospace applications : Production and optical properties'., *Astron. Geophys.*, vol. 3, no. 1, pp.82–87.

Hembury, M, Chiappini, C, Bertazzo, S, Kalber, TL & Drisko, GL 2015, 'Gold – silica quantum rattles for multimodal imaging and therapy'., *PNAS*, vol. 112, pp.1959–1964.

Hong, EJ, Choi, DG & Suk, M 2016, 'Targeted and effective photodynamic therapy for cancer using functionalized nanomaterials'., *Acta Pharmaceutica Sinica B*, vol. 6, no. 4, pp.297–307. Available from: http://dx.doi.org/10.1016/j.apsb.2016.01.007.

Huang, X, Jain, PK & El-sayed, IH 2008, 'Plasmonic photothermal therapy (PPTT) using gold nanoparticles'., *Lasers Med Sci*, vol. 23, pp.217–228.

Huang, X, Neretina, S & El-Sayed, MA 2009, 'Gold nanorods: From synthesis and properties to biological and biomedical applications'., *Advanced Materials*, vol. 21, no. 48, pp.4880–4910.

Huimin, Z, Yuxiang, GAO, Haixing, XU, Xin, LI, Yahui, LÜ, Tian, MA & Xinjie, CAI 2018, 'Hyaluronic Acid-RGD Peptide Conjugated Mesoporous Silica-coated Gold Nanorods for Cancer Dual-targeted Chemo-photothermal Therapy'., *Journal of Wuhan University of Technology-Mater. Sci. Ed.*, vol. 33, no. 2, pp.512–523.

Jain, PK, Huang, X, El-sayed, IH & El-sayed, MA 2008, 'Noble Metals on the Nanoscale : Optical and Photothermal Properties and Some Applications in Imaging , Sensing , Biology , and Medicine'., *Acc Chem Res*, vol. 41, no. 12, pp.7–9.

Jain, PK, Huang, X, El-Sayed, IH & El-Sayed, MA 2007, 'Review of Some Interesting Surface Plasmon Resonance-Enhanced Properties Review of Some Interesting Surface Plasmon Resonance-enhanced Properties of Noble Metal Nanoparticles and Their Applications to Biosystems'., *Plasmonics*, vol. 2, pp.107–118.

Jang, B, Park, J, Tung, C, Kim, I & Choi, Y 2011a, 'Gold Nanorod-Photosensitizer Complex for Near-Infrared Fluorescence Imaging and Photodynamic/Photothermal Therapy In Vivo'., *ACS Nano*, no. 2, pp.1086–1094.

Jang, B, Park, J, Tung, C, Kim, I & Choi, Y 2011b, 'Gold Nanorod-Photosensitizer Complex for Near-Infrared Fluorescence Imaging and Photodynamic/Photothermal Therapy In Vivo Boseung'., *ACS Nano*, no. 2, pp.1086–1094.

Jang, B, Park, JY, Tung, CH, Kim, IH & Choi, Y 2011c, 'Gold nanorod-photosensitizer complex for near-infrared fluorescence imaging and photodynamic/photothermal therapy in vivo'., *ACS Nano*, vol. 5, no. 2, pp.1086–1094.

Jose, P, Skali, H, Anavekar, N, Tomson, C, Krumholz, HM, Rouleau, JL, Moye, L, Pfeffer, MA & Solomon, SD 2006, 'Increase in Creatinine and Cardiovascular Risk in Patients with Systolic Dysfunction after Myocardial Infarction'., *J Am Soc Nephrol*, vol. 17, pp.2886–2891.

JP, Ma, JN, K, CT, C, LL, F, JW, J & H, B 1993, 'Serum creatinine as an independent predictor of coronary heart disease mortality in normotensive survivors of myocardial'., *Fam Pract*, vol. 36, no. 5, pp.497–503.

Kaneti, YV, Chen, C, Liu, M, Wang, X, Yang, JL, Taylor, RA, Jiang, X & Yu, A 2015, 'Carbon-Coated Gold Nanorods : A Facile Route to Biocompatible Materials for Photothermal Applications Carbon-Coated Gold Nanorods : A Facile Route to Biocompatible Materials for Photothermal Applications Abstract Gold nanorods and

their core-shell nanocom'., *ACS Appl. Mater. Interfaces*, vol. 7, no. 46, pp.25658–25668.

Kelly, KL, Coronado, E, Zhao, LL & Schatz, GC 2003, 'The Optical Properties of Metal Nanoparticles: The Influence of Size, Shape, and Dielectric Environment'., *J. Phys. Chem. B*, vol. 107, pp.668–677.

Kim, T, Zhang, Q, Li, J, Zhang, L & Jokerst, J V 2018, 'A Gold/Silver Hybrid Nanoparticle for Treatment and Photoacoustic Imaging of Bacterial Infection'., *ACS Nano*, vol. 12, pp.5615–5625.

Klar, TA, Sau, BTK, Rogach, AL & Ja, F 2010, 'Properties and Applications of Colloidal Nonspherical Noble Metal Nanoparticles'., *Adv. Mater*, vol. 22, pp.1805–1825.

Klevay, LM 1984, *Dietary copper and risk of coronary heart disease*., vol. 1973, no. 3, pp.1213–1214.

Komatsu, H, Miki, T, Citterio, D, Kubota, T, Shindo, Y, Kitamura, Y, Oka, K & Suzuki, K 2005, 'Single Molecular Multianalyte (Ca 2 + , Mg 2 +) Fluorescent Probe and Applications to Bioimaging'., *J. Am. Chem. Soc.*, vol. 127, pp.10798–10799.

Kreibig, U & Vollmer, Bm 1996, 'Optical Properties of Metal Cluster'.

Kreisman, SH & Hennessey, J V 1999, 'Consistent Reversible Elevations of Serum Creatinine Levels in Severe Hypothyroidism'., *Arch Intern Med.*, vol. 159, pp.79–82.

Kumar, CSSR & Mohammad, F 2011, 'Magnetic nanomaterials for hyperthermia-based therapy and controlled drug delivery'., *Adv. Drug Deliv. Rev.*, vol. 63, no. 9, pp.789–808. Available from: http://dx.doi.org/10.1016/j.addr.2011.03.008.

Kumbhakar, P, Ray, SS & Stepanov, AL 2014, 'Optical Properties of Nanoparticles and Nanocomposites'., *J. Nanomater.*, vol. 2014, pp.2–4.

Kuo, W, Chang, Y, Cho, K, Chiu, K, Lien, C, Yeh, C & Chen, S 2012, 'Biomaterials Gold nanomaterials conjugated with indocyanine green for dual-modality photodynamic and photothermal therapy'., *Biomaterials*, vol. 33, no. 11, pp.3270–3278. Available from: http://dx.doi.org/10.1016/j.biomaterials.2012.01.035.

Kuo, WS, Chang, CN, Chang, YT, Yang, MH, Chien, YH, Chen, SJ & Yeh, CS 2010, 'Gold nanorods in photodynamic therapy, as hyperthermia agents, and in near-infrared optical imaging'., *Angewandte Chemie - International Edition*, vol. 49, no. 15, pp.2711–2715.

Lal, S, Clare, SE & Halas, NJ 2008, 'Therapy : Impending Clinical Impact'., *Accounts of Chemical Research*, vol. 41, no. 12, pp.1842–1851.

Lapotko, D 2009, 'Therapy with gold nanoparticles and lasers : what really kills the cells ?', *Future Medicine*, vol. 4, pp.253–256.

Larson, TA, Bankson, J & Aaron, J 2007, 'Hybrid plasmonic magnetic nanoparticles as molecular specific agents for MRI / optical imaging and photothermal therapy of cancer cells'., *Nanotechnology*, vol. 18, pp.1–8.

Lee, Y-F, Nan, F-H, Chen, M-J, Wu, H-Y, Ho, C-W, CHen, Y-Y & Huang, C-C 2012, 'Analytical Methods Detection and removal of mercury and lead ions by using gold'., *Anal. Methods*, vol. 4, pp.1709–1717.

Li, L, Jiang, W, Luo, K, Song, H, Lan, F, Wu, Y & Gu, Z 2013, 'Superparamagnetic Iron Oxide Nanoparticles as MRI contrast agents for Non-invasive Stem Cell Labeling and Tracking'., *Theranostics*, vol. 3, no. 8, pp.595–615.

Li, M, Zhou, X, Guo, S & Wu, N 2013, 'Detection of lead (II) with a "' turn-on '" fluorescent biosensor based on energy transfer from CdSe / ZnS quantum dots to graphene oxide'., *Biosens. Bioelectron.*, vol. 43, pp.69–74. Available from: http://dx.doi.org/10.1016/j.bios.2012.11.039.

Li, X, Takashima, M, Yuba, E, Harada, A & Kono, K 2014, 'Biomaterials PEGylated PAMAM dendrimer e doxorubicin conjugate-hybridized gold nanorod for combined photothermal-chemotherapy'., *Biomaterials*, vol. 35, no. 24, pp.6576–6584. Available from: http://dx.doi.org/10.1016/j.biomaterials.2014.04.043.

Li, Y, Schluesener, HJ & Xu, S 2010, 'Gold nanoparticle-based biosensors'., *Gold Bulletin*, vol. 43, no. 1, pp.29–41.

Liao, J, Li, W, Peng, J, Yang, Q, Li, H, Wei, Y & Zhang, X 2015, 'Combined Cancer Photothermal-Chemotherapy Based on Doxorubicin / Gold Nanorod-Loaded Polymersomes'., *Theranostics*, vol. 5, no. 4, pp.345–356.

Link, S & El-sayed, MA 2010, 'Shape and size dependence of radiative , non- radiative and photothermal properties of gold nanocrystals'., *Int. Review in Physical Chemistry*.

Liu, Q & Vo-Dinh, T 2009, 'Spectral filtering modulation method for estimation of hemoglobin concentration and oxygenation based on a single fluorescence emission spectrum in tissue phantoms'., *Medical Physics*, vol. 36, no. 10, pp.4819–4829. Available from: http://dx.doi.org/10.1118/1.3218763.

Liu, X, Dai, Q, Austin, L, Coutts, J, Knowles, G, Zou, J & Chen, H 2008, 'A One-Step Homogeneous Immunoassay for Cancer Biomarker Detection Using Gold Nanoparticle Probes Coupled with Dynamic Light Scattering'., *J. Am. Chem. Soc.*, vol. 130, pp.2780–2782.

Lou, T, Chen, L, Chen, Z, Wang, Y, Chen, L & Li, J 2011, 'Colorimetric Detection of Trace Copper Ions Based on Catalytic Leaching of Silver-Coated Gold Nanoparticles'., *ACS*

Appl. Mater. Interface, vol. 3, pp.4215–4220.

Luo, PG & Stutzenberger, FJ 2008, ‘‘Nanotechnology in the Detection and Control of Microorganisms’’ in *Advances in Applied Microbiology* , p.29634.

Luo, QJ, Li, ZG, Lai, JH, Li, FQ & Qiu, P 2017, ‘An on–off–on gold nanocluster-based fluorescent probe for sensitive detection of organophosphorus pesticides’., *RSC Adv.*, vol. 7, pp.55199–55205.

Lyons C Leland, CL 1962, ‘Electrode systems for continuous monitoring in cardiovascular surgery’., *Ann. N. Y. Acad. Sci.*, vol. 102, pp.29–45.

Mackey, MA, Ali, MRK, Austin, LA, Near, RD & El-sayed, MA 2014, ‘The Most E ff ective Gold Nanorod Size for Plasmonic Photothermal Therapy: Theory and In Vitro Experiments’., *The Journal of physical Chemistryhysical Chemistry*, vol. 118, pp.1319–1326.

Maret, W & Sandstead, HH 2006, ‘Zinc requirements and the risks and benefits of zinc supplementation’., *J. Trace Elem. Med. Biol.*, vol. 20, pp.3–18.

Matea, CT & Mocan, T 2017, ‘Quantum dots in imaging , drug delivery and sensor applications’., *International Journal of Nanomedicine*, vol. 12, pp.5421–5431.

Mehta, VN, Kumar, MA & Kailasa, SK 2013, ‘Colorimetric Detection of Copper in Water Samples Using Dopamine Dithiocarbamate-Functionalized Au Nanoparticles’., *Ind. Eng. Chem*, vol. 52, pp.4414–4420.

Miao, X & Shuai, X 2011, ‘Ultrasensitive detection of lead (II) with DNAzyme and gold nanoparticles probes by using a dynamic light scattering technique w’., *Chem. Commun.*, vol. 47, pp.4192–4194.

Mohamed, MB, Volkov, V, Link, S & El-Sayed, MA 2000, ‘The “lightning” gold nanorods: Fluorescence enhancement of over a million compared to the gold metal’., *Chemical Physics Letters*, vol. 317, no. 6, pp.517–523.

Moradian, R, Ghobadi, N, Roushani, M & Shamsipur, M 2011, ‘Synthesis, Characterization and Size Dependent Energy Band Gap of Binary CdSe Quantum Dot and Its Nanoparticle Film’., *J.Iran.Chem.Soc*, vol. 8, pp.22–25.

Murphy, CJ 2002, ‘Optical sensing with quantum dots’., *Anal. Chem.*, pp.520–526.

Murphy, CJ & Coffer, JL 2002, ‘QuantumDots: APrimer’., *Appl. Spectrosc.*, vol. 55, no. 1, p.16A–27A.

Nabiev, I, Baranov, A, Chourpa, I, Beljebbar, A, Sockalingum, GD & Manfait, M 1995, ‘Does Adsorption on the Surface of a Silver Colloid Perturb DrugDNA Interactions? Comparative SERS, FT-SERS, and Resonance Raman Study of Mitoxantrone and Its

Derivatives'., *J. Phys. Chem,* vol. 99, no. Figure l, pp.1608–1613.

Nair, L V., Nagaoka, Y, Maekawa, T, Sakthikumar, D & Jayasree, RS 2014, 'Quantum dot tailored to single wall carbon nanotubes: A multifunctional hybrid nanoconstruct for cellular imaging and targeted photothermal therapy'., *Small,* vol. 10, no. 14, pp.2771–2775.

Nair, L V., Nazeer, SS, Jayasree, RS & Ajayaghosh, A 2015, 'Fluorescence Imaging Assisted Photodynamic Therapy Using Photosensitizer-Linked Gold Quantum Clusters'., *ACS Nano,* vol. 9, no. 6, pp.5825–5832.

Nair, L V, Nair, R V & Jayasree, RS 2016, 'An insight into the optical properties of a sub nanosize glutathione stabilized gold cluster'., *Dalton Trans.,* vol. 45, pp.11286–11291.

Nair, L V, Nair, R V, Shenoy, SJ, Thekkuveettil, A & Jayasree, RS 2017, 'Blood brain barrier permeable gold nanocluster for targeted brain imaging and therapy: an in vitro and in vivo study'., *J. Mater. Chem. B.*, vol. 5, pp.8314–8321.

Nair, L V, Philips, DS & Jayasree, RS 2013, 'A Near-Infrared Fluorescent Nanosensor (AuC @ Urease) for the Selective Detection of Blood Urea'., *Small,* vol. 9, no. 16, pp.2673–2677.

Nair, R V, Santhakumar, H & Jayasree, RS 2018, 'Gold nanorods decorated with a cancer drug for multimodal imaging and therapy'., *Faraday Discuss.,* vol. 207, pp.423–435.

Nazeer, SS, Saraswathy, A, Gupta, AK & Jayasree, RS 2013, 'Fluorescence spectroscopy as a highly potential single-entity tool to identify chromophores and fluorophores: study on neoplastic human brain lesions.', *Journal of biomedical optics,* vol. 18, no. 6, p.67002.

Nazeer, SS, Saraswathy, A, Gupta, AK & Jayasree, RS 2014, 'Fluorescence spectroscopy to discriminate neoplastic human brain lesions: a study using the spectral intensity ratio and multivariate linear discriminant analysis'., *Laser Physics,* vol. 24, no. 2, p.25602. Available from: http://stacks.iop.org/1555-6611/24/i=2/a=025602.

Nikoobakht, B & El-sayed, MA 2003, 'Preparation and Growth Mechanism of Gold Nanorods (NRs) Using Seed-Mediated Growth Method'., *Chem Mater,* vol. 15, no. 16, pp.1957–1962.

Notingher, I 2007, 'Raman Spectroscopy Cell-based Biosensors'., *Sensors,* vol. 7, pp.1343–1358.

Panyala, NR & Havel, J 2009, 'Gold and nano-gold in medicine : Overview , toxicology and perspectives Gold and nano-gold in medicine : overview , toxicology and perspectives'., *J. Appl. Biomed,* vol. 7, pp.75–91.

Park, J, Estrada, A, Sharp, K, Sang, K, Schwartz, JA, Smith, DK, Coleman, C, Payne, JD, Korgel, BA, Dunn, AK & Tunnell, JW 2008, 'Two-photon-induced photoluminenscence imaging of tumors using near-infrared excited gold nanoshells'., *Optics Express*, vol. 16, no. 3, pp.214–221.

Park, S, Lee, JH & Jung, JH 2013, 'A thin-layered chromatography plate prepared from naphthalimide-based receptor immobilized SiO 2 nanoparticles as a portable chemosensor and adsorbent for Pb 2+'., *Analyst*, vol. 138, pp.2812–2815.

Parvanian, S, Mojtaba, S & Aghashiri, M 2017, 'Sensing and Bio-Sensing Research Multifunctional nanoparticle developments in cancer diagnosis and treatment'., *Sensing and Bio-Sensing Research*, vol. 13, pp.81–87. Available from: http://dx.doi.org/10.1016/j.sbsr.2016.08.002.

Peng, J, Xu, W, Teoh, CL, Han, S, Kim, B, Er, JC, Wang, L, Yuan, L, Liu, X & Chang, Y 2015, 'High-efficiency In Vitro and In Vivo Detection of Zn2 + High-efficiency In Vitro and In Vivo Detection of Zn 2 + by Dye- assembled Upconversion Nanoparticles'., *J. Am. Chem. Soc.*, vol. 137, no. 6, pp.2336–2342.

Peng, Y, MaomaoWang, Wu, X, Wang, F & Liu, L 2018, 'Methionine-Capped Gold Nanoclusters as a Fluorescence-Enhanced Probe for Cadmium(II) Sensing'., *Sensors*, no. Ii.

Pereiro, R & Sanz-medel, A 2006, 'The use of luminescent quantum dots for optical sensing'., *Trends in Analytical Chemistry*, vol. 25, no. 3, pp.207–218.

Perez-Hernandez, M, Pino, P del, Mitchell, SG, Moros, M, Stepien, G, Pelaz, B, Parak, WJ & Ga, EM 2015, 'Dissecting the Molecular Mechanism of Apoptosis during Photothermal Therapy Using Gold Nanoprisms'., *ACS Nano*, vol. 9, no. 1, pp.52–61.

Pinchuk, A, Kreibig, U & Hilger, A 2004, 'Optical properties of metallic nanoparticles : influence of interface effects and interband transitions'., *Surface Science*, vol. 557, pp.269–280.

Popp, MK, Oubou, I, Shepherd, C, Nager, Z, Anderson, C & Pagliaro, L 2014, 'Photothermal Therapy Using Gold Nanorods and Near-Infrared Light in a Murine Melanoma Model Increases Survival and Decreases Tumor Volume'., *journal of Nanomaterials*.

Pundir, CS, Yadav, S & Kumar, A 2013, 'Creatinine sensors'., *Trends in Analytical Chemistry*, vol. 50, pp.42–52. Available from: http://dx.doi.org/10.1016/j.trac.2013.04.013.

Qu, X, Li, Y, Li, L, Wang, Y, Liang, J & Liang, J 2015, 'Fluorescent gold nanoclusters:

Synthesis and recent biological application'., *Journal of Nanomaterials*, vol. 2015.

Rahman, MM, Ahmed, J & Asiri, AM 2016, 'Development of Creatine sensor based on Antimony-doped Tin oxide (ATO) nanoparticles'., *Sensors & Actuators: B. Chemical* Available from: http://dx.doi.org/10.1016/j.snb.2016.11.053.

Rastogi, SK, Pal, P, Aston, DE, Bitterwolf, TE & Branen, AL 2011, '8-Aminoquinoline Functionalized Silica Nanoparticles : A Fluorescent Nanosensor for Detection of Divalent Zinc in Aqueous and in Yeast Cell Suspension'., *ACS Appl. Mater. Interface*, vol. 3, pp.1731–1739.

Ray, SC, Chiou, JW, Pong, WF, Tsai, M, Chiou, JW, Pong, WF, Electronic, MTT, Ray, SC, Chiou, JW & Pong, WF 2006, 'The Electronic Properties of Nanomaterials Elucidated by Synchrotron Radiation – Based Spectroscopy The Electronic Properties of Nanomaterials Elucidated by Synchrotron Radiation – Based Spectroscopy'., *Crit Rev Solid State*, vol. 8436.

Richard P Feyman 1960, 'There's Plenty of Room at the Bottom'., *Int. J. Eng. Sci.*

Rock, KL & Kono, H 2008, 'The Inflammatory Response to Cell Death'., *Annu. Rev. Pathol. Mech.Dis*, pp.99–126.

Rostami, S, Mehdinia, A, Jabbari, A, Kowsari, E, Niroumand, R & Booth, TJ 2018, 'Colorimetric sensing of dopamine using hexagonal silver nanoparticles decorated by task-specific pyridinum based ionic liquid'., *Sens. Actuator B-Chem.*, vol. 271, pp.64–72. Available from: https://doi.org/10.1016/j.snb.2018.05.116.

Roti, JLR 2008, 'Cellular responses to hyperthermia (40 – 46 C): Cell killing and molecular events'., *Int. J. Hyperthermia*, vol. 24, no. February, pp.3–15.

Ruedas-rama, MJ & Hall, EAH 2008, 'Azamacrocycle Activated Quantum Dot for Zinc Ion Detection'., *Anal. Chem*, vol. 80, no. 21, pp.8260–8268.

Ruedas-rama, MJ & Hall, EAH 2010, 'Analytical Nanosphere Sensors Using Quantum Dot - Enzyme Conjugates for Urea and Creatinine'., *Anal. Chem.*, vol. 82, no. 21, pp.9043–9049.

Santhakumar, H, Nair, R V, Philips, DS & Shenoy, SJ 2018, 'Real Time Imaging and Dynamics of Hippocampal Zn 2 + under Epileptic Condition Using a Ratiometric Fluorescent Probe'., *Scientific Reports*, vol. 8, no. 1, pp.1–11.

Saraswathy, A, Nazeer, SS, Jeevan, M, Nimi, N, Arumugam, S, Harikrishnan, VS, Varma, PRH & Jayasree, RS 2014a, 'Citrate coated iron oxide nanoparticles with enhanced relaxivity for in vivo magnetic resonance imaging of liver fibrosis a'., *Colloid Surface B*, vol. 117, pp.3–5.

Saraswathy, A, Nazeer, SS, Nimi, N, Arumugam, S, Shenoy, SJ & Jayasree, RS 2014b, 'Synthesis and characterization of dextran stabilized superparamagnetic iron oxide nanoparticles for in vivo MR imaging of liver fibrosis'., *Carbohydrate Polymers*, vol. 101, pp.760–768.

Saul, JM, Annapragada, A, Natarajan, J V. & Bellamkonda, R V. 2003, 'Controlled targeting of liposomal doxorubicin via the folate receptor in vitro'., *Journal of Controlled Release*, vol. 92, no. 1–2, pp.49–67.

Seo, S, Kim, B, Joe, A, Han, H, Chen, X, Cheng, Z, Jang, E & Program, B 2014, 'NIR-light-induced surface-enhanced Raman scattering for detection and photothermal/photodynamic therapy of cancer cells using methylene blue-embedded gold nanorod@SiO2 nanocomposites'., *Biomacromolecules*, vol. 35, no. 10, pp.3309–3318.

Shim, S, Lim, D & Nam, J 2008, 'Ultrasensitive optical biodiagnostic methods using metallic nanoparticles'., *Nanomedicine*, vol. 3, pp.215–232.

Sittiwong, J & Unob, F 2015, 'Detection of urinary creatinine using gold nanoparticles after solid phase extraction'., *Spectrochimica Acta Part A: Molecular and Biomolecular Spectroscopy*, vol. 138, pp.381–386. Available from: http://dx.doi.org/10.1016/j.saa.2014.11.080.

Skala, MC, Riching, KM, Gendron-Fitzpatrick, A, Eickhoff, J, Eliceiri, KW, White, JG & Ramanujam, N 2007, 'In vivo multiphoton microscopy of NADH and FAD redox states, fluorescence lifetimes, and cellular morphology in precancerous epithelia'., *PNAS*, vol. 104, no. 49, pp.19494–19499. Available from: http://www.pnas.org/content/104/49/19494.abstract.

Smith, AM & Nie, S 2010, 'Semiconductor Nanocrystals: Structure, Properties, and Band Gap Engineering'., *Acc Chem Res*, vol. 43, no. 2, pp.190–200.

Song, Y, Qu, K, Xu, C, Ren, J & Qu, X 2010a, 'Visual and quantitative detection of copper ions using magnetic silica nanoparticles clicked on multiwalled carbon nanotubes w'., *Chem. Commun.*, vol. 46, pp.6572–6574.

Song, Y, Qu, K, Xu, C, Ren, J & Qu, X 2010b, 'Visual and quantitative detection of copper ions using magnetic silica nanoparticles clicked on multiwalled carbon nanotubes'., *Chem. Commun.*, vol. 46, pp.6572–6574.

Stockman, MI 2011, 'Nanoplasmonics: The physics behind the applications'., *Physics Today*, vol. 64, no. 2, pp.39–44.

Su, H, Sun, B, Chen, L, Xu, Z & Ai, S 2012, 'Colorimetric sensing of dopamine based on

the aggregation of gold nanoparticles induced by copper ions'., *Anal. Methods*, vol. 4, pp.3981–3986.

Sugunan, A, Thanachayanont, C, Dutta, J & Hilborn, JG 2005, 'Heavy-metal ion sensors using chitosan-capped gold nanoparticles'., *Sci. Technol. Adv. Mater.*, vol. 335, no. 6, pp.335–340.

Sulek, S, Mammadov, B, Mahcicek, DI, Sozeri, H, Atalar, E, Tekinay, AB & Guler, MO 2011, 'Peptide functionalized superparamagnetic iron oxide nanoparticles as MRI'., *J. Mater. Chem.*, vol. 21, pp.15157–15162.

Taylor-pashow, KML, Della, J, Huxford, RC & Lin, W 2010, 'Hybrid nanomaterials for biomedical applications'., *ChemCommun*, vol. 46, pp.5832–5849.

Tham, HP, Chen, H, Tan, YH, Qu, Q, Sreejith, S, Zhao, L, Venkatraman, SS & Zhao, Y 2016, 'Photosensitizer anchored gold nanorods for targeted combinational photothermal and photodynamic therapy'., *Chem. Commun.*, vol. 52, pp.8854–8857.

Tian, X, Zhang, L, Yang, M, Bai, L, Dai, Y & Yu, Z 2018, 'Functional magnetic hybrid nanomaterials for biomedical diagnosis and treatment'., *Nanomedicine and Nanotechnology*, vol. 10, no. February, pp.1–14.

Uauy, R, Olivares, M & Gonzalez, M 1998, 'Essentiality of copper in humans'., *Am J Clin Nutr*, vol. 3970009, pp.952–959.

Uni, V, Liu, J & Lu, Y 2003, 'A Colorimetric Lead Biosensor Using DNAzyme-Directed Assembly of Gold Nanoparticles'., *J. Am. Chem. Soc.*, vol. 125, pp.6642–6643.

Vries, W De, Römkens, PFAM & Schütze, G 2007, 'Critical Soil Concentrations of Cadmium , Lead , and Mercury in View of Health Effects on Humans and Animals'., *Rev Environ contam Toxicol*, vol. 191, pp.91–130.

Wang, B, Wang, J, Liu, Q, Huang, H, Chen, M, Li, K, Li, C, Yu, X & Chu, PK 2014, 'Rose-bengal-conjugated gold nanorods for in vivo photodynamic and photothermal oral cancer therapies'., *Biomaterials*, vol. 35, no. 6, pp.1954–1966. Available from: http://dx.doi.org/10.1016/j.biomaterials.2013.11.066.

Wang, J, Zhu, G, You, M, Song, E, Shukoor, MI, Zhang, K, Altman, MB, Chen, Y, Zhu, Z, Huang, CZ & Tan, W 2013, 'Assembly of Aptamer Switch Probes and Photosensitizer on Gold Nanorods for Targeted Photothermal and Photodynamic Cancer Therapy'., *ACS Nano*, vol. 6, no. 6, pp.5070–5077.

Wang, X, Gao, S, Qin, Z, Tian, R, Wang, G, Zhang, X, Zhu, L & Chen, X 2018, 'Evans Blue Derivative-Functionalized Gold Nanorods for Photothermal Therapy-Enhanced Tumor Chemotherapy'., *ACS Appl. Mater. Interfaces*, vol. 10, pp.15140–15149.

Wei, H, Li, B, Li, J, Dong, S & Wang, E 2008, 'DNAzyme-based colorimetric sensing of lead (Pb 2 +) using unmodified gold nanoparticle probes'., *Nanotechnology*, vol. 095501, pp.0–5.

Wu, C, Kyaw, M, Oo, K & Fan, X 2010, 'Highly Sensitive Multiplexed Heavy Labeled DNAzymes Metal Detection Using Quantum-Dot-'., *ACS Nano*, vol. 4, no. 10, pp.5897–5904.

Wu, W, Sun, Z, Zhang, Y, Xu, J, Yu, H, Liu, X & Wang, Q 2012, 'A multifunctional nanosensor based on silica nanoparticles and biological applications in living cells'., *Chem. Commun.*, vol. 48, pp.11017–11019.

Wu, Z & Jin, R 2010, *On the Ligand ' s Role in the Fluorescence of.*, vol. 25, pp.2568–2573.

Xu, H, Miao, R, Fang, Z & Zhong, X 2011, 'Quantum dot-based " turn-on " fluorescent probe for detection of zinc and cadmium ions in aqueous media'., *Analytica Chimica Acta*, vol. 687, pp.82–88.

Xu, X, Daniel, WL, Wei, W & Mirkin, CA 2012, 'Colorimetric Cu2+ Detection Using DNA Modified Gold Nanoparticle Aggregates as Probes and Click Chemist'., *Small*, vol. 6, no. 5, pp.623–626.

Xu, Y, Zhou, Y, Ma, W & Wang, S 2013, 'A Fluorescent Sensor for Zinc Detection and Removal Based on Core-Shell Functionalized Fe 3 O 4 @ SiO 2 Nanoparticles'., *J. Nanomater.*, vol. 2013, pp.1–7.

Xue, C, Birel, O, Li, Y, Ma, X, Gao, M, Urbas, A & Li, Q 2013, 'Porphyrin metal complex monolayer-protected gold nanorods: A parallel facile synthesis and self-assembly'., *Journal of Colloid and Interface Science*, vol. 398, pp.1–6. Available from: http://dx.doi.org/10.1016/j.jcis.2013.02.014.

Yang, S, Palanikumar, L, Jeong, S, Kim, K, Lee, J, Jeoung, E, Kim, C, Ryu, J & Park, M 2018, 'Synergistic Effect of Photothermal Therapy and Chemotherapy Using Camptothecin-Conjugated Gold Nanorods'., *Part. Part.Syst.Charact*, vol. 1700307, pp.1–9.

Yildirim, A & Bayindir, M 2014, 'Turn-on Fluorescent Dopamine Sensing Based on in Situ Formation of Visible Light Emitting Polydopamine Nanoparticles'., *Anal. Chem.*, vol. 86, pp.5508–5512.

Zhang, L, Su, H, Cai, J, Cheng, D, Zhang, J, Zhou, C, Liu, S, Shi, H, Zhang, Y & Zhang, C 2016, 'A Multifunctional Platform for Tumor Angiogenesis-Targeted Chemo-Thermal Therapy Using Polydopamine-Coated Gold Nanorods'., *ACS Nano*, vol. 10, pp.10404–10417.

Zhang, X, Chen, X, Kai, S, Wang, H, Yang, J, Wu, F & Chen, Z 2015, 'Highly Sensitive and Selective Detection of Dopamine Using One- Pot Synthesized Highly Photoluminiscent Silicon Nanoparticles'., *Anal. Chem.,* vol. 87, no. 6, pp.3360–3365.

Zhaomin, Z, Yupeng, S, Pan, Y & Li, M 2014, 'Quinoline derivative-functionalized carbon dots as a fluorescent nanosensor for sensing and intracellular imaging of Zn2+'., *J. Mater. Chem. B,* vol. 2, pp.5020–5027.

Zheng, Y, Wang, Y & Yang, X 2011, 'Chemical Aptamer-based colorimetric biosensing of dopamine using unmodified gold nanoparticles'., *Sens. Actuator B-Chem.,* vol. 156, no. 1, pp.95–99. Available from: http://dx.doi.org/10.1016/j.snb.2011.03.077.

Zhong, G, Liu, J & Liu, X 2015, 'A Fast Colourimetric Assay for Lead Detection Using Label-Free'., *Macromachines,* vol. 6, pp.462–472.

Zijlstra, P & MoNOS, MO 2011, 'Single metal nanoparticles : optical detection , spectroscopy and applications'., *Rep. Prog. Phys.*, vol. 74.

List of publications

1 **Resmi V. Nair**, Parvathy Radhakrishna Pillai Suma, Willi Paul Ramapurath S. Jayasree, Vanadium pentoxide nanoplates: Synthesis, characterization and unveiling the intrinsic anti-bacterial activity, *Mater. Lett.,* 269,127673,2020.

2 **Resmi V. Nair**, Parvathy R. S., Ramapurath S. Jayasree, A dual signal on-off fluorescent nanosensor for the simultaneous detection of copper and creatinine, *Mater. Sci. Eng. C,* 109, 110569, 2020.

3 **Resmi V. Nair**, Lakshmi V. Nair, Divya Maldepalli Govindachar, Hema Santhakumar, Shaiju S. Nazeer, Sachin J. Shenoy, Ganga Periyasamy, Ramapurath S. Jayasree, Luminescent Gold Nanorod to enhance the NIR emission of Photosensitizer for Targeted Cancer Imaging and Dual therapy: Experimental and Theoretical Approach, *Chem. Eur. J*, , 26, 2826–2836, 2020 (frontispiece).

4 Resmi V Nair, Hema Santhakumar, Ramapurath S Jayasree, Gold nanorods decorated with a cancer drug for multimodal imaging and therapy, *Faraday Discuss*.,207, 423-435, 2018.

5 H Santhakumar, **Resmi V Nair**, DS Philips, SJ Shenoy, A Thekkuveettil, RS Jayasree, Real Time Imaging and Dynamics of Hippocampal Zn^{2+} under Epileptic Condition Using a Ratiometric Fluorescent Probe, *Sci. Rep*, 8, 9069, 2018

6 LV Nair, **Resmi V Nair**, SJ Shenoy, A Thekkuveettil, RS Jayasree, Blood brain barrier permeable gold nanocluster for targeted brain imaging and therapy: an *in vitro* and *in vivo* study; *J. Mater. Chem. B,*5 (42), 8314-8321, 2017

7 Lakshmi.V.Nair, **Resmi.V.Nair**, RS Jayasree, An insight into the optical property of sub nano size glutathione stabilized gold cluster, *Dalton Transactions*, 45, 11286-11291, 2016.

8 **Resmi V Nair**, Lakshmi V Nair, Divya Maldepalli Govindachar, Hema Santhakumar, Sachin J Shenoy, Ganga periyasamy, Ramapurath S Jayasree, " Luminescent Gold Nanorod induced NIR emission of Photosensitizer for

Targeted Cancer Imaging and Dual therapy: Experimental and Theoretical Approach", *Adv Funct Mater* (under revision).

9 **Resmi V Nair**, Parvathy R S, Ramapurath S Jayasree, An On-Off Fluorescent Nanosensor for the Simultaneous detection of Copper and Creatinine (Communicated).

Book Chapter

Resmi V Nair and Ramapurath S. Jayasree (2018) **Role of Advanced Nanomaterials in Biosensing;** In **Drug delivery nanosystem for Biomedical Applications** – 1st Edition, Chandra P Sharma (ed), *Elsevier***.**

Patent

Resmi V Nair, Parvathy R S, Ramapurath S Jayasree, Multifunctional fluorescent nanosensor for simultaneous detection of copper and creatinine and the process thereof (*Indian Patent Application 201741031554*).